This is to certify that the

dissertation entitled

Inelastic Response of Reinforced Concrete Elements To Dynamic Loads

presented by

Jong Sung Sim

has been accepted towards fulfillment
of the requirements for

Ph.D. degree in Civil Engineering

Major professor

Date 4/27/87

INELASTIC RESPONSE OF REINFORCED CONCRETE ELEMENTS TO DYNAMIC LOADS

By

Jongsung Sim

A DISSERTATION

Submitted to

Michigan State University

in partial fulfillment of the requirements

for the degree of

DOCTOR OF PHILOSOPHY

Department of Civil and Environmental Engineering

1987

ABSTRACT

INELALSTIC RESPONSE OF REINFOCED CONCRETE ELEMENTS TO DYNAMIC LOADS

By

Jongsung Sim

Strain rate effects and shear deformations are two factors with major effects on the dynamic response characteristics of reinforced concrete (R/C) structures, which are generally neglected in dynamic analysis. In this investigation, the analytical techniques capable of accounting for these effects of these two factors were developed for dynamic analysis of R/C elements (and structures). These techniques were used in numerical studies on the sensitivity of R/C elements behavior to the variations in the rate of straining under monotonic loading and to the effects of shear deformations under cyclic loadng.

The strain rate-sensitive element model was constructed based on the strain rate-dependent constitutive models of steel and concrete which was empirically developed in this study. A refined (layer) element modeling technique was used for axial-flexural analysis of R/C beam-columns at different rates of load application. The element model was used in numerical studies to assess the strain rate effects on the axial compressive monotonic load-deformation behavior of R/C columns and flexural behavior of R/C beams.

In order to account for the effects of shear deformations on the cyclic behavior of R/C beams, an element model which physically separates the flexural and shear deformations was developed. This element model considers the differences between the shear and flexural hysteretic characteristics of R/C beams (marked by the highly deteriorating nature of shear resisting mechanisms under cyclic loads). The tangent stiffness matrix of the element model was also developed, and the experimentally-observed tendency of shear deformations to dominate the element load-deformation behavior under repeated inelastic load cycles was verified analytically.

To my Parents

ACKNOWLEDGEMENT

I would like to express appreciation to those who have helped and contributed to making this work a reality. This includes my dissertation advisor, Dr. Parviz Soroushian for his guidance and assistance; all of my guidance committee members, Dr. W. A. Bradley, Dr. R. K. Wen, and Dr. W. E. Kuan for their interest and help during preparation of this work; and all members of the Structures Research Laboratory for their assistance in the experimental portions of this work.

The numerical results and most of the figures presented in this dissertation were produced using the computational and plotting facilities of the Albert H. Case Center for Computer Aided Design at Michigan State University. This study was financially supported by General Electric Corperation, and MSU(All University Research Initiation Grants). This support is gratefully acknowledged.

Finally, sincere thanks are extended to my parents and parents-in-law, and my wife Yoonhi, my son Chungwook, my brothers, my brothers-in-law, and sisters-in-law for their encouragement.

TABLE OF CONTENTS

LIST OF TABLES

LIST OF FIGURES

LIST OF NOTATIONS

A_g = gross area of the concrete cross section
A_s = area of tension steel
A_s' = area of compression steel
A_{st} = total area of longitudinal steel
a = depth of equivalent rectangular block representing compressive resistance of concrete in beams
b = width of cross section
c = depth of neutral axis of cross section
d = effective depth of cross section
d' = distance from centroid of compression steel to the extreme compression fiber
dM = incremental bending moment of cross section
dM_i = incremental bending moment at end i
dM_j = incremental bending moment at end j
dM_e = incremental bending moment of element
dP = incremental axial load at cross section
dP_e = incremental axial load on element
dV = incremental lateral load
dV_e = incremental lateral load of element
dt = incremental loading time
$d\Delta_e$ = incremental free end lateral displacement of element
$d\delta$ = incremental displacement at free end of the cantilever beam
$d\delta_s$ = shear spring incremental deformation
$d\epsilon$ = strain increment
$d\epsilon_i$ = strain increment at the i'th layer
$d\dot{\epsilon}_i$ = strain rate increment at the i'th layer
$d\epsilon_p$ = strain increment at plastic centroid
$d\gamma_e$ = incremental axial deformation
$d\phi$ = incremental curvature

$d\theta_f$ = flexural spring incremental deformation

$d\theta_s$ = shear spring incremental deformation

E_{cd} = dynamic secant modulus of elasticity

E_{cs} = static secant modulus of elasticity

E_h = static strain hardening modulus of steel

E_h' = dynamic strain hardening modulus of steel

E_i = tangent stiffness modulus of the i'th layer

E_s = modulus of elasticity of steel

E_{td} = dynamic tangent modulus of elasticity

E_{ts} = static tangent modulus of elasticity

F_y = yield force of the proposed hysteretic model

f_c = concrete stress

f_c' = standard (quasi-static) compressive strength of concrete

f_c'' = dynamic compressive strength of concrete

f_{cd} = dynamic compressive strength of concrete

f_{cs} = static compressive strength of concrete

f_p = static upper yield strength of steel

f_p' = dynamic upper yield strength of steel

f_s = steel stress

f_{sc} = compression steel stress

f_u = static ultimate strength of steel

f_u' = dynamic ultimate strength of steel

f_y = standard (quasi-static) yield strength of steel

f_y' = dynamic yield strength of steel

f_{yh} = yield strength of transverse reinforcement

h' = width of concrete core measured from outside of transverse reinforcement

K_{11}, K_{12}, K_{21}, and K_{22} = components of the section tangent stiffness matrix

K_f = tangent stiffness of flexural spring

K_{fi} = tangent stiffness of flexural spring at end i

K_{fj} = tangent stiffness of flexural spring at end j

K_G = element tangent stiffness matrix

K_i = initial stiffness of the proposed model

K_h = strain hardening stiffness of the proposed model

K_s = tangent stiffness of shear spring

K_{si} = tangent stiffness of shear spring at end i

K_{sj} = tangent stiffness of shear spring at end j

K_t = tangent stiffness of cantilever element

K_u = unloading stiffness of the proposed model

K_γ = quasi-static secant axial stiffness

K'_γ = dynamic secant axial stiffness

L = total element length

l = cantilever element length

M_n = static flexural strength

M'_n = dynamic flexural strength

P = axial force on element

P_n = nominal axial strength

P'_n = dynamic axial strength

s = center to center spacing of transverse reinforcement

V = lateral force of cantilever element

V_n = quasi-static lateral strength

V'_n = dynamic lateral strength

y_i = distance from centroid of the i'th layer to the plastic centroid

R = a point on the skeleton curve in the element model

R/C = reinforced concrete

X = spring deformation in the element model

X_y = yield deformation

Δ = lateral displacement of element

α = a coefficient used in the element model

β = a coefficient used in the element model

ϵ = strain

$\dot{\epsilon}$ = strain rate (1/sec) $\geq 10^{-5}$

$\dot{\epsilon}_i$ = strain rate in the i'th layer

$\dot{\epsilon}_p$ = strain rate at plastic centroid

ϵ_h = static strain at initiation of strain hardening

ϵ'_h = dynamic strain at initiation of strain hardening

ϵ_{od} = dynamic strain at maximum stress

ϵ_{os} = static strain at maximum stress

ϵ_s = steel strain

ϵ_u = quasi-static ultimate strain of steel

ϵ'_u = dynamic ultimate strain of steel

γ = a coefficient used in element model

ϕ = section curvature

$\dot{\phi}$ = section curvature rate

ψ = element orientation angle

ρ = tensile steel ratio

ρ' = compressive steel ratio

ρ_s = volumetric ratio of transverse reinforcement to concrete core

θ = rotation of element

θ_i = rotation of element at end i

θ_j = rotation of element at end j

ς = a coefficient used in the element model

CHAPTER 1

INTRODUCTION

Experimental data have indicated that the rate of loading and the shear deformations are two major variables influencing the inelastic response of reinforced concrete (R/C) elements and structures to dynamic loads. These two factors, however, have been generally neglected in the development of analytical models for predicting the inelastic dynamic response of R/C structures.

Dynamic (e.g., seismic and impulsive) loadings induce relatively high strain rates in structures as compared to the quasi-static laboratory loads. Increased strain rates result in higher strengths and moduli of elasticity of concrete and reinforcing steel, and consequently increased the strengths and stiffnesses of R/C elements[1-5]*. These modifications in element behavior at higher rates of straining might adversely influence the dynamic response characteristics of R/C structures, resulting in higher element forces and stronger tendencies towards the brittle modes of failure. Hence, the disregard for the strain rate effects in dynamic analysis of R/C structures might actually lead to unsafe structural designs.

Under repeated inelastic load reversals, shear deformations play an increasingly important role in the inelastic load-deformation behavior of R/C elements[6-8]. This is due to the deteriorating nature (under cyclic loads) of the

* Numbers in square brakets refer to the list of references.

shear resisting mechanisms when compared with the flexural ones. Many analytical predictions of dynamic response of R/C structures, however, have neglected the effects of shear deformations, disregarding the fact that the relatively small and negligible shear deformations (compared with the flexural ones) under monotonic loads tend to grow and dominate the behavior under repeated inelastic load cycles. Dynamic response characteristics of R/C structures might also be adversely influenced by the deteriorations in the shear resisting mechnisms of elements. Hence, the disregard for shear deformations in dynamic analysis of R/C structures can also damage the accuracy and safety of final designs.

The first part of this dissertation (Chapters 2 to 5) deals with strain rate effects on the dynamic properties of R/C materials and structural elements under monotonic loading conditions. The second part (Chapter 6) examines the effects of shear deformations on the cyclic load-deformation relationships of the elements.

In order to assess the strain rate effects on the dynamic response of R/C elements, strain rate-sensitive constitutive models were developed for concrete and steel (Chapter 3 and 4, respectively), and they were incorporated into a refined nonlinear analysis procedure for predicting the axial-flexural response of R/C sectons and beam-column elements to monotonic dynamic loads (Chapter 5). The analysis techniques were verified using the results of a relatively large number of quasi-static and dynamic tests on R/C elements. The developed strain-dependent element model was then used for numerical studies on the sensitivity of the axial/flexural behavior of R/C beams and columns to the variations in the rate of straining.

In studies on shear deformations (Chapter 6), a beam element model capable of distinguishing between the hysteretic characteristics of the shear and flexural actions was developed. This element model consists of a physical simulation which treats the axial and flexural actions separately, and two distinct sets of

empirical hysteretic rules for cyclic shear and flexural deformations. These hysteretic rules account for the higher deteriorating nature of the shear behavior which leads to the growing dominance of shear deformations under repeated inelastic load reversals. The tangent stiffness matrix of the developed element model was also derived, and the model was verified using the results of a relatively large number of cyclic tests on R/C beams with wide ranges of material and geometric characteristics.

CHAPTER 2

STRAIN RATE EFFECTS ON THE DYNAMIC RESPONSE OF REINFORCED CONCRETE STRUCTURES: A REVIEW OF THE LITERATURE

2.1 INTRODUCTION

The current reinforced concrete seismic analysis and design procedures[9] are generally based on the results of quasi-static tests on R/C materials and elements. The rate of straining in such tests is of the order of 10^{-5}/sec[1-4]. Typical earthquake- and impulse-induced strain rates are, however, of the order of 10^{-2} and 10^{-1}/sec, repectively[4,5], and dynamic test results on the reinforced concrete materials and elements[10-26] have revealed considerable dependence of the results on the rate of straining. For example, at the high earthquake-induced loading rates, the axial and flexural strengths of the reinforced concrete (R/C) beam-columns have been observed to increase by about 20% over the quasi-static values[4,5,8,12,15].

The potential problems caused by disregarding the strain rate effects in the current methods for dynamic analysis and design of the R/C structures are discussed below:

(a) Maximum seismic shear forces in the structural elements are proportional to their flexural strength[9] (Figure 2.1a), and thus they increase proportionally

with the flexural strength as the rate of straining increases. The corresponding increase in shear strength is, however, smaller[12,24]. Hence, a beam with a ductile flexural failure under quasi-static loading might fail suddenly in shear when the load is applied dynamically.

(b) The maximum bond stress between steel and concrete as well as the maximum shear force in the R/C beam-column joints under seismic loads increase proportionally with the bar strength as the rate of straining increases[9,27] (Figure 2.1b). If this is not accompanied by comparable increases in the bond and shear strengths in the joints, then a beam with flexural failure under quasi-static loads might fail by bar pull-out or joint shear cracking if the load is applied dynamically. This will adversely influence the ductility and energy dissipation capacity of the element.

(c) In the present philosophy of seismic design, it is assumed that the flexural yielding and hysteretic energy dissipation in the critical regions of the structures reduce the seismic forces in the structural elements. At higher strain rates, however, the increased element yield strength postpones the formation of the plastic hinges[3,8,12,24,28]. This can increase the earthquake-induced internal forces in the structural elements.

(d) At higher strain rates, the stiffnesses of the R/C materials and elements increase and thus the overall structural stiffness also increases[5,8,10,28]. This modifies the seismic response characteristics of the system.

(e) In the coupled wall systems, the maximum axial forces in the walls are proportional to the maximum shear forces (and consequently to the flexural strengths) of the coupling girders (Figure 2.1c), and hence they increase with increasing strain rates. The increased wall axial forces might substantially modify the seismic response characteristics of the R/C structures [29-32]. The same discussion also applies to the axial forces in the columns of the R/C

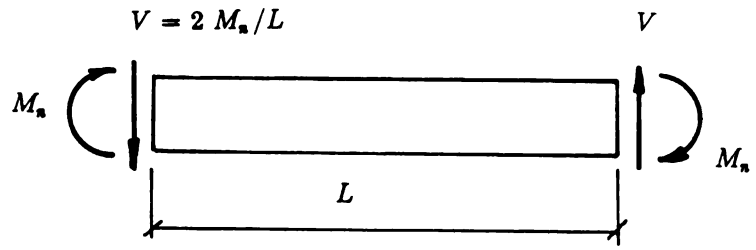

(a) Beam Shear Forces

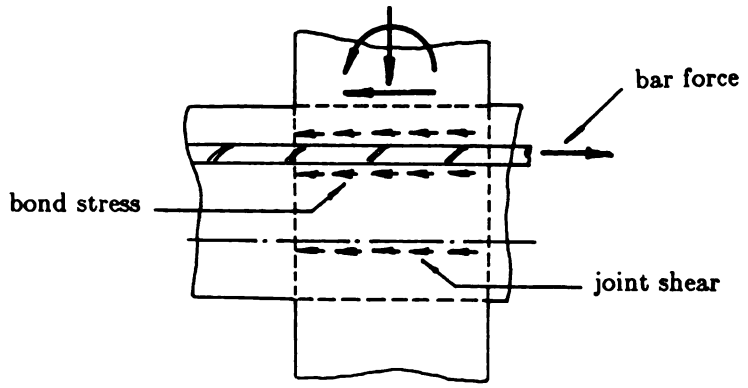

(b) Joint Shear and Bond Stresses

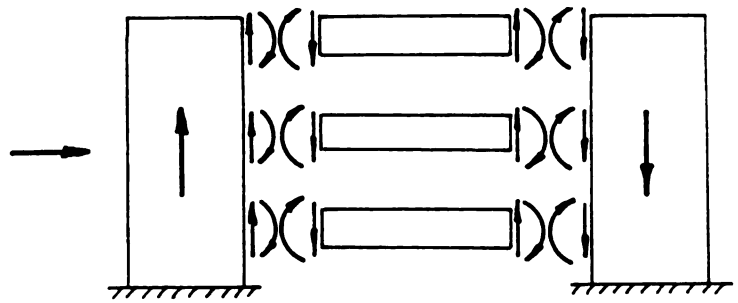

(c) Wall Axial Forces

Figure 2.1 Strain Rate Effect on The R/C Element under Seismic Forces

frames that will be modified due to the strain rate-sensitivity of the beams.

(f) In the lower stories of the R/C tall buildings, the column reinforcing bars are usually of higher strength than the beam reinforcement. Considering that the higher strength steel is less strain rate-sensitive[12,17,25,26], then a strong column - weak beam design[9] under quasi-static loads might turn out to be weak column - strong beam under dynamic loads.

(g) At higher strain rates, the increase in the element strength and the subsequent increase in the element seismic forces might increase the tendency towards the buckling failure modes in the structure.

The remainder of this chapter presents a critical review of the literature on the strain rate-sensitivity of the R/C materials and elements. No analytical or experimental studies regarding the strain rate effects on the overall dynamic response characteristics of the R/C structures have been reported in the literature.

2.2 CONCRETE IN COMPRESSION

Typical static and dynamic monotonic stress-strain diagrams of concrete loaded in compression are compared in Figure 2.2(a). As shown in this figure, with increasing strain rate, the compressive strength and modulus of elasticity of both confined and unconfined concrete increase, and the maximum strain at failure in unconfined concrete decreases.

Figure 2.2(b) presents an accumulation of the available test data[4,5,10-15] as well as some empirical expressions[10,12] regarding the strain rate-sensitivity of the concrete compressive strength. The considerable scatter of the test results observed in Figure 2.2(b) has been attributed to the variations in the moisture content, compressive strength and confinement of the tested concrete specimens[4,10-14].

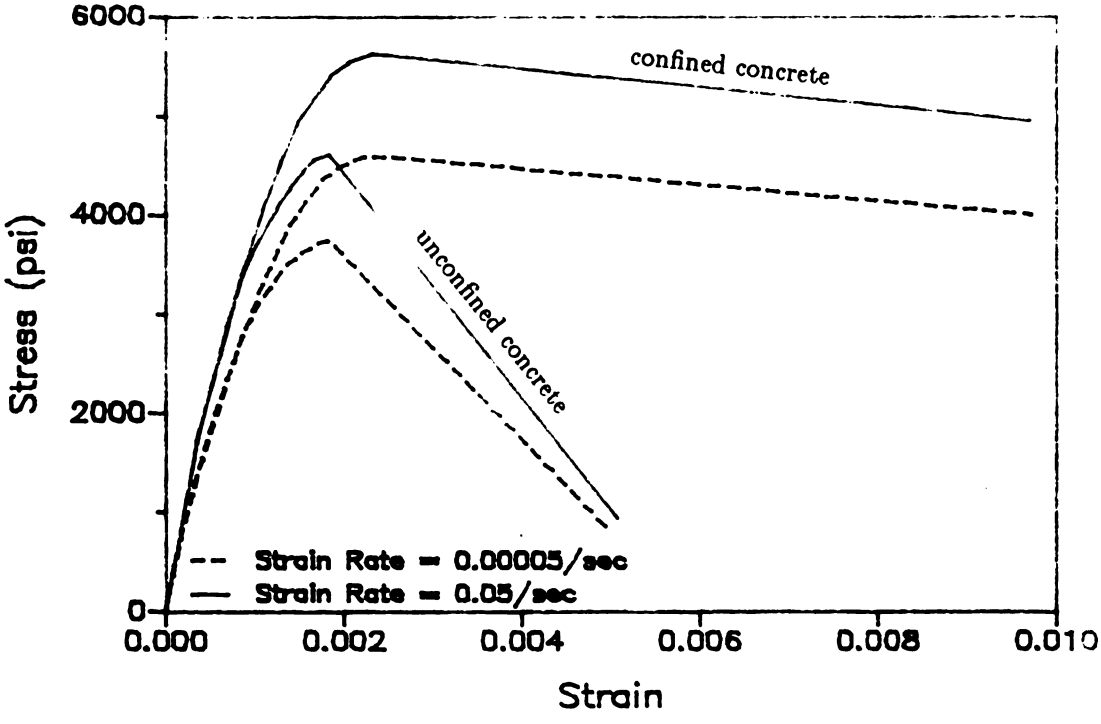

(a) Constitutive Behavior

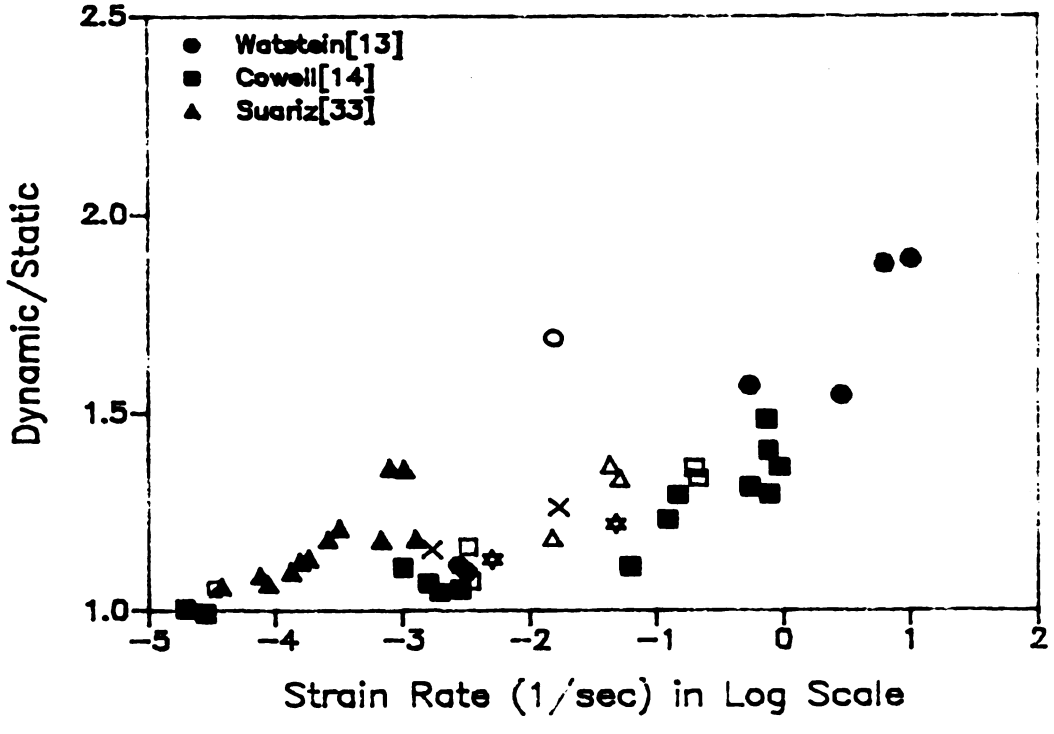

(b) Compressive Strength

Figure 2.2 Strain Rate-Sensitivity of The Concrete Mechanical Properties

Figures 2.2(c) and (d) show the strain rate effect on the secant and initial tangent moduli of concrete, respectively[4,10,12,13,33]. The initial tangent modulus is seen to be less strain rate-sensitive than the secant modulus. The strain rate-sensitivity of the concrete strain at maximum stress is demonstrated in Figure 2.2(e). The model of Reference 10 does not agree well with the test results given in this figure.

Strain rate-sensitive constitutive models for concrete are presented in References 10 and 33. The inaccuracies of the typical model given in Reference 10 in predicting the test results are shown in Figure 2.2(f), where the result of a dynamic test[15] on an R/C column with a compressive strength of 6,000 psi is compared with the stress-strain diagram predicted by this model.

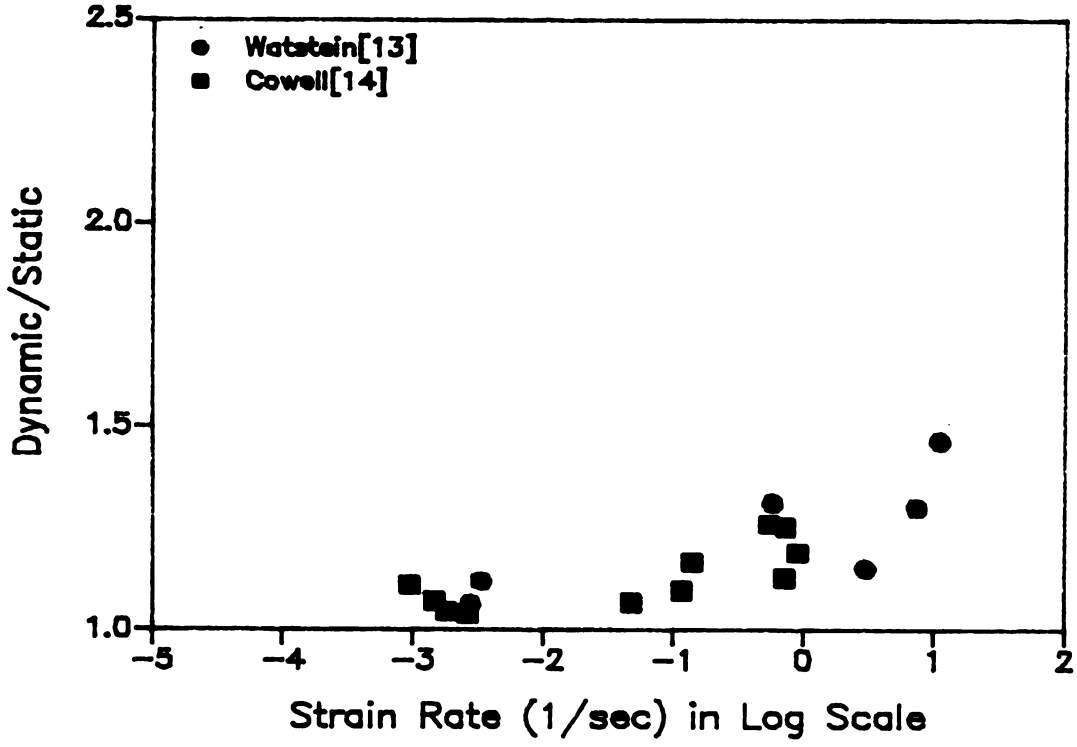

(c) Secant Modulus

Figure 2.2 Strain Rate-Sensitivity of The Concrete Mechanical Properties (cont'd)

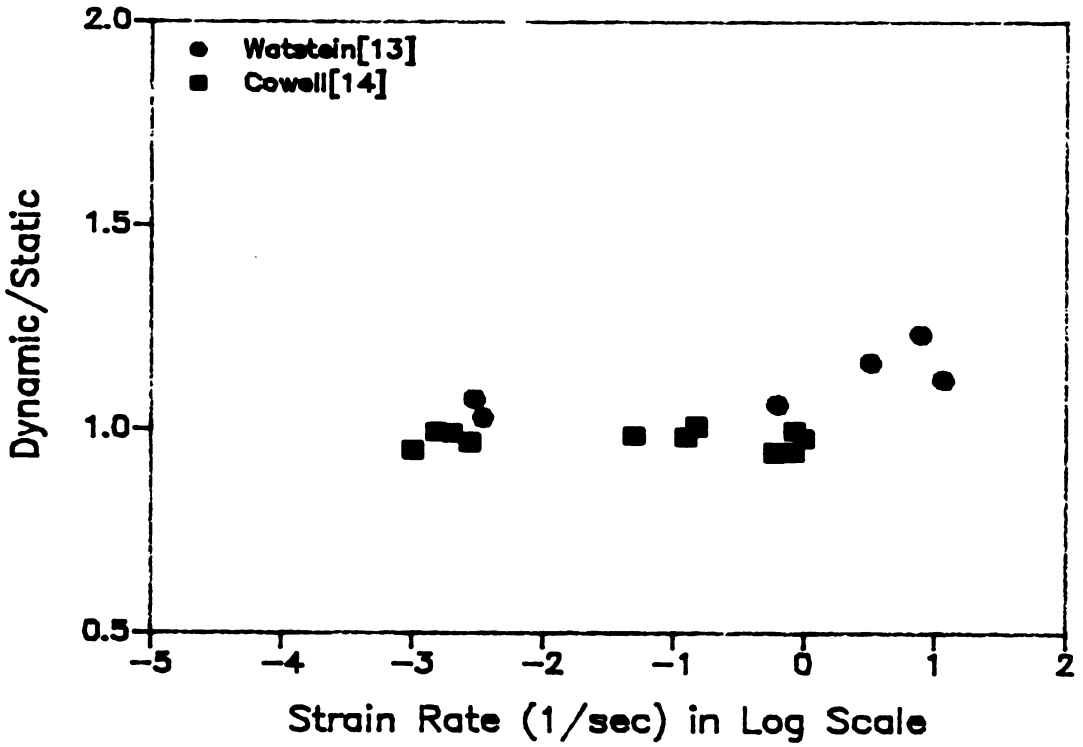

(d) Tangent Modulus

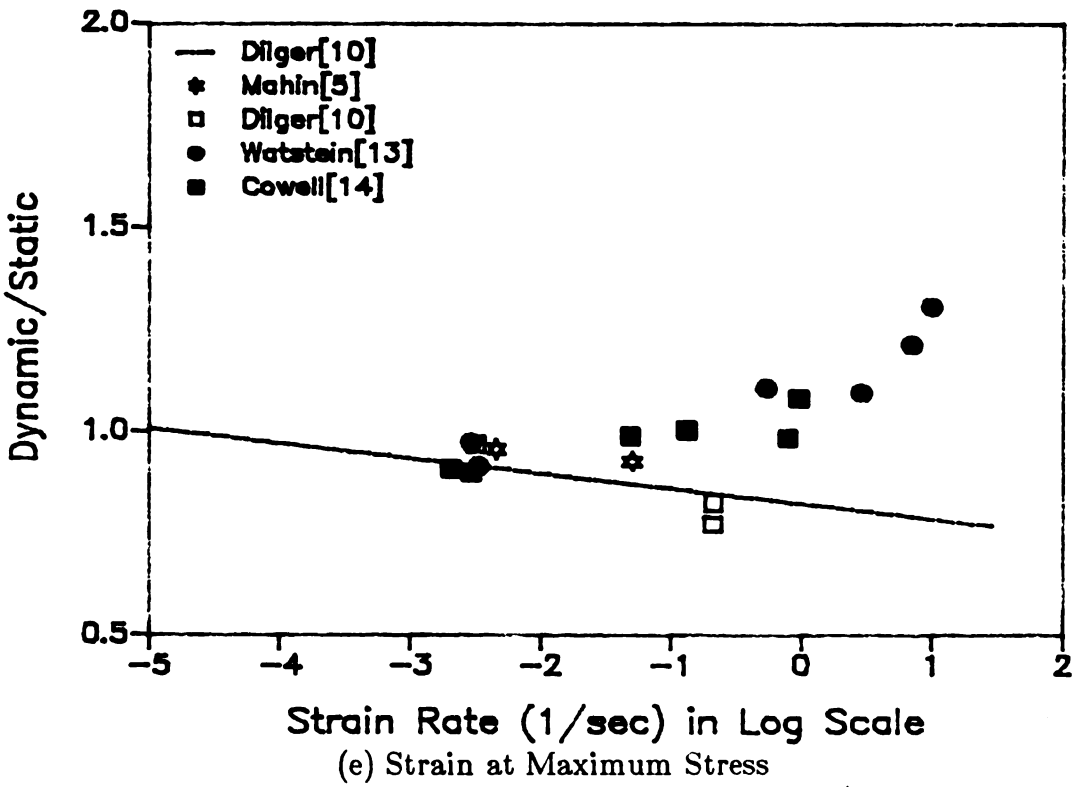

(e) Strain at Maximum Stress

Figure 2.2 Strain Rate-Sensitivity of The Concrete Mechanical Properties(cont'd)

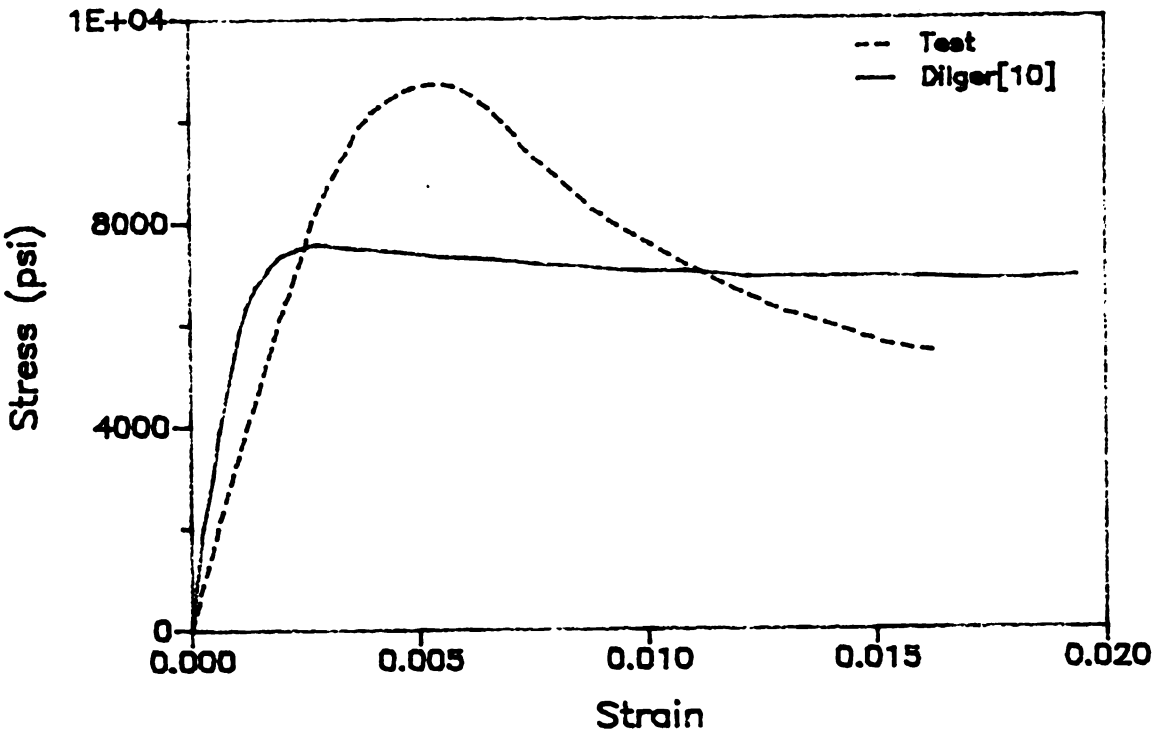

(f) Test versus Theory

Fifure 2.2 Strain Rate-Sensitivity of The Concrete Mechanical Properties(cont'd)

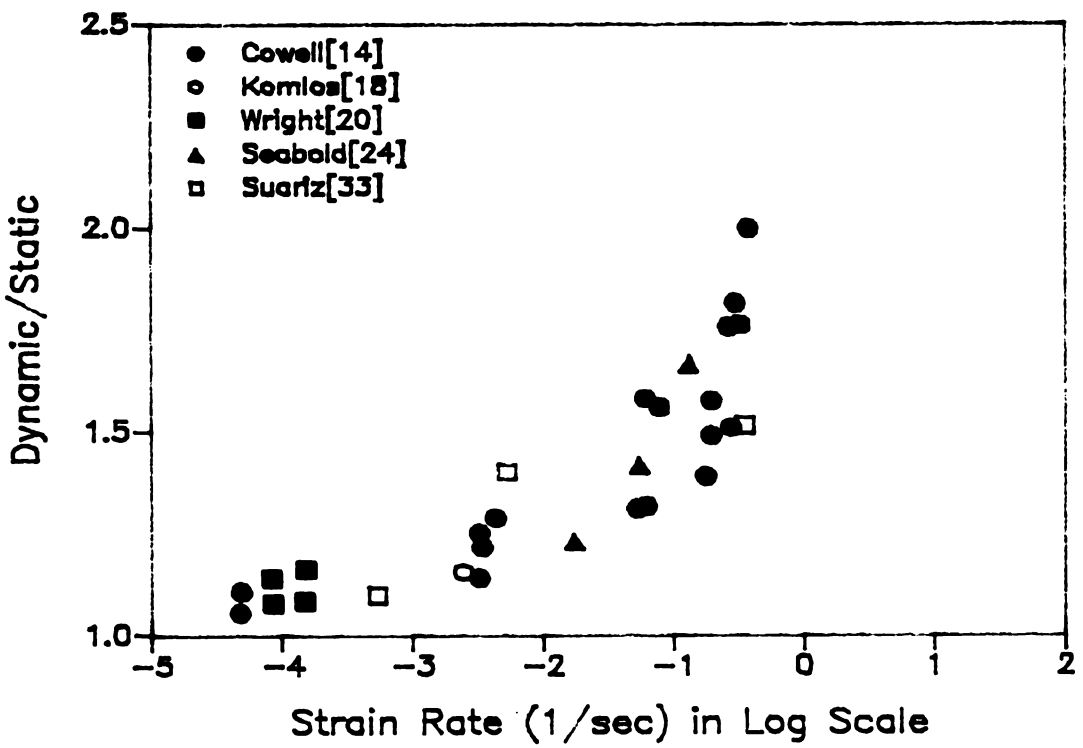

Figure 2.3 Strain Rate-Sensitivity of The Concrete Tensile Strength

Under seismic excitations, the concrete in the R/C structures is subjected to repeated compression at high strain rates. The available dynamic test results are, however, mainly concerned with the monotonic behavior of concrete, and studies on the strain rate-sensitivity of the concrete hysteretic behavior are scarce[15].

2.3 CONCRETE IN TENSION

The available test data on concrete tensile strength [12,14,17-20,24,33] are accumulated in Figure 2.3. Concrete tensile strength increases more rapidly than its compressive strength with increasing strain rate (compare Figures 2.2b and 2.3).

2.4 STEEL

As typically shown in Figure 2.4(a), the steel yield and ultimate stresses as well as its maximum yield plateau and ultimate strains increase with increasing strain rate[5,12,21-26]. The modulus of elasticity of steel is not, however, strain rate-sensitive. Figures 2.4(b) through 2.4(d) present accumulations of the test data available in the literature on the strain rate-sensitivity of the steel yield and ultimate stresses as well as its ultimate strain. The steel yield strength is seen to be more strain rate-sensitive than its ultimate strength. The strain rate-sensitivity of the steel yield strength has been found[12,22,25,26] to increase with decreasing steel strength as shown in Figure 2.5. This figure also presents the empirical expression derived in Reference 12 that does not compare well with the test data. Results of cyclic tests performed on steel at high strain rates are scarce, but the available data[5] show similar tendencies in the steel strain rate-sensitivity under monotonic and cyclic loads.

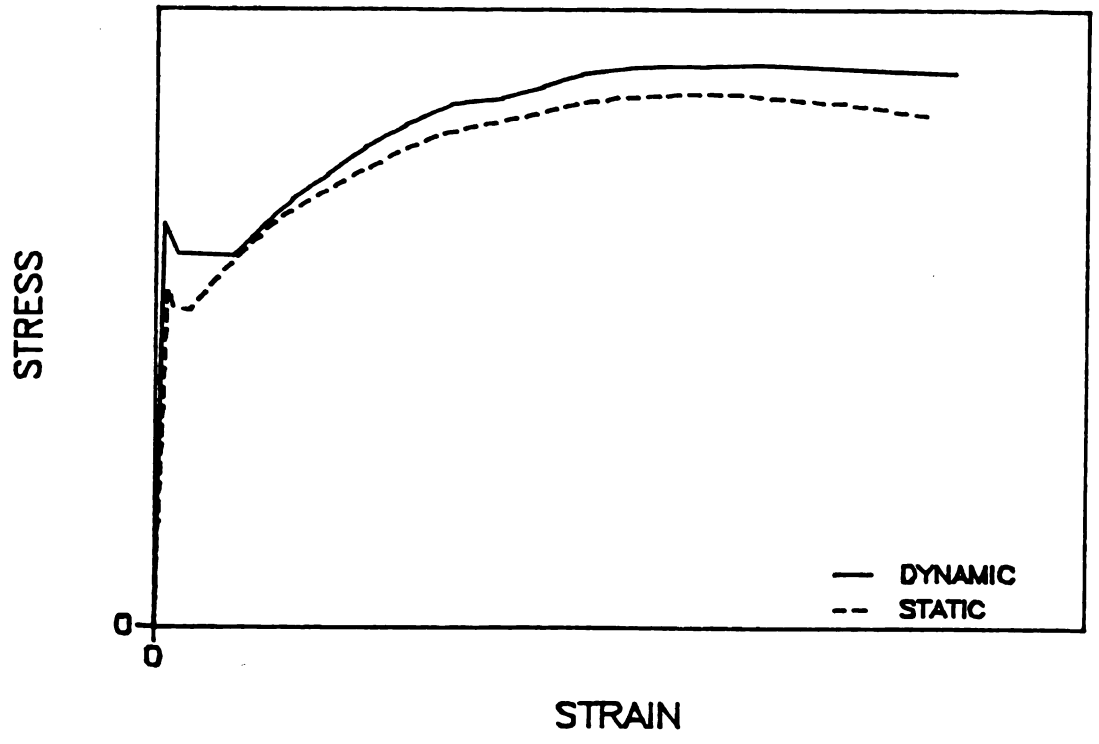

(a) Constitutive Diagram

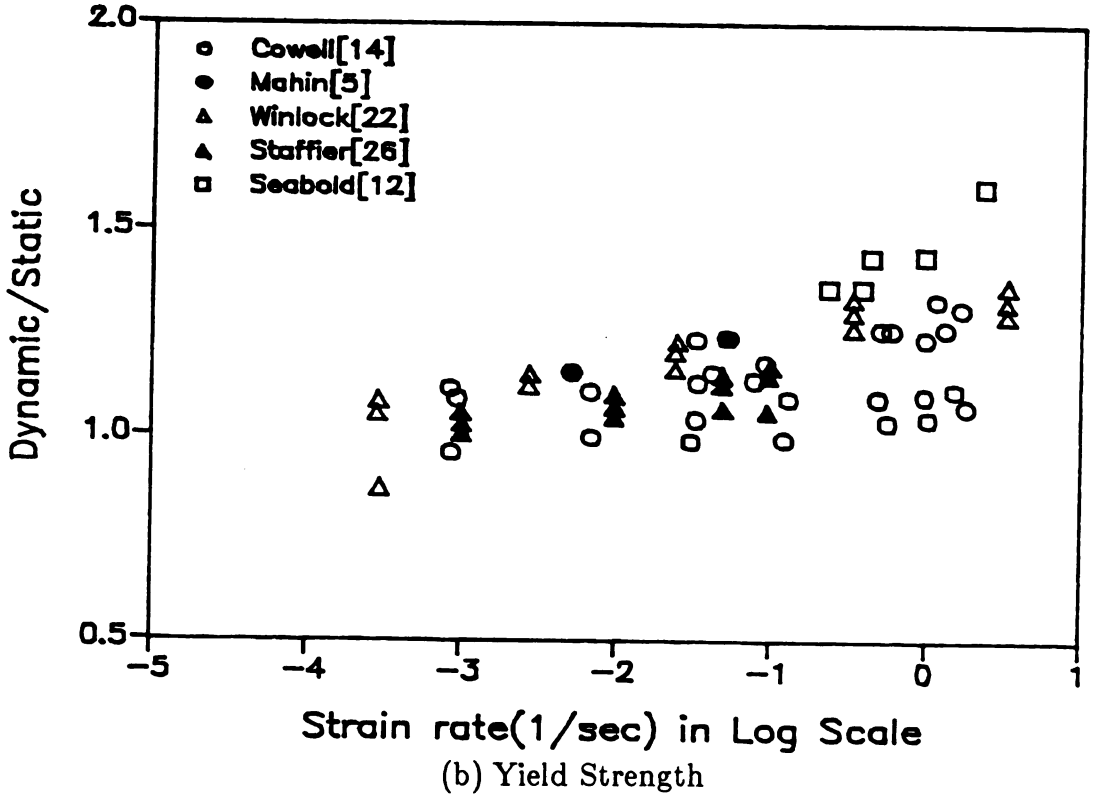

(b) Yield Strength

Figure 2.4 Strain Rate-Sensitivity of The Steel Mechanical Properties

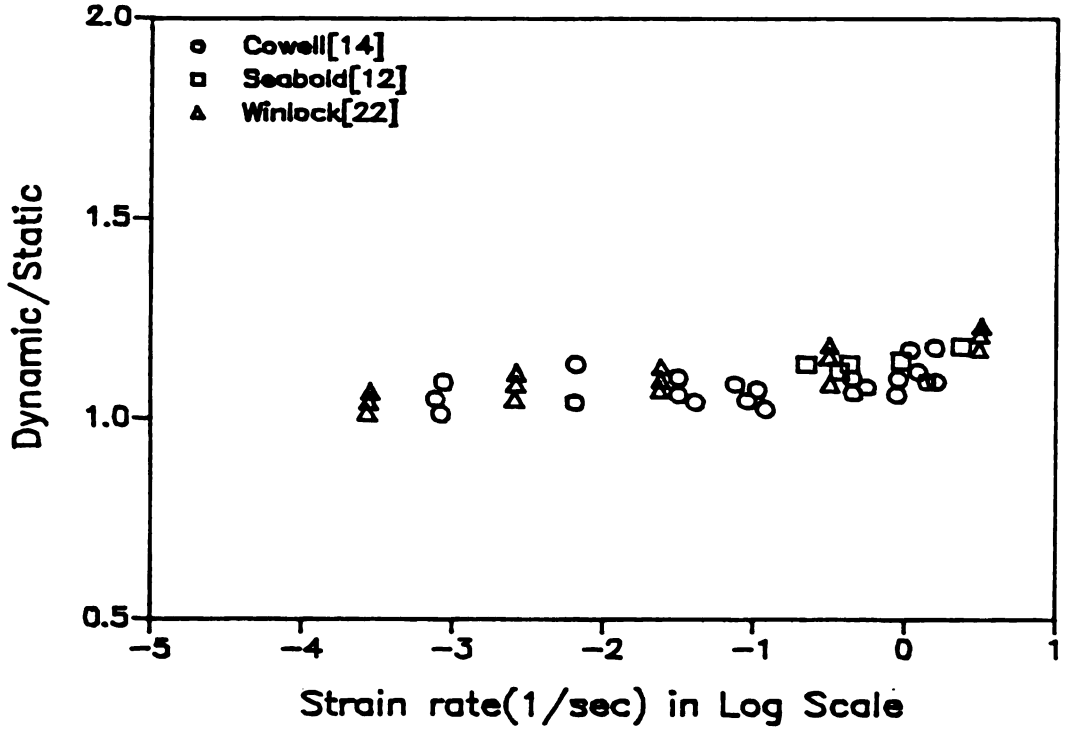

(c) Ultimate Strength

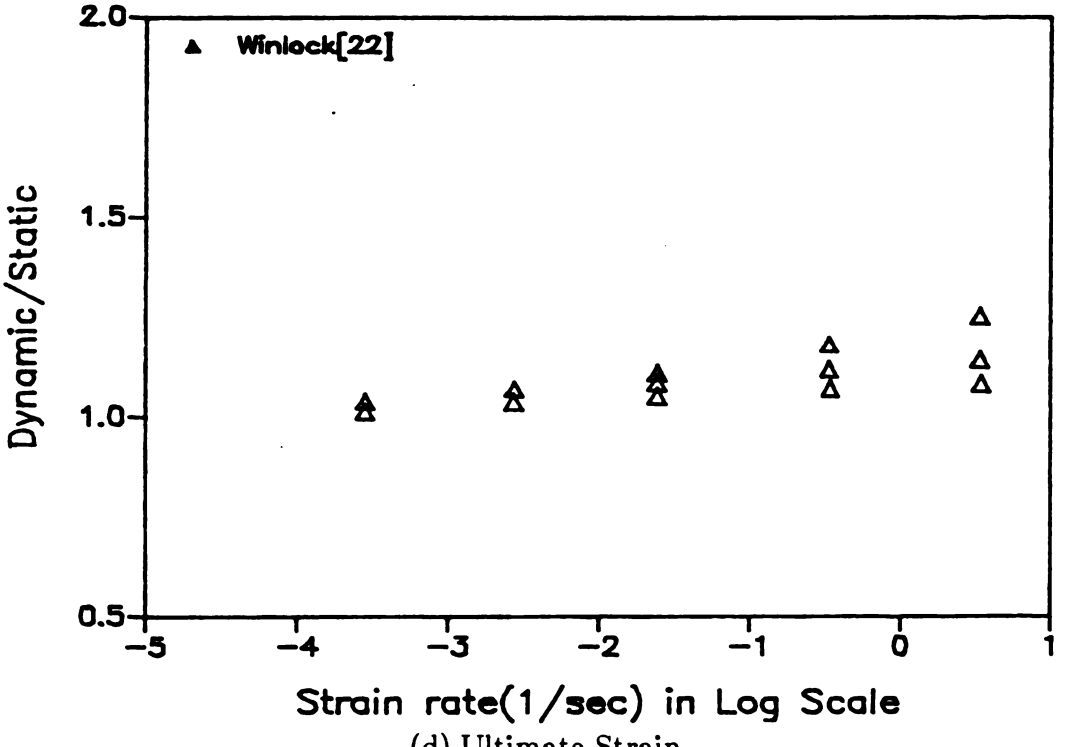

(d) Ultimate Strain

Figure 2.4 Strain Rate-Sensitivity of The Steel Mechanical Properties(cont'd)

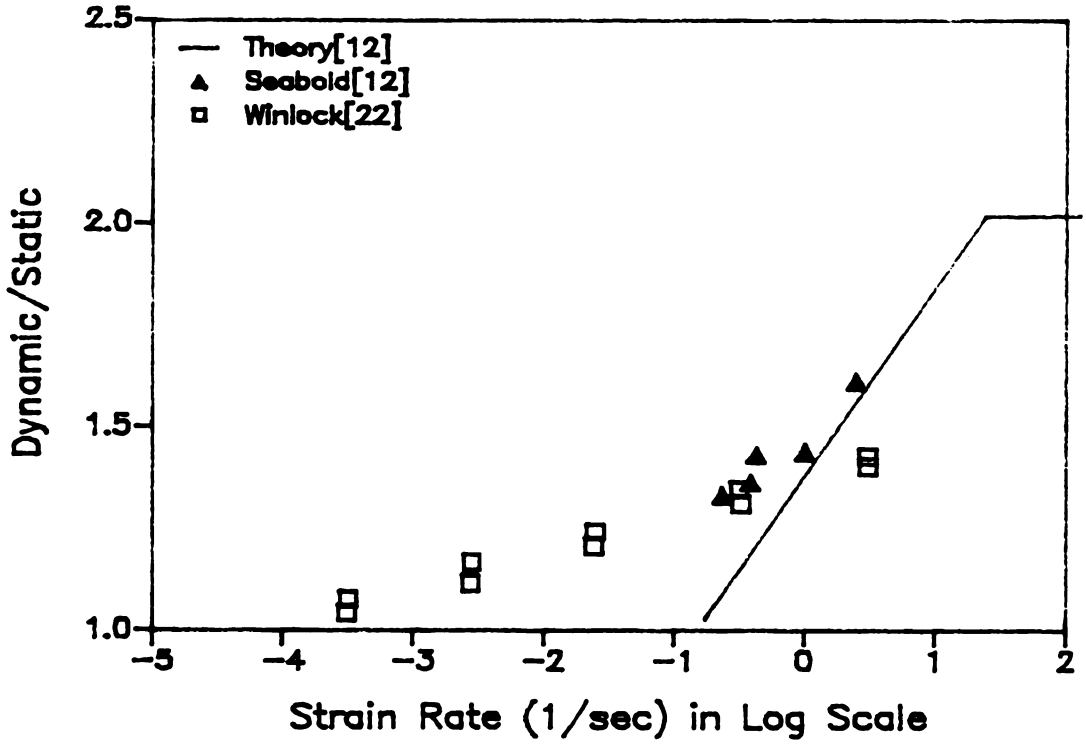

(a) f_y = 30,000 psi

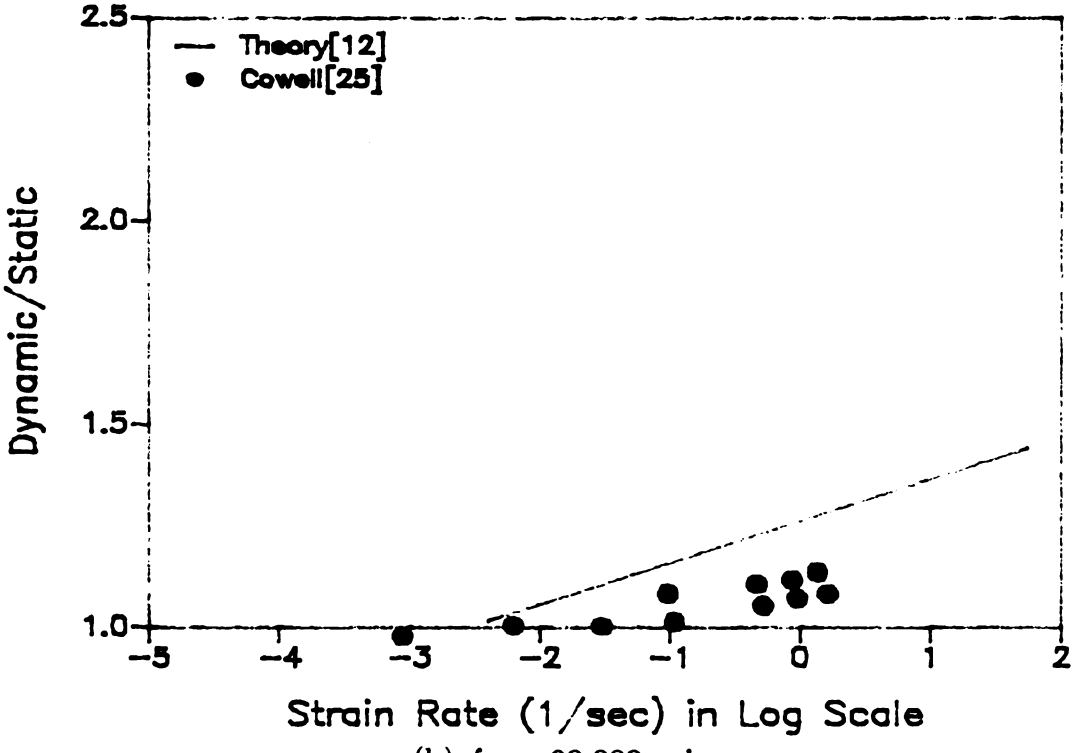

(b) f_y = 90,000 psi

Figure 2.5 Strain Rate-Sensitivity of The Steel Yield Strength

2.5 BOND BETWEEN STEEL AND CONCRETE

Monotonic test results have indicated that the characteristic bond stress values increase with increasing slip rate[26,34-36] (Figure 2.6). Cyclic test results on bond performed at high loading rates have not become available in the literature.

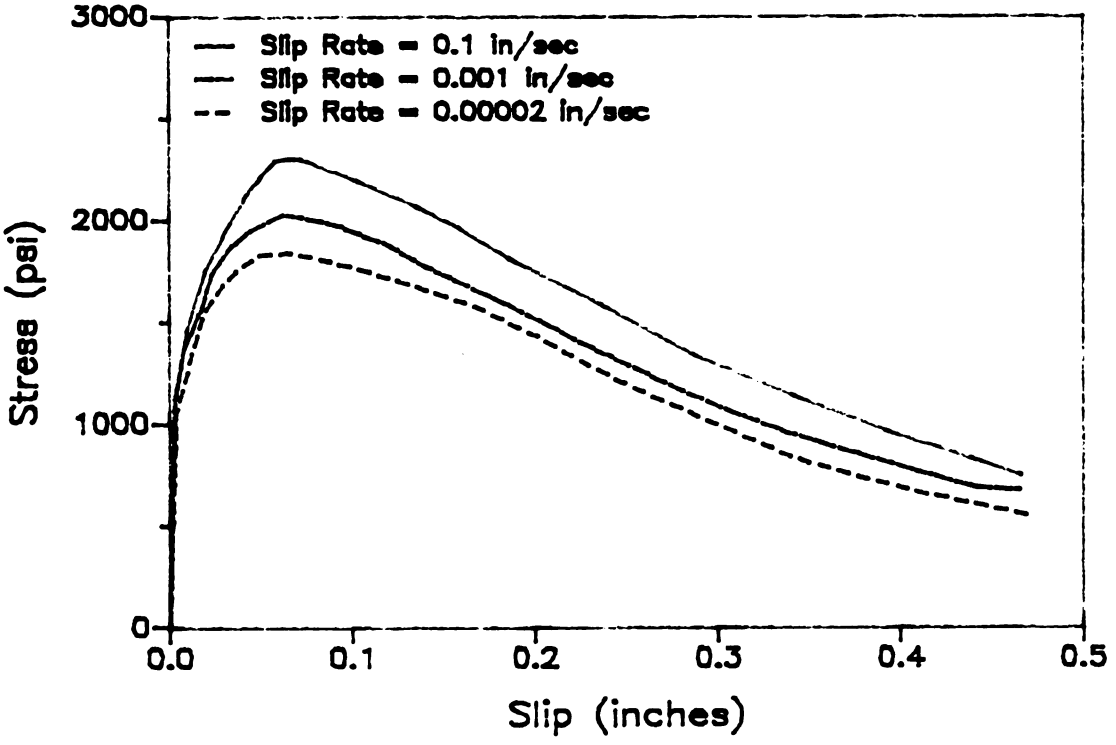

Fiure 2.6 Slip Rate-Sensitivity of Bond between Steel and Concrete

2.6 AXIAL-FLEXURAL BEHAVIOR OF THE R/C ELEMENTS

As shown in Figure 2.7(a), the axial-flexural strength and stiffness of the R/C beam-columns increased by about 20% as the rate of straining was raised from a quasi-static value to the seismic level in monotonic tests reported in Reference 4. The failure of the dynamically loaded elements has been also observed to be more

brittle[4,5,12,24].

As typically shown in Figure 2.7(b), in the available cyclic tests on R/C beams[5,8,28,37] also the flexural yield strength was observed to increase by about 20% as the quasi-static loading rate was increased to the seismic level. The strain rate effects become smaller after repetition of some large-amplitude inelastic cycles. A relatively small increase in the beam hysteretic energy absorption was also observed at higher strain rates.

In one of the very few analytical studies available in this area, Reference 45 has used layer models of the R/C sections to analytically produce their interaction diagrams at different strain rates. The results compared well with the available test data and it was confirmed that the ACI[9] equations give quasi-static values of the axial-flexural strength that are considerably smaller than the corresponding dynamic strengths (Figure 2.7c). The strain rates shown in Figure 2.7(c) belong to the extreme compressive concrete fiber.

2.7 SHEAR BEHAVIOR OF THE R/C ELEMENTS

Test results on simply supported R/C beams subjected to monotonic loads[12,24] have revealed that with increasing loading rate, the maximum shear force increases proportionally with the flexural strength, but the corresponding increase in shear strength is less pronounced. Hence, in some tests the beams had sufficient web reinforcement to force flexural yielding prior to shear failure when loaded statically, but not enough to cause that sequence of failure modes in the dynamic loading case. It was also observed that the share of the web reinforcement in resisting shear increases and the shear failure becomes more brittle as the loading rate increases.

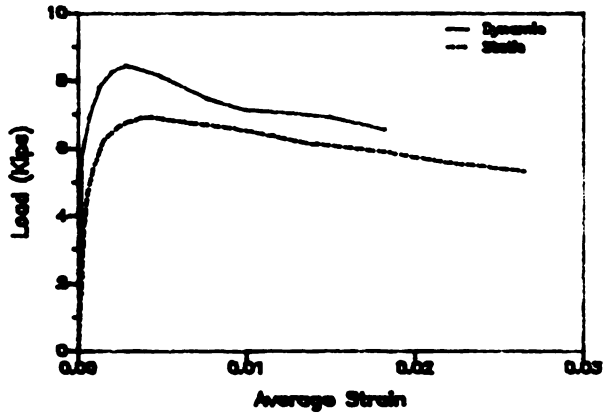

(a) Monotonic Constitutive Behavior

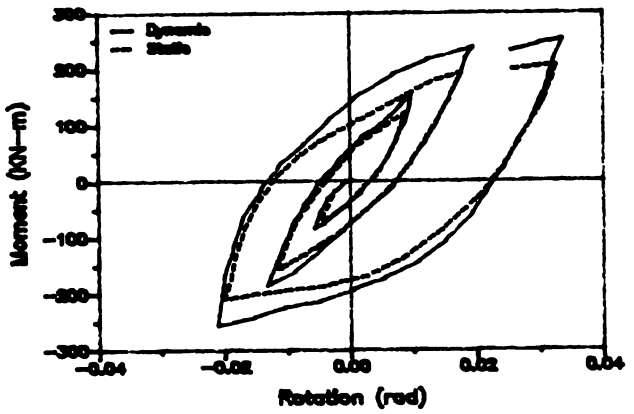

(b) Hysteretic Behavior

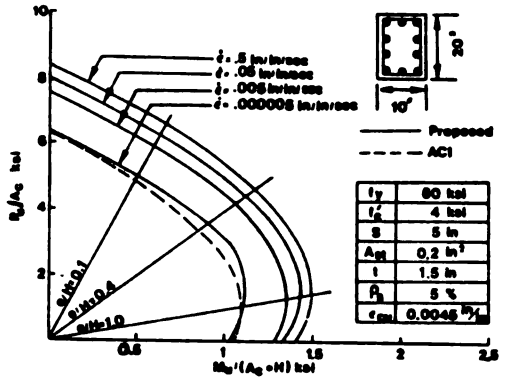

(c) Interaction Diagrams

Figure 2.7 Strain Rate-Sensitivity of The Axial-Flexural Behavior of The R/C Elements

Reference 33 has reported experimentally derived static and dynamic shear load-deformation diagrams of cyclically loaded cantilever beams with shear span-to-depth ratios of about 3 (Figure 2.8). Shear stiffness degradation in these tests was found to be smaller at higher loading rates.

Comprehensive analytical studies on the strain rate-sensitivity of the shear strength and deformation characteristics of the R/C elements have not been reported in the literature.

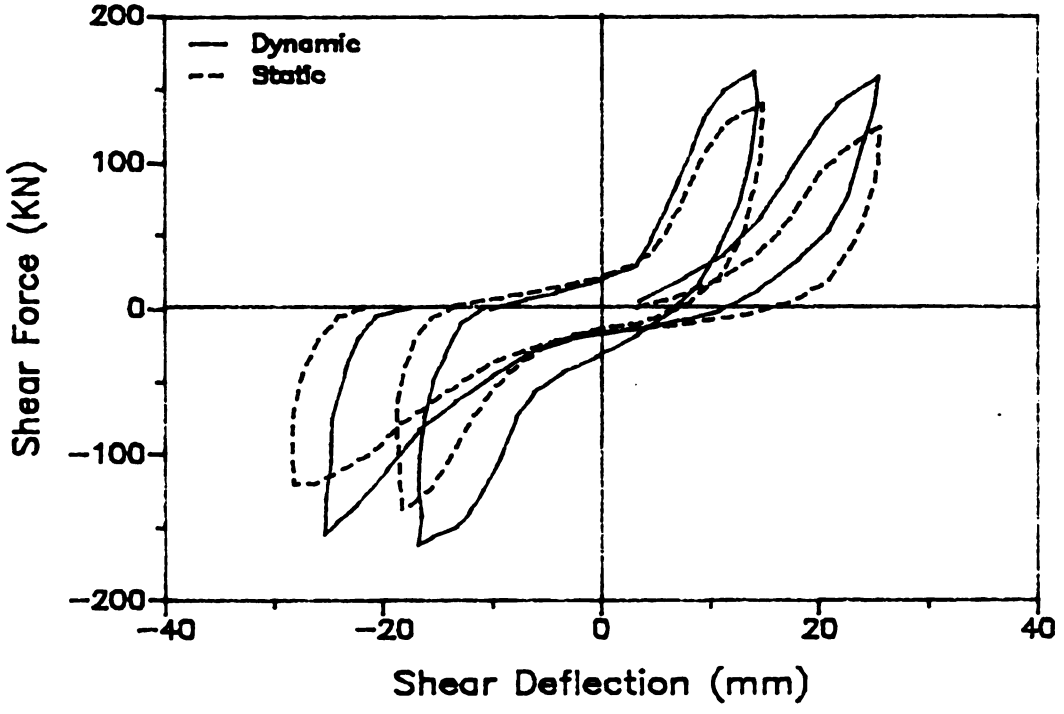

Figure 2.8 Strain Rate-Sensitivity of An R/C Beam Shear Hysteresis

CHAPTER 3

A STRAIN RATE-SENSITIVE CONSTITUTIVE MODEL FOR CONCRETE UNDER COMPRESSION

3.1 INTRODUCTION

Dynamic compression tests on confined and unconfined concrete have shown that as the strain rate increases

(1) the compressive strength, secant modulus of elasticity, and slope of the descending branch in the concrete stress-strain diagram increase, and

(2) the maximum strain at failure decreases while the strain at maximum stress might decrease[10] or increase[4] depending on the rate of straining.

The strain rate effects are found to decrease with evaporation of the moisture in concrete. Some investigators have also suggested that the strain rate effects are more significant on high strength concrete, while others have concluded from their test results that the concrete compressive strength has no influence on the strain rate effects[11,12].

In this chapter, a constitutive model for confined and unconfined concrete subjected to dynamic compression is proposed. This model is based on numerous measurements of the maximum stress and strain at maximum stress in tests performed by different investigators at different strain rates. The proposed model

accounts for the confinement effects and distinguishes between the strain rate effects on air-dried and saturated concrete. It also compares well with the available test results.

3.2 COMPRESSIVE STRENGTH

Test results on the dynamic compressive strength of concrete have been reported in References 4, 5, 10, 11, 13, 14, 15 and 33. These experimental studies have covered wide ranges of compressive strength (1,000 to 7,500 psi), moisture content (air-dried and saturated), confinement condition (plain, tied, and spirally reinforced), and age at test (3 to 49 days). In most of the tests the strain rate has been measured, but some studies have reported only stress rate measurements. In these cases, the strain rates were derived by dividing the stress rates into the concrete modulus of elasticity. The errors of this transformation were judged to be acceptable, because the strain rate effects are not sensitive even to errors of the order of 50 percent in the strain rate measurements (strain rate effects become apparent after changes of an order of magnitude in strain rate). Figure 3.1(a) presents a plot of the ratios of the dynamic to static compressive strengths versus the rate of straining during the test. Each point in this figure is an average of about three tests. This figure also shows three curves, two of which have been based on the expressions proposed by Dilger[10] and Seabold[12], for the strain rate effect on the compressive strength of concrete:

$$Dilger: \frac{f_{cd}}{f_{cs}} = 1.38 + 0.08\log_{10}\dot{\epsilon} \tag{3.1}$$

$$Seabold: \frac{f_{cd}}{f_{cs}} = 1.17 + 0.173\dot{\epsilon} + 0.06\log_{10}\dot{\epsilon} \tag{3.2}$$

where, $1 \leq \frac{f_{cd}}{f_{cs}} \leq 2$

The third curve, proposed in this study, has resulted from least-square curve fitting of a second-degree polynominal (in terms of $\log_{10}\dot{\epsilon}$) to the test results reported by different investigators. For all tests,

$$\frac{f_{cd}}{f_{cs}} = 1.48 + 0.160\log_{10}\dot{\epsilon} + 0.0127(\log_{10}\dot{\epsilon})^2 \tag{3.3}$$

where,

f_{cd} = dynamic compressive strength;
f_{cs} = static compressive strength (at a atrain rate of 10^{-5}/sec); and
$\dot{\epsilon}$ = strain rate (1/sec) $\geq 10^{-5}$

A wide scatter of the tests results is observed in Figure 3.1(a). The main source of the scatter was found to be the variation in the moisture content of concrete. Figures 3.1(b) and (c) show the results of tests on air-dried and saturated concrete, respectively. It can be concluded from these figures that the strain rate effect on increasing the concrete compressive strength becomes more significant as the concrete moisture content increases. The following expressions (also shown in Figures 3.1b and c) were derived by least square curve fitting to the test results on air-dried and saturated specimens:

For air-dried concrete,

$$\frac{f_{cd}}{f_{cs}} = 1.48 + 0.206\log_{10}\dot{\epsilon} + 0.0221(\log_{10}\dot{\epsilon})^2 \tag{3.4}$$

For saturated concrete,

$$\frac{f_{cd}}{f_{cs}} = 2.54 + 0.580\log_{10}\dot{\epsilon} + 0.0543(\log_{10}\dot{\epsilon})^2 \tag{3.5}$$

The available test results did not show any considerable influence from the compressive strength on the strain rate effects. For example, Figures 3.1(d) and (e) compare the strain rate effets on low strength ($f_{cs} \leq 4{,}000$psi) and high strength ($f_{cs} > 4{,}000$psi) air-dried concrete. These figures show that the results

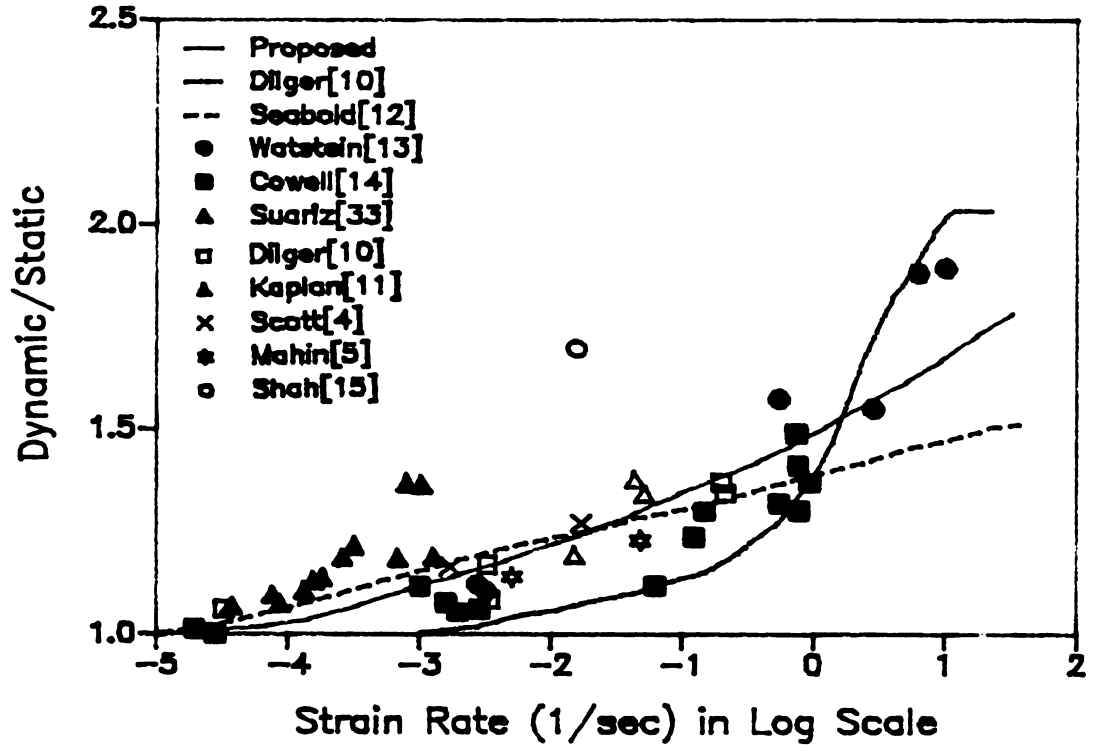

(a) General Concrete Tests

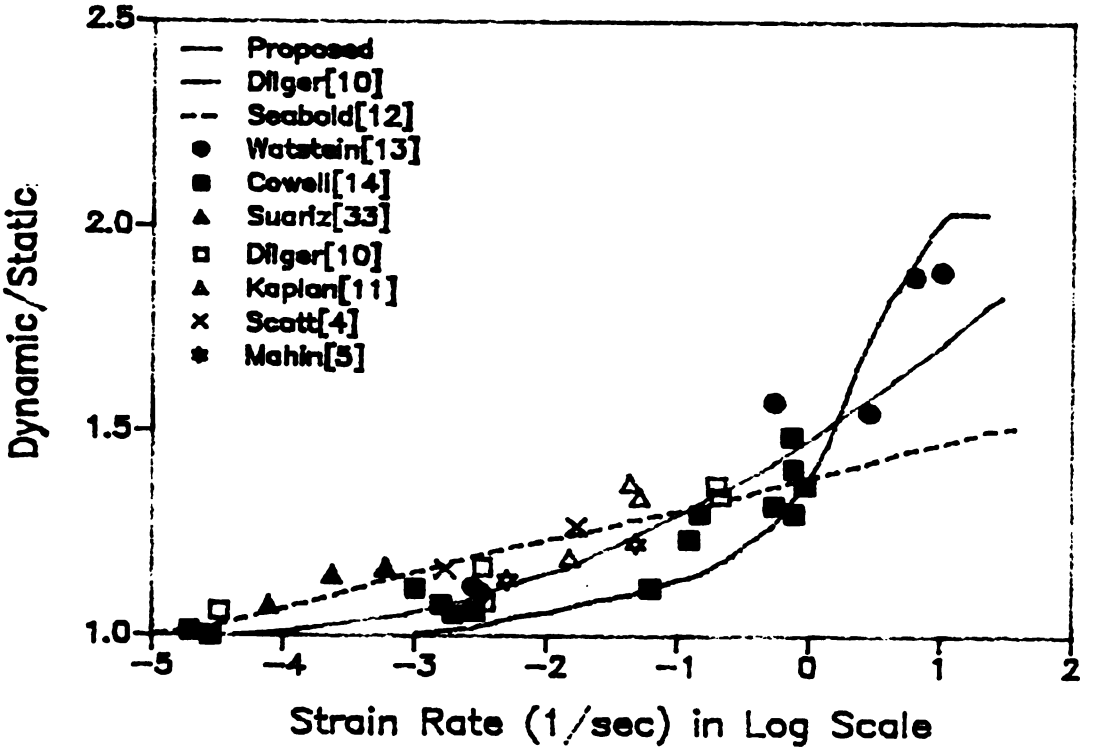

(b) Air-Dried Concrete Tests

Figure 3.1 Strain Rate Effects on The Compressive Strength of Concrete

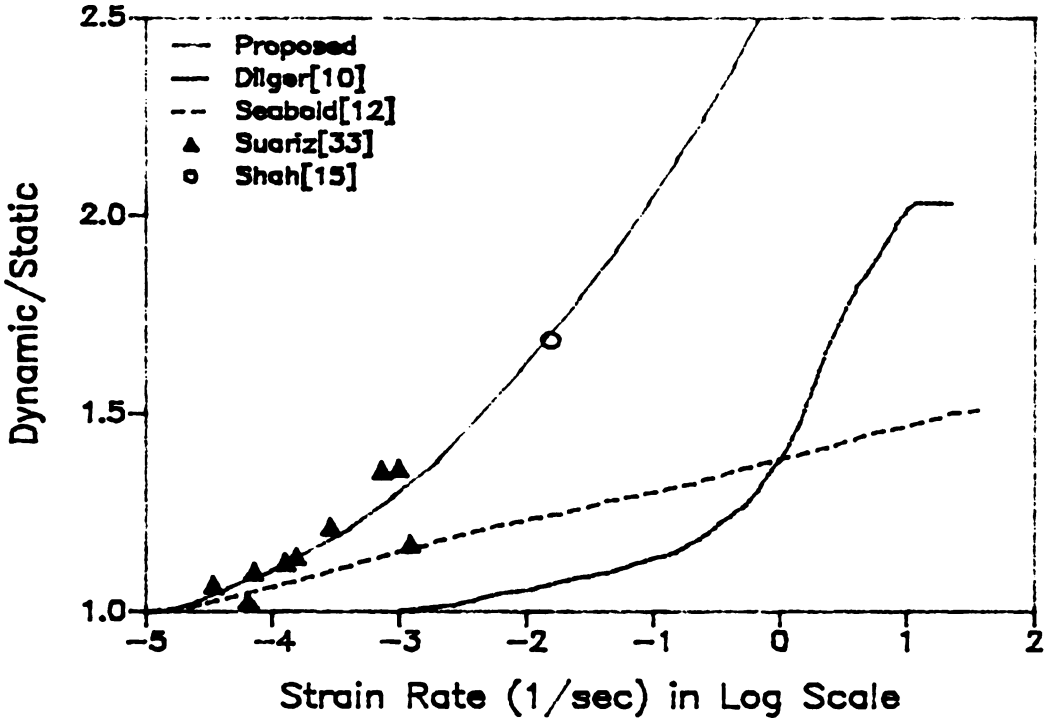

(c) Saturated Concrete Tests

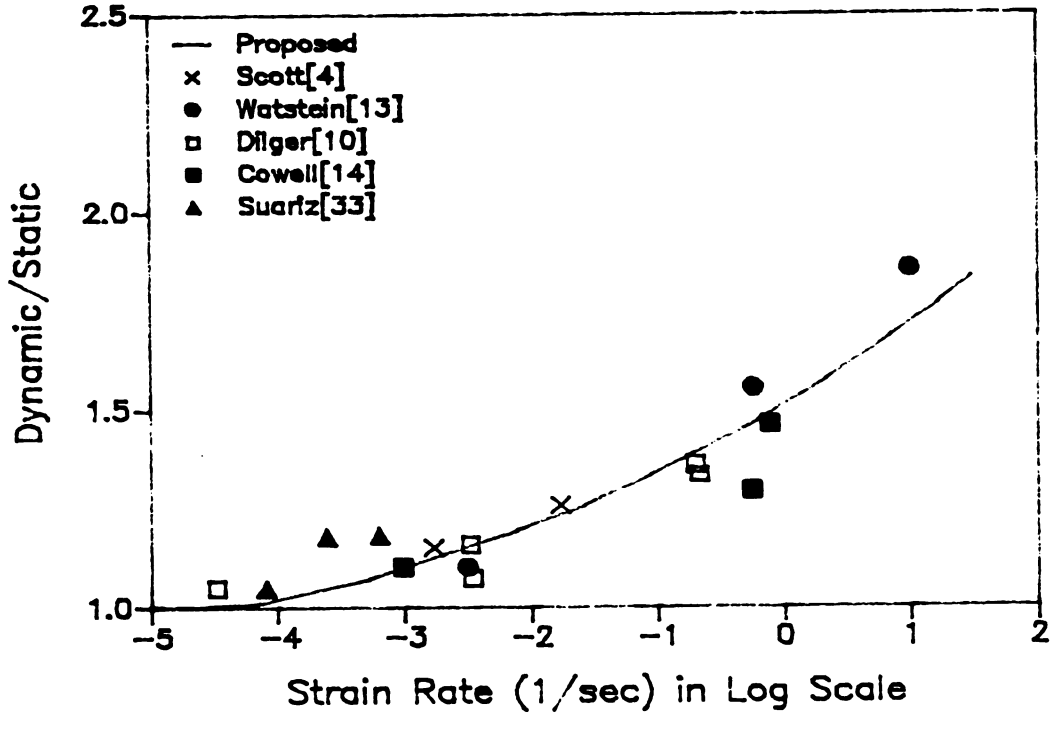

(d) Air-Dried Concrete with $f_{cs} \leq 4{,}000$ psi

Figure 3.1 Strain Rate Effects on The Compressive Strength of Concrete(cont'd)

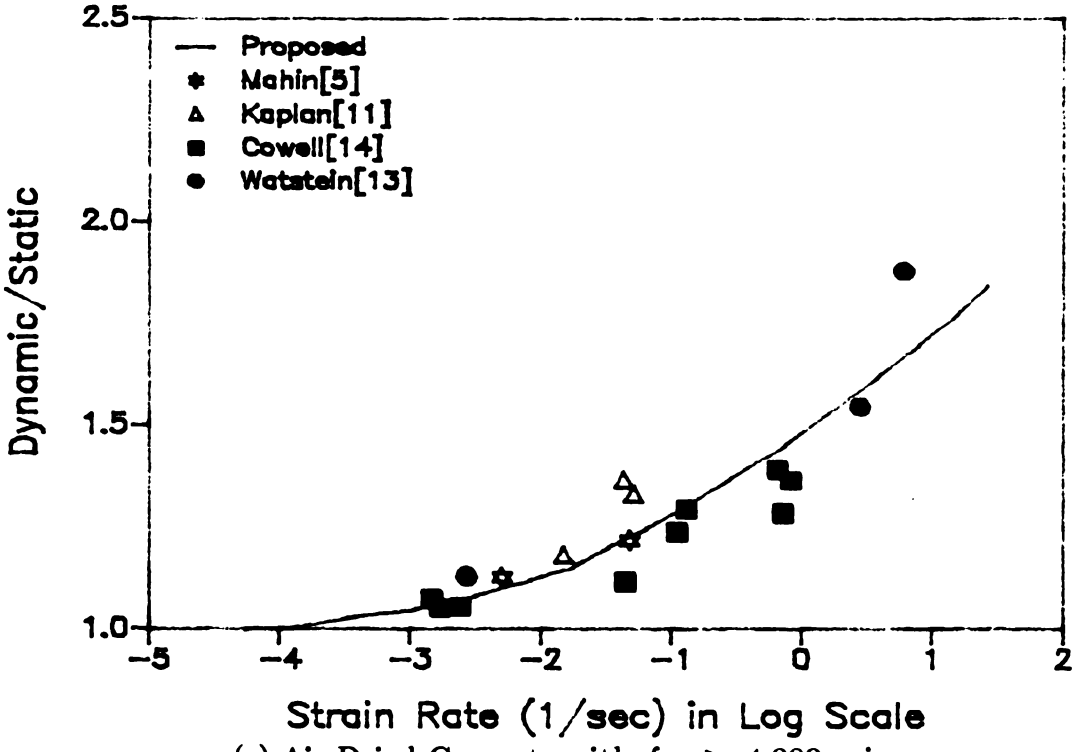

(e) Air-Dried Concrete with $f_{cs} > 4{,}000$ psi

Figure 3.1 Strain Rate Effects on The Compressive Strength of Concrete(cont'd)

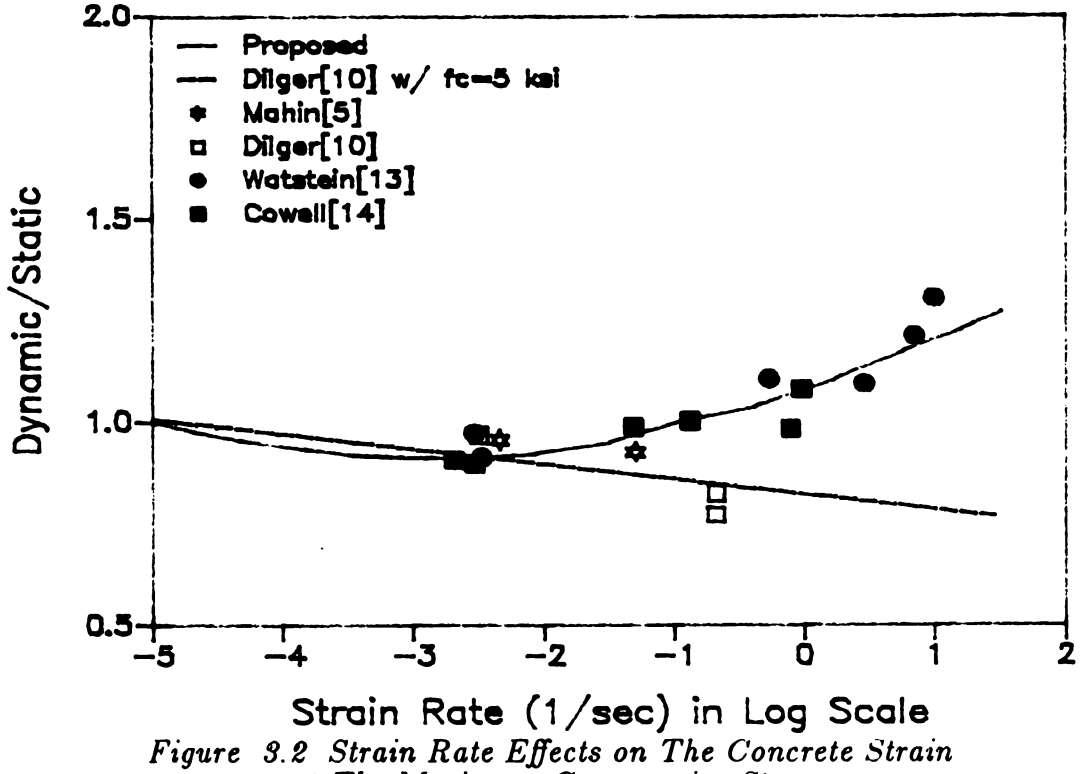

Figure 3.2 Strain Rate Effects on The Concrete Strain at The Maximum Compressive Stress

of curve fitting to the test data are very similar for different concrete strengths. The strain rate effect on concrete compressive strength was also found to be independent of the age of the specimens if their moisture contents are similar.

As far as the confinement effects are concerned, very few of the test programs have studied confined concrete, and thus no final conclusion can be drawn at this point. The few available confined test results, however, do not show any significant influence from confinement on the strain rate effects.

3.3 STRAIN AT MAXIMUM STRESS

As mentioned earlier, in some tests[4] when the strain rate was increased the value of the concrete strain at maximum compressive stress increased while in some other tests[10] it decreased. Figure 3.2 shows the strain rate effect on the strain at maximum stress in the tests reported in References 5, 10, 13 and 14. Each point in this figure represents the average of about 3 test results. In this figure, ϵ_{od} is the dynamic strain at maximum stress and ϵ_{os} is the static strain at maximum stress.

According to the available test results shown in Figure 3.2, increasing the strain rate from the static value of 10^{-5}/sec to values as high as 10^{-1}/sec results in reduced values of strain at maximum stress. At strain rates higher than 10^{-1}/sec, however, the concrete strain at maximum stress becomes larger than the static value. A considerable scatter of test results is evident in this figure.

Figure 3.2 also presents the equation proposed by Dilger[10] as well as the one derived in this study. Dilger's equation is a function of the concrete compressive strength and is based on the assumption that the concrete strain at maximum compressive stress decreases linearly with the increasing strain rate:

$$\frac{\epsilon_{od}}{\epsilon_{os}} = (1.3 - 0.06\log_{10}\dot{\epsilon} + 0.00007 f_c^{'})/(1.6 + 0.00007 f_c^{'}) \tag{3.6}$$

where,

$f_c^{'}$ = 28-day quasi-static compressive strength of concrete in psi.

The proposed equation given below was derived by least square curve fitting, using all the experimental data shown in Figure 3.2:

$$\frac{\epsilon_{od}}{\epsilon_{os}} = 1.08 + 0.112\log_{10}\dot{\epsilon} + 0.0193(\log_{10}\dot{\epsilon})^2 \tag{3.7}$$

As far as the effects of concrete moisture content, compressive strength, and confinement on the dynamic strain at maximum stress are concerned, the available test results are inadequate to derive meaningful conclusions.

3.4 MODULUS OF ELASTICITY

Figures 3.3(a) and (b) present the strain rate effects on the compressive secant and tangent moduli of elasticity of concrete as observed in the test results reported in References 13, 14, and 33. The secant modulus was found at a compressive stress equal to 0.45 $f_c^{'}$, and the tangent modulus was measured at the origin. Compared to the secant modulus of elasticity, the tangent modulus is found to be less influenced by the rate of straining. The following expressions were derived by least square curve fitting to the test results presented in Figures 3.3(a) and (b):

$$\frac{E_{cd}}{E_{cs}} = 1.241 + 0.111\ \log_{10}\dot{\epsilon} + 0.127(\log_{10}\dot{\epsilon})^2 \tag{3.8}$$

$$\frac{E_{td}}{E_{ts}} = 1.061 + 0.464\ \log_{10}\dot{\epsilon} + 0.00683(\log_{10}\dot{\epsilon})^2 \tag{3.9}$$

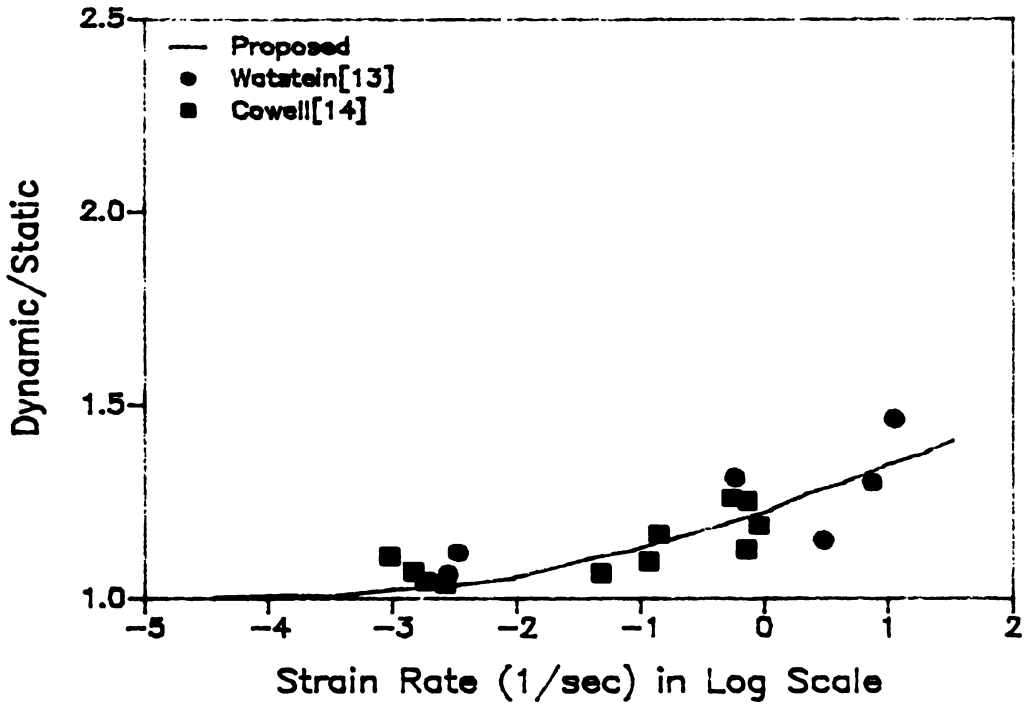

(a) Secant Modulus

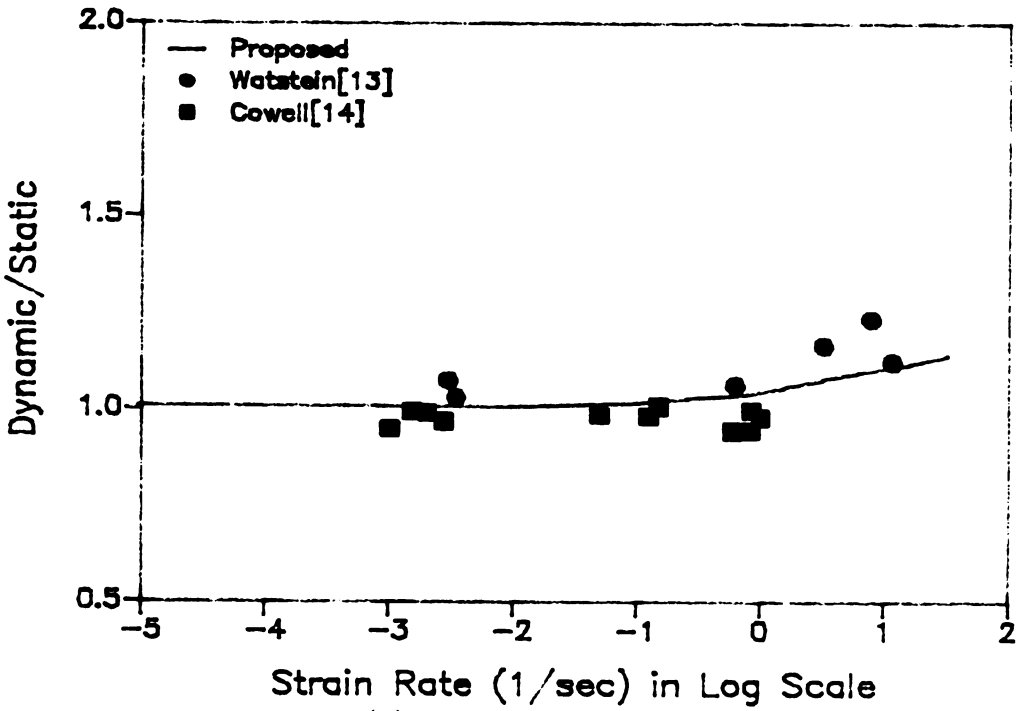

(b) Tangent Modulus

Figure 3.3 Strain Rate Effects on The Concrete Modulus of Elasticity

where,

E_{cd} = dynamic secant modulus of elasticity;
E_{cs} = static secant modulus of elasticity;
E_{td} = dynamic tangent modulus of elasticity; and
E_{ts} = static tangent modulus of elasticity.

No conclusion could be derived from the available test results regarding the effects of moisture content, compressive strength, and confinement on the dynamic moduli of elasticity.

3.5 THE CONSTITUTIVE MODEL FOR CONCRETE

The following constitutive model (Figure 3.4) is based on Equations (3.8) and (3.9), which were derived from a relatively large number of dynamic compressive test results reported by different investigators:

$$f = \begin{cases} K_1 K_2 f_c' \left[\dfrac{2\epsilon}{0.002 K_1 K_3} - \left(\dfrac{\epsilon}{0.002 K_1 K_3} \right)^2 \right] \\ \qquad \text{for } \epsilon \leq 0.002 K_1 K_3 \\ K_1 K_2 f_c' \left[1 - z(\epsilon - 0.002 K_1 K_3) \right] \geq 0.2 K_1 K_2 f_c' \\ \qquad \text{for } \epsilon > 0.002 K_1 K_3 \end{cases} \tag{3.10}$$

where,

f = concrete compressive stress;
ϵ = concrete compressive strain;
$K_1 = 1 + \dfrac{\rho_s f_{yh}}{f_c'}$;
ρ_s = volumetric ratio of transverse reinforcement to concrete core;
f_c' = 28-day compressive strength of concrete;

f_{yh} = yield strength of transverse reinforcement;

$$z = \frac{0.5}{\frac{3 + 0.002 f_c'}{f_c' - 1000} + \frac{3}{4}\rho_s \left(\frac{h'}{s}\right)^{1/2} - 0.002 K_1 K_3}$$

h' = width of concrete core measured to outside of the transverse reinforcement;

s = center to center spacing of transverse reinforcement;

$$K_2 = \begin{cases} 2.54 + 0.580 \log_{10}\dot{\epsilon} + 0.0543(\log_{10}\dot{\epsilon})^2 & \text{for saturated concrete} \\ 1.48 + 0.160 \log_{10}\dot{\epsilon} + 0.0127(\log_{10}\dot{\epsilon})^2 & \text{for air-dried concrete} \end{cases}$$

$$K_3 = 1.08 + 0.112 \log_{10}\dot{\epsilon} + 0.0193(\log 10\dot{\epsilon})^2$$

(Note : *For* $\dot{\epsilon} < 10^{-5}/sec$, $K_2 = K_3 = 1.0$)

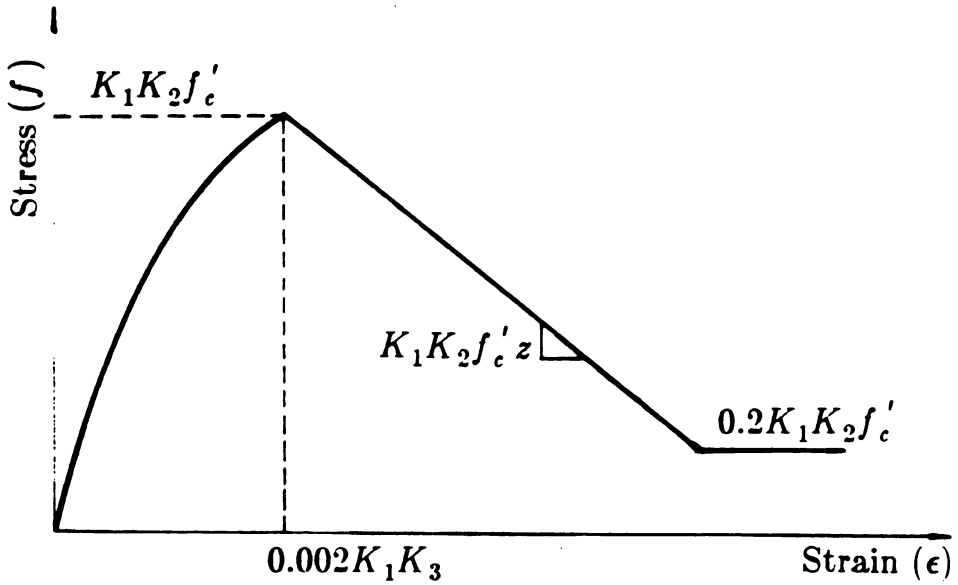

Figure 3.4 The Constitutive Model for Concrete under Compression

In this model, K_2 represents the strain rate effect on the compressive strength of concrete [Equations (3.3), (3.4) and (3.5)], and K_3 takes care of the strain rate effect on the concrete strain at maximum stress [Equation (3.7)]. In deriving this

model, it was assumed that the strain rate effect on the slope of the descending branch of the stress-strain diagram is similar to the strain rate effect on the compressive strength of concrete. Test results presented in Reference 10 support this assumption. The basic static stress-strain relationship in this model is taken from Reference 4.

The formulation does not specify a maximum strain at failure. Test results have shown that, especially for unconfined concrete, the failure strain tends to decrease as the strain rate increases[10], but the available experimental data are insufficient for a quantitative assessment of this strain rate effect. The constitutive model given above closely predicts the strain rate effect on the secant modulus of elasticity, while it overestimates the strain rate effect on the initial tangent modulus (which is not usually considered as an important property of concrete).

3.6 COMPARISON WITH TEST RESULTS AND PARAMETRIC STUDIES

The advantages of the strain rate-dependent constitutive model given in Equation (3.10) over the one proposed in Reference 10 are:

(1) its simplicity and stability,

(2) its generality, in the sense that it was derived using more test results reported by different investigators,

(3) its capability to distinguish between the strain rate effects on air-dried and saturated concretes, and

(4) its more accurate consideration of the confinement effects.

Some of these advantages are shown in Figure 3.5(a), which compares the predictions of the model given by Equation (3.10) and the constitutive model of Refer-

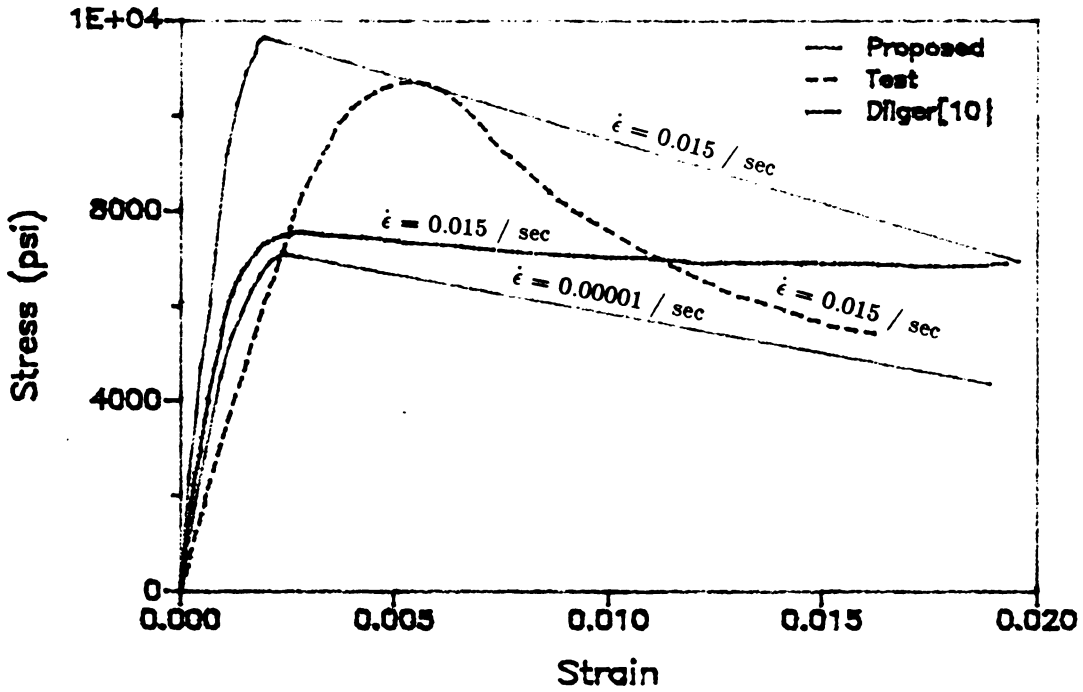

(a) Spirally Reinforced Saturated Concrete

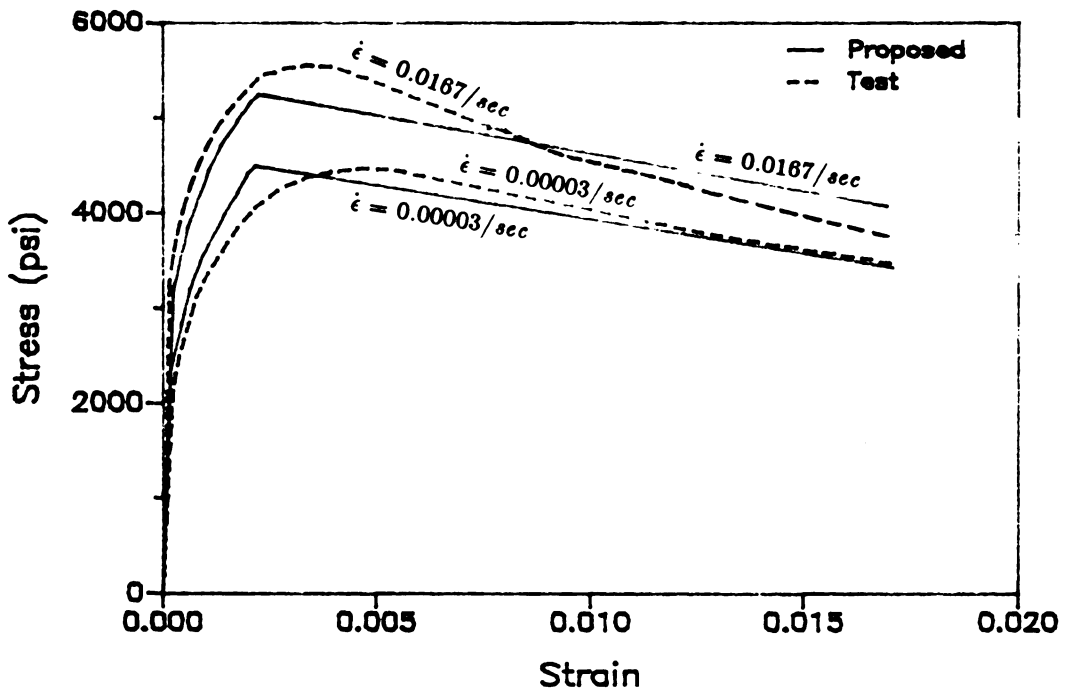

(b) Tied Air-Dried Concrete

Figure 3.5 Comparison of The Proposed Constitutive Model with Test Results

ence 16 with a test result performed on a spirally reinfoced saturated concrete subjected to a dynamic compressive strain rate of 0.0015/sec[15]. The static compressive strength of the 3 in. by 6 in. cylindrical specimen tested in Reference 9 was 6,000 psi, and it was spirally reinfoced having 1/8 in. diameter wires with a yield strength of 60,000 psi and a pitch of 1 in. This specimen had practically no cover. It is clear that the Dilger's model[10] underestimates the strain rate effect on the compressive strength of saturated concrete and also overestimates the confinement effect on reducing the slope of the descending branch of the stress-strain diagram. Figure 3.5(a) also shows the quasi-static constitutive diagram of concrete as predicted by Equation (3.10), which is observed to compare with test results far better than the other available model. The proposed model [Equation (3.10)] also compares well in Figure 3.5(b) with concrete constitutive diagrams obtained in quasi-static and dynamic tests on columns with a 17.7 in. square cross section reported in Reference 4. The air-dried concrete in these clolumns had a compressive strength of 3,600 psi and was confined by 0.39 in. ties with a yield strength of 44,800 psi and a volumetric ratio of 0.0182. The cover thickness in the tested specimens was 1.6 in.

Figure 3.6 compares the predictions of the proposed model given by Equation (3.10) with the test results on air-dried, unconfined specimens tested at two different strain rates[5]. The theoretical and experimental results are close. The discrepancy between the theoretical and experimental values of strain at maximum stress in Figures 3.5(a) and 3.6 seems to have resulted from the considerable scatter of the test data in Figure 3.2.

The more significant effect of strain rate on saturated concrete when compared with air-dried concrete is shown in Figure 3.7. This figure compares the static and dynamic constitutive diagrams predicted by Equation (3.10) for air-dried and saturated concretes with a compressive strength of 3,670 psi. The

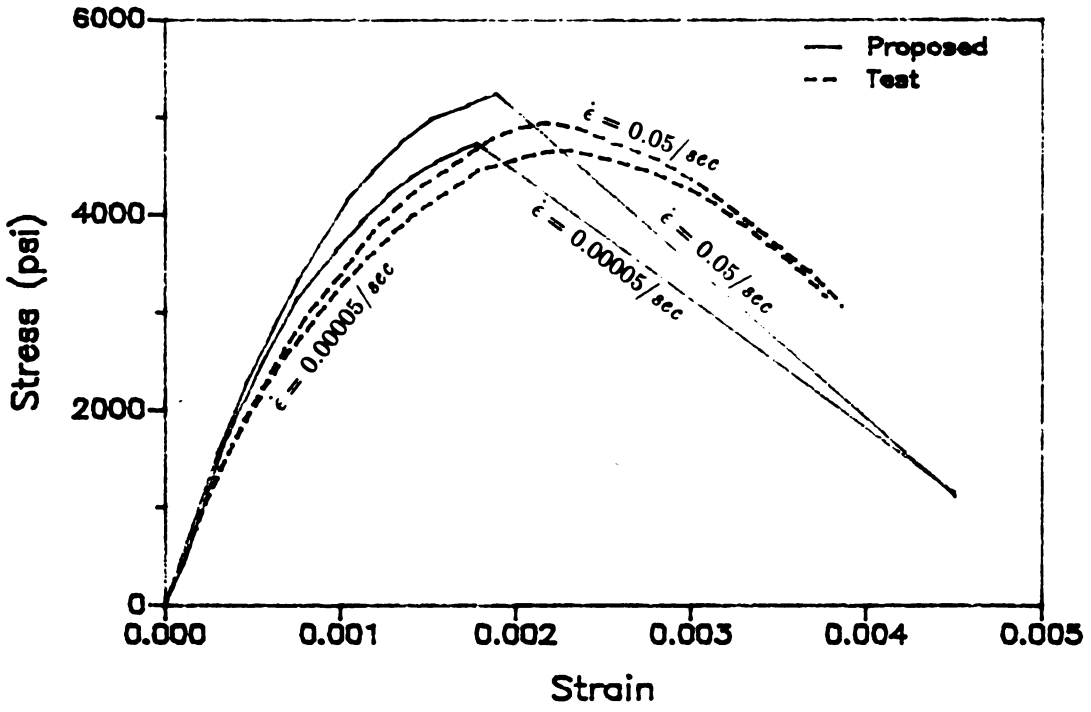

Figure 3.6 Theoretical and Experimental Constitutive Diagrams for Air-Dried Unconfined Specimens

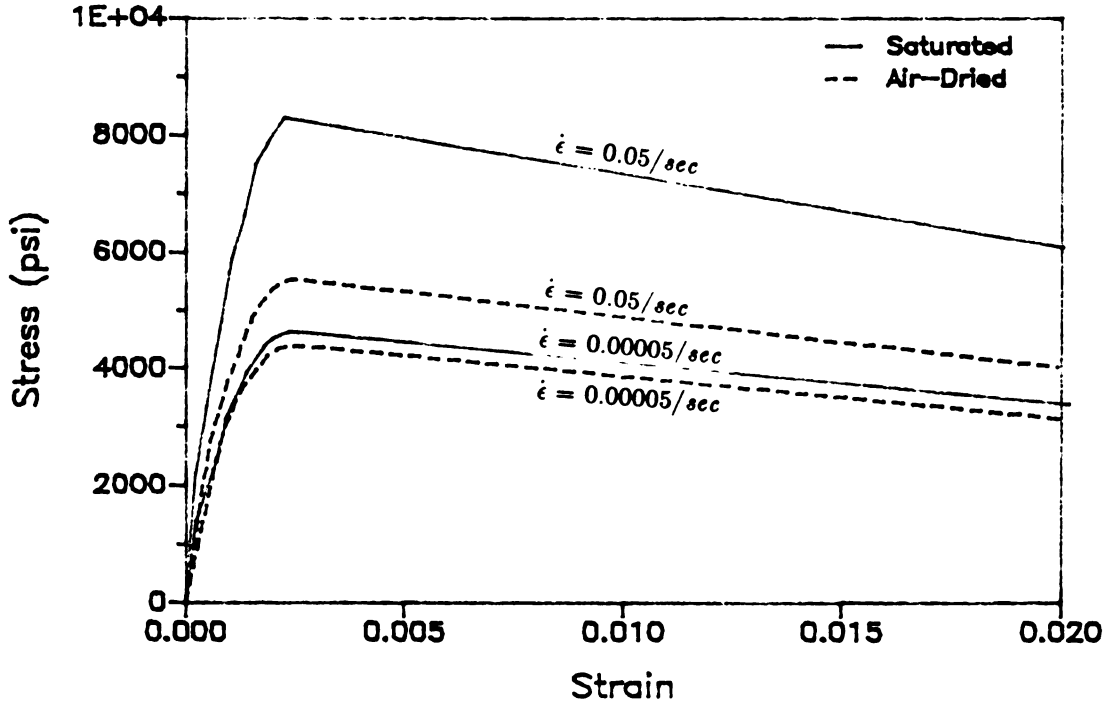

Figure 3.7 Strain Rate Effects on Air-Dried and Saturated Concrete

column studied had an 18 in. square section confined with No. 3 stirrups having a yield strength of 45,000 psi and a volumetric ratio of 0.0182. The cover thickness in these columns was approximated at 0.75 in.

Figure 3.8 compares the static and dynamic constitutive models of the confined air-dried specimen presented in the previous diagram with the static and dynamic constitutive models of an unconfined air-dried specimen with the same compressive strength. This figure shows that confinement considerably reduces the slope of the descending branch in the stress-strain diagram, while a higher strain rate slightly increases this slope. Both confinement and higher strain rates tend to increase the concrete strength.

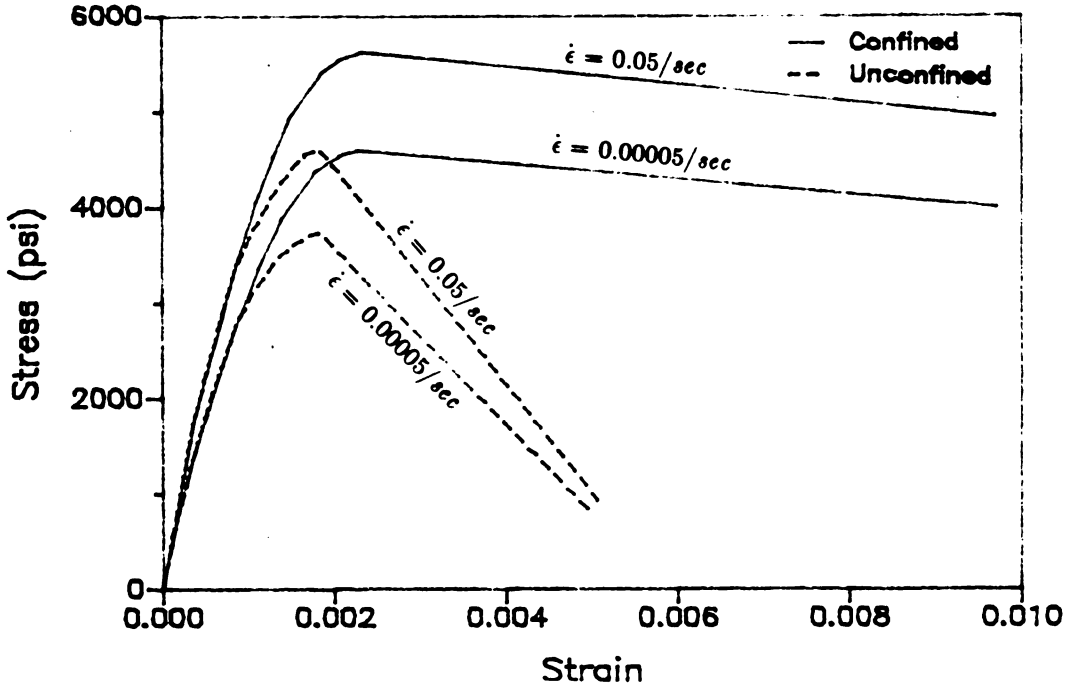

Figure 3.8 Strain Rate Effects on Confined and Unconfined Concrete

3.7 SUMMARY AND CONCLUSIONS

On the basis of many test results reported by different investigators, empirical models were developed for the strain rate effects on the concrete compressive strength, strain at maximum stress, and modulus of elasiticity. It was found that

(1) the concrete compressive strength increases at higher strain rates, and this increase is more significant for saturated concrete,

(2) the strain at maximum stress first decreases and then increases as the strain rate increases over the static values, and

(3) at higher strain rates, the secant modulus of elasticity of concrete increases. The initial tangent modulus also increases at higher strain rates but at a much slower rate when compared with the secant modulus.

The preceding idealizations of the strain rate effects were used to develop a practical constitutive model for confined and unconfined concrete subjected to different compressive strain rates. This model compared well with test results.

The strain rate-dependent constitutive model developed in this chapter for confined and unconfined concrete under compression can be used in refined (e.g., layer) modeling of reinforced concrete sections and elements. Such models can be applied for dynamic analysis of reinforced concrete structures subjected to seismic, impulsive, or wind loads.

CHAPTER 4

A STRAIN RATE-SENSITIVE CONSTITUTIVE MODEL FOR STEEL UNDER TENSION

4.1 INTRODUCTION

The steel yield stress and ultimate strength will increase and the strains corresponding to these stresses, as well as the strain at the beginning of the strain hardenig range, will either increase or remain constant with increasing strain rate. However, the steel modulus of elasticity will not be significantly influenced by the rate of straining[5,12,22,25,26]. Dynamic tests[22,25,26] have revealed that steels with lower yield strengths are relatively more sensitive to strain rate variations than steels with higher strengths. Other factors, such as the chemical properties and the cold work history of the steel, are also suggested[26] to influence the strain rate effects.

In this chapter, the strain rate effects on the mechanical properties of structural steel, deformed reinforcing bars and deformed wires have been compared. Empirical strain rate-dependent constitutive models for steel have been derived on the basis of these comparisons.

4.2 TEST RESULTS

Dynamic test results on structural steel , reinforcing bars and deformed wires have been reported in References 12, 24, 25 and 41. The yield strength in these tests ranged from 26,000 to 99,100 psi, and they included different types of steel with different chemical properties. The tests were all performed in tension, and the specimens were either round or rectangular.

Figure 4.1(a) shows a typical comparison of the static and dynamic stress-strain diagrams. As shown in this figure, the steel modulus of elasticity is not influenced by the strain rate variations, but all the load-sustaining properties and the percentage elongations increase with increasing strain rate.

Figure 4.1(b) shows the ratios of dynamic to static (lower) yield strengths versus the rate of straining in test results reported by different investigators. This figure shows that, in spite of the wide scatter in the test results, the steel yield strength increases with increasing strain rate. The same conclusion is valid for test results on the steel upper yield strength, as shown in Figure 4.1(c). The steel upper yield strength seems to be more strain rate-sensitive than the lower yield strength. The ultimate strength of steel, as shown in Figure 4.1(d), shows an increase with increasing rate of straining, but at a slower rate when compared with the increase in yield strength.

Figure 4.1(e) presents the ratio of the measured dynamic to static strain at the initiation of the steel strain hardening region versus the rate of straining in dynamic tests. A rapid increase in this strain is observed with increasing strain rate. The ultimate strain is shown in Figure 4.1(f) to increase rather slowly with the rate of straining. Note that the scatter in test results is rather large.

4.3 FACTORS INFLUENCING THE STRAIN RATE EFFECTS

In order to find the sources of the considerable scatter in the observed strain

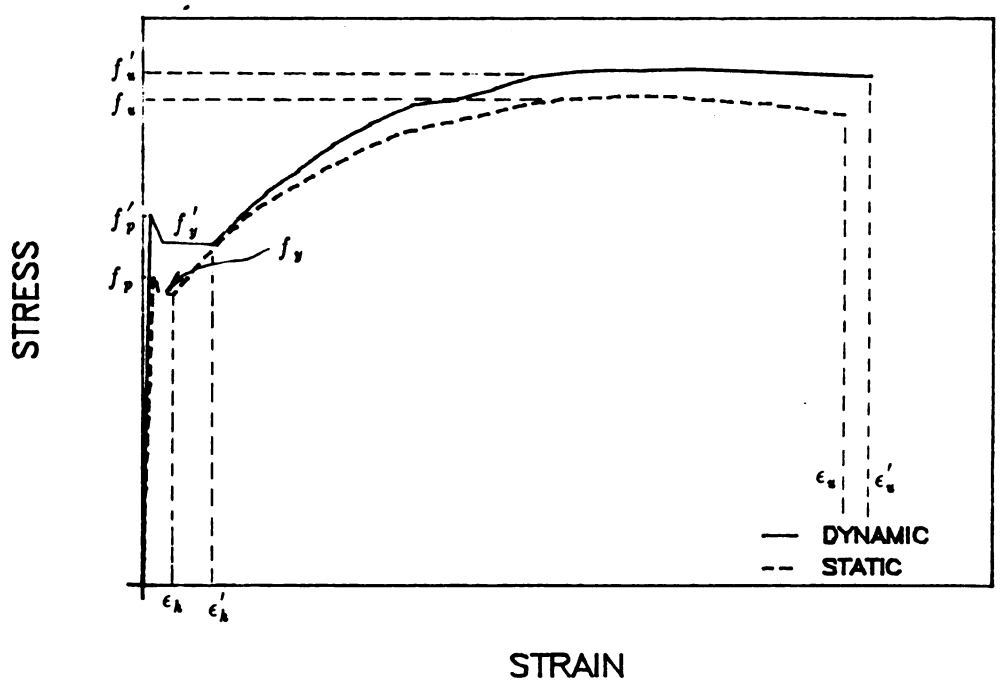

(a) Static and Dynamic Constitutive Diagrams

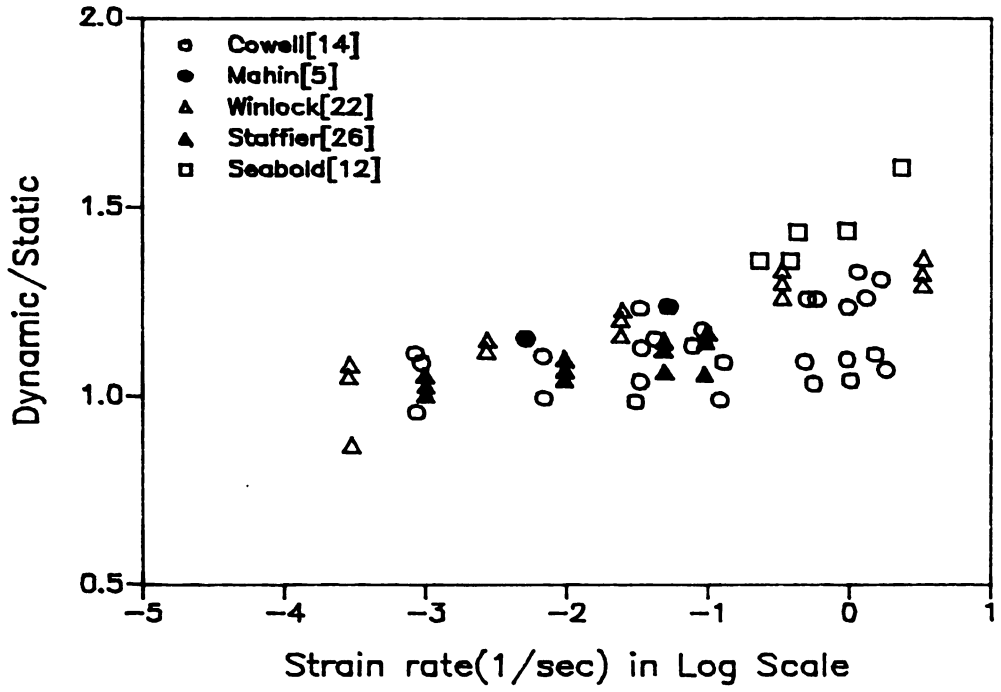

(b) Lower Yield Strength

Figure 4.1 Strain Rate Effects on The Steel Mechnical Properties

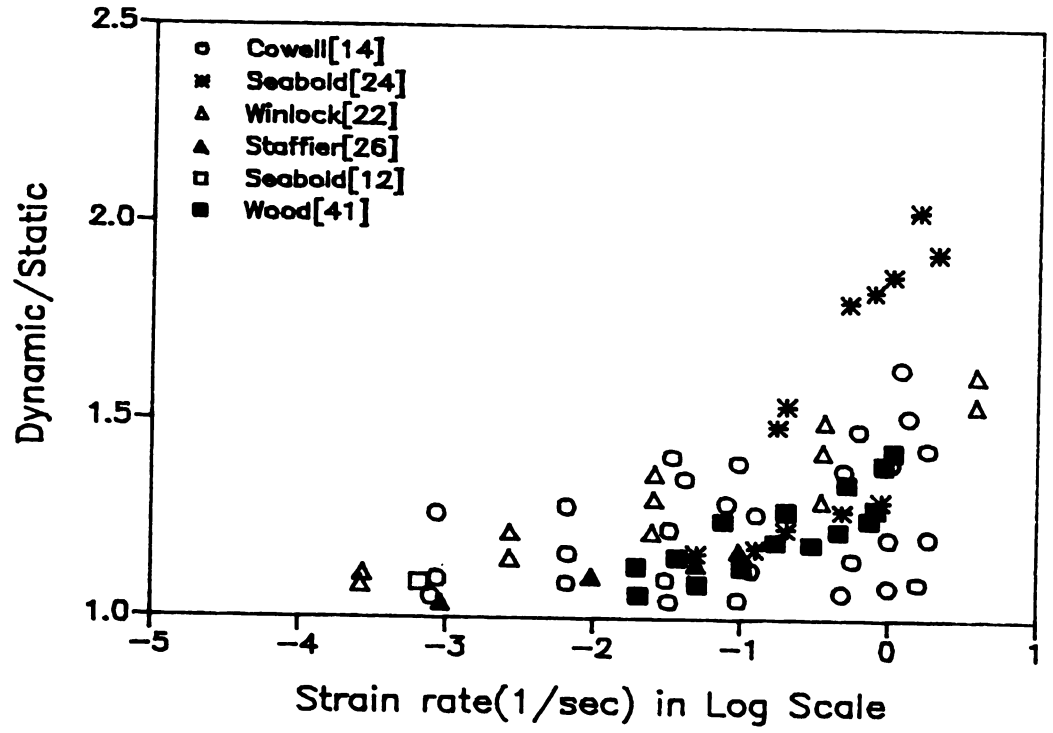

(c) Upper Yield Strength

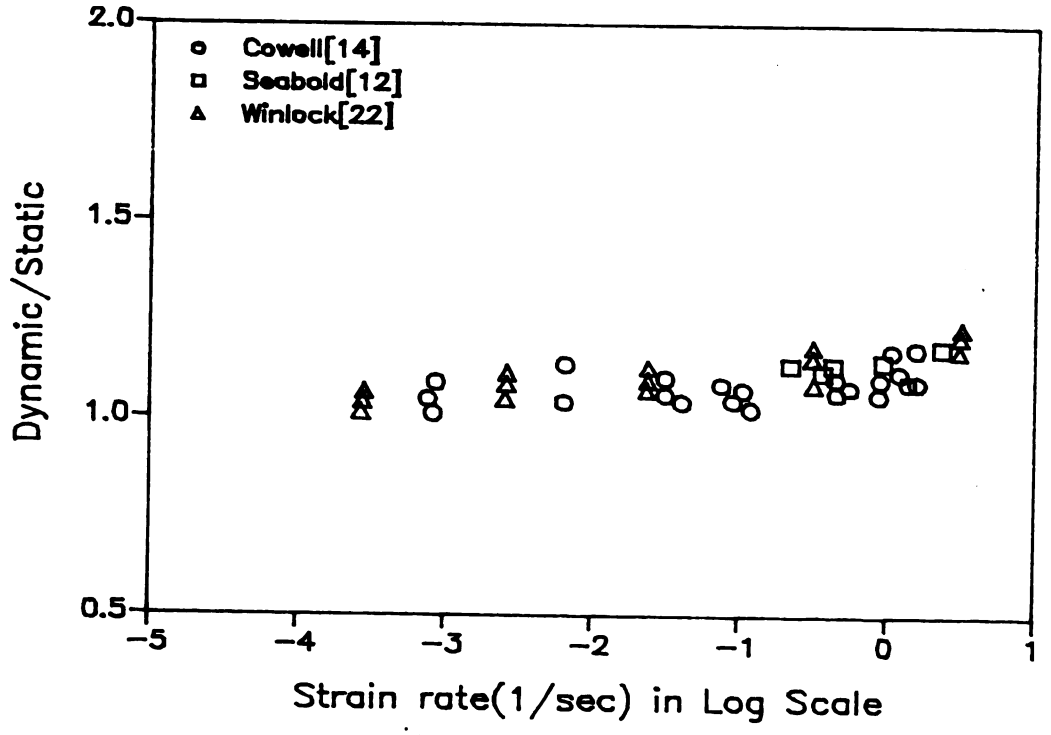

(d) Ultimate Strength

Figure 4.1 Strain Rate Effects on The Steel Mechnical Properties(cont'd)

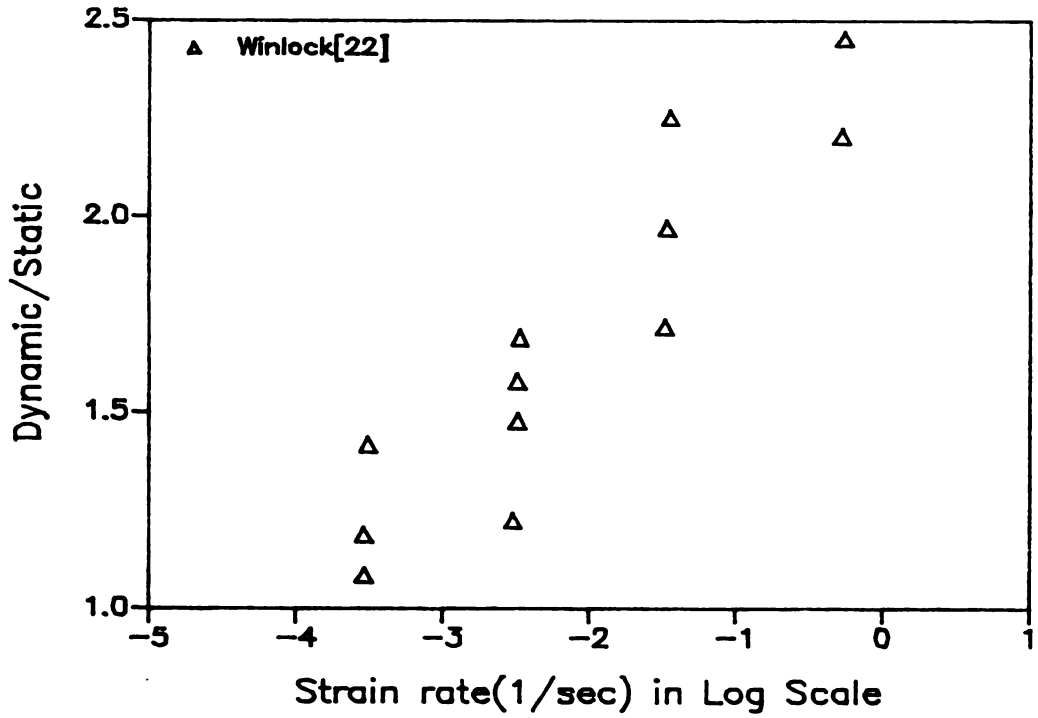

(e) Strain at The Initiation of Strain Hardening

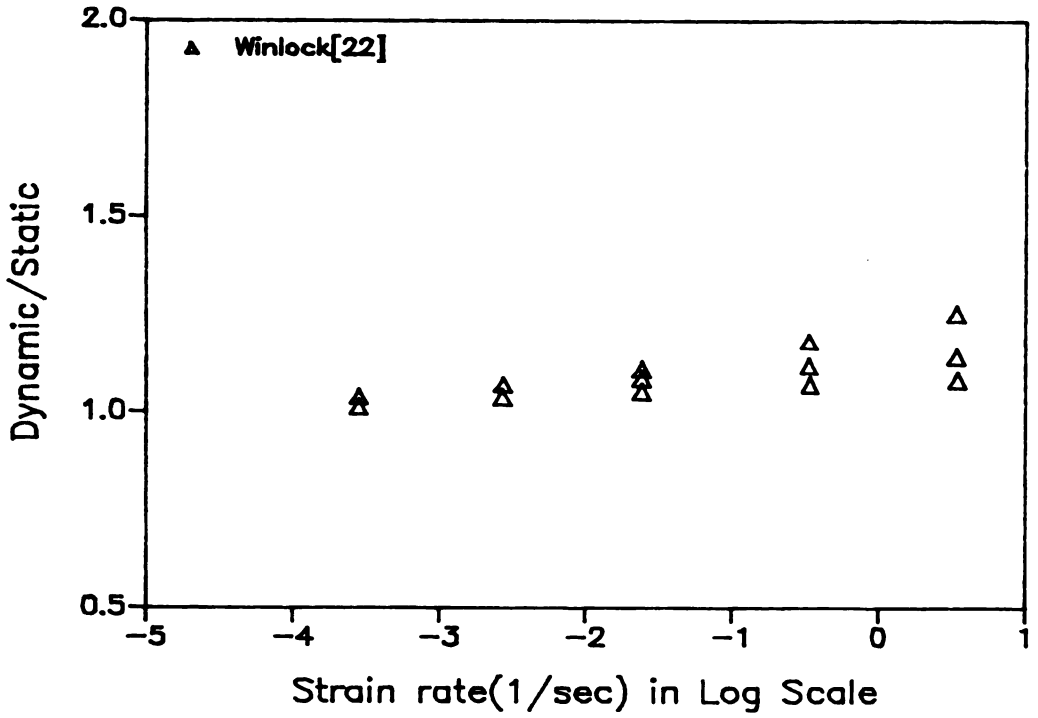

(f) Ultimate Strain

Figure 4.1 Strain Rate Effects on The Steel Mechnical Properties(cont'd)

rate effects (Figure 4.1), the influences of the steel yield strength, the steel type (structural, bar, wire), and the specimen shape (round, rectangular) were studied. It was found that the main source of scatter is the steel yield strength, and the other factors do not noticeably influence the strain rate effects. For example, the scatter in strain rate effects on the (lower) yield strength shown in Figure 4.1(b) is considerably reduced when the test results are presented separately for different ranges of yield strength in Figure 4.2. It is clear in this figure that the strain rate effect becomes less significant as the yield strength increases. Similar influences of yield strength are observed in Figures 4.3, 4.4, 4.5 and 4.6 for the strain rate effects on the upper yield strength, ultimate strength, strain at the beginning of the strain hardening region, and the ultimate strain of steel, respectively.

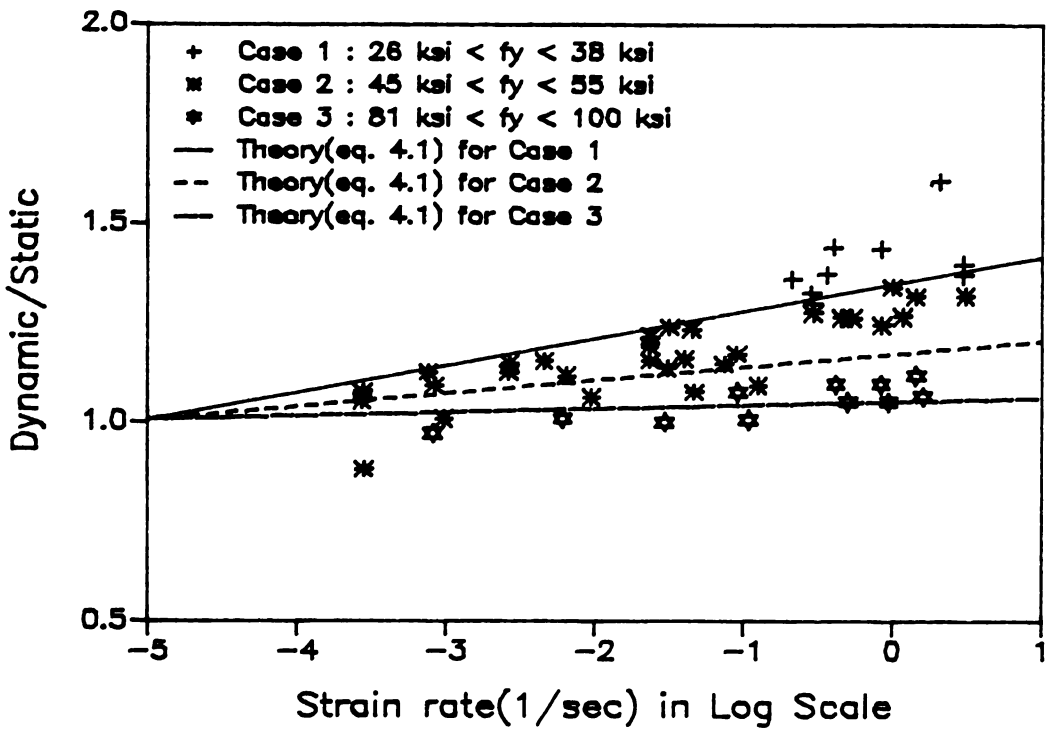

Figure 4.2 Strain Rate Effects on The Lower Yield Strength of Steels with Different Yield Strengths

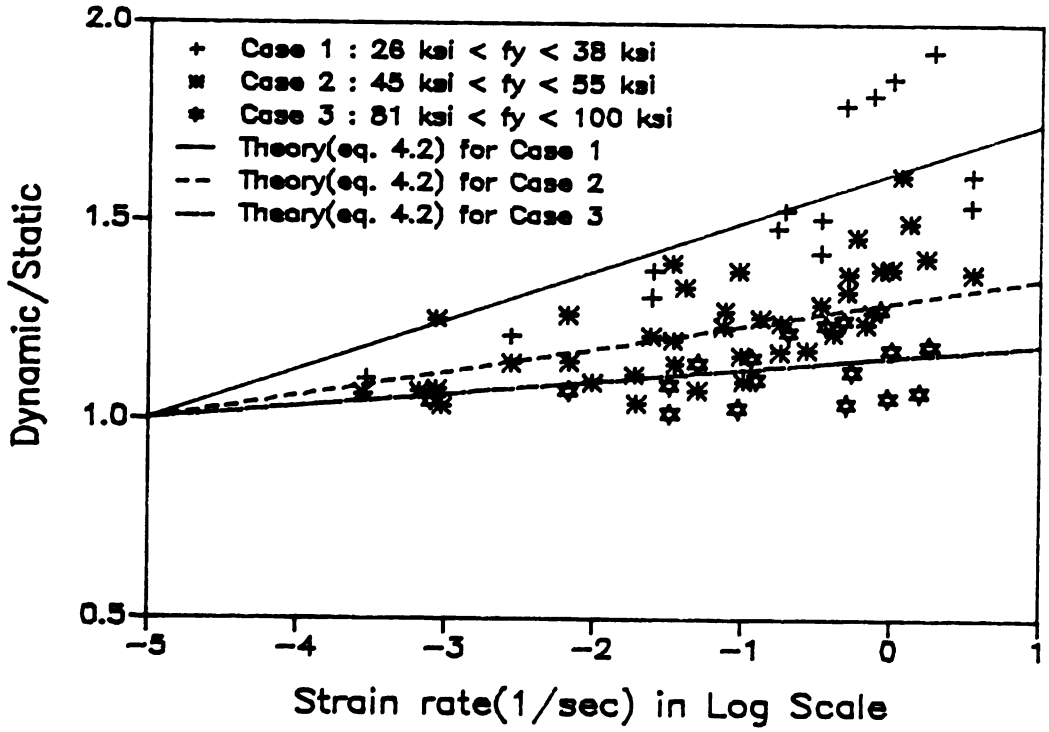

Figure 4.3 Srain Rate Effects on The Upper Yield Strength of Steels with Different Yield Strengths

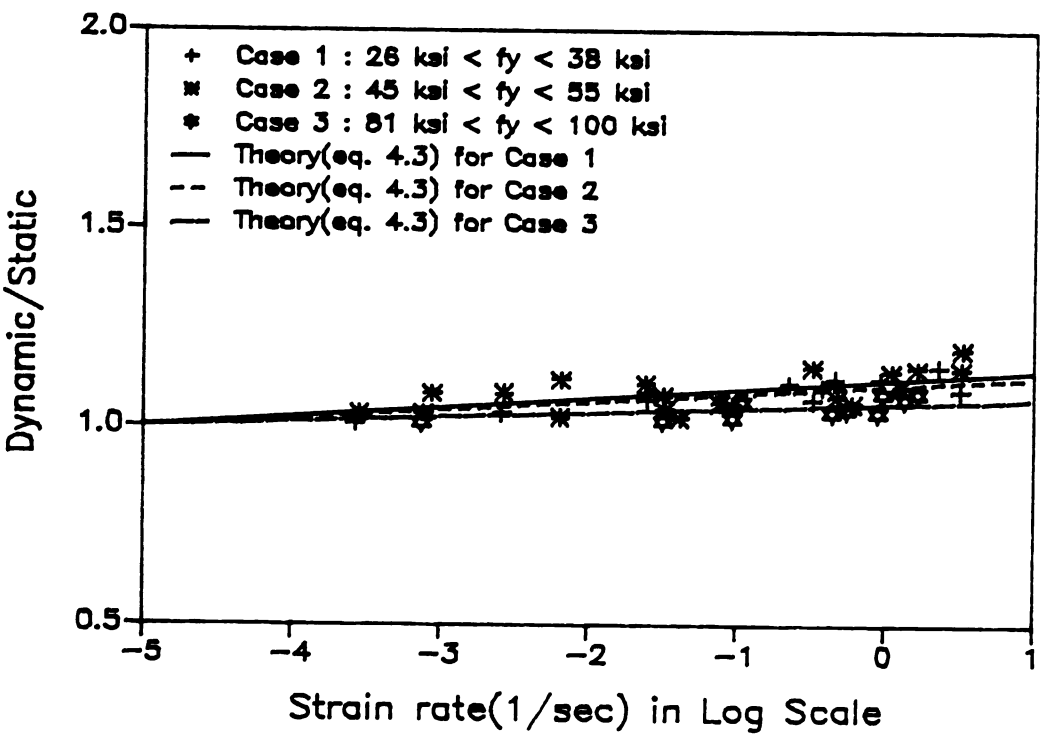

Figure 4.4 Strain Rate Effects on The Ultimate Strength of Steels with Different Yield Strengths

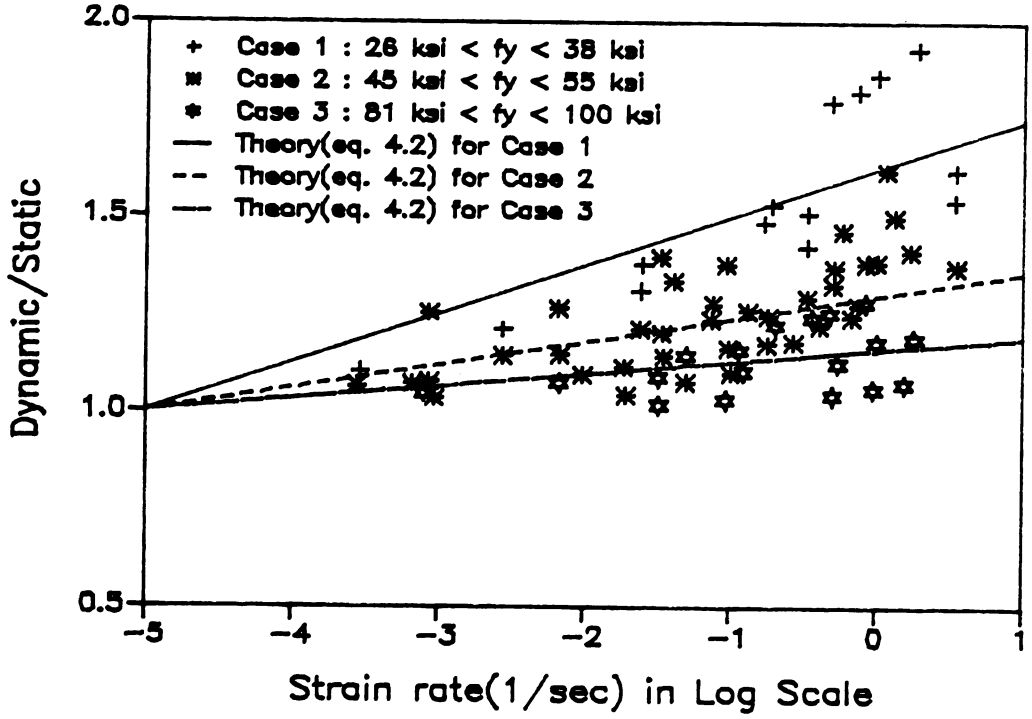

Figure 4.3 Srain Rate Effects on The Upper Yield Strength of Steels with Different Yield Strengths

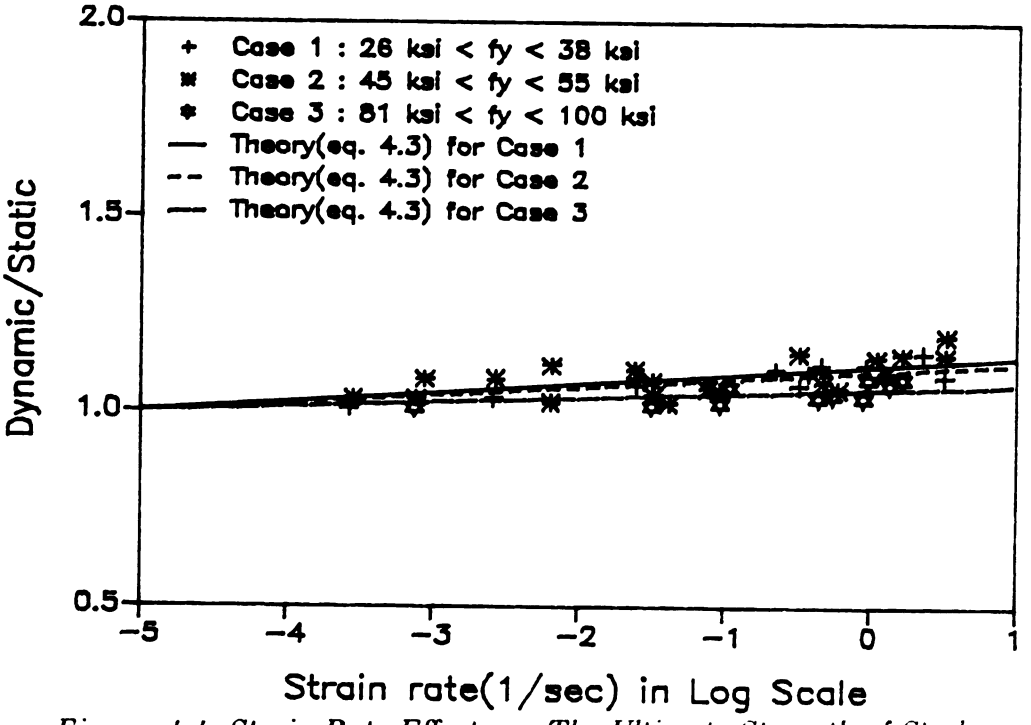

Figure 4.4 Strain Rate Effects on The Ultimate Strength of Steels with Different Yield Strengths

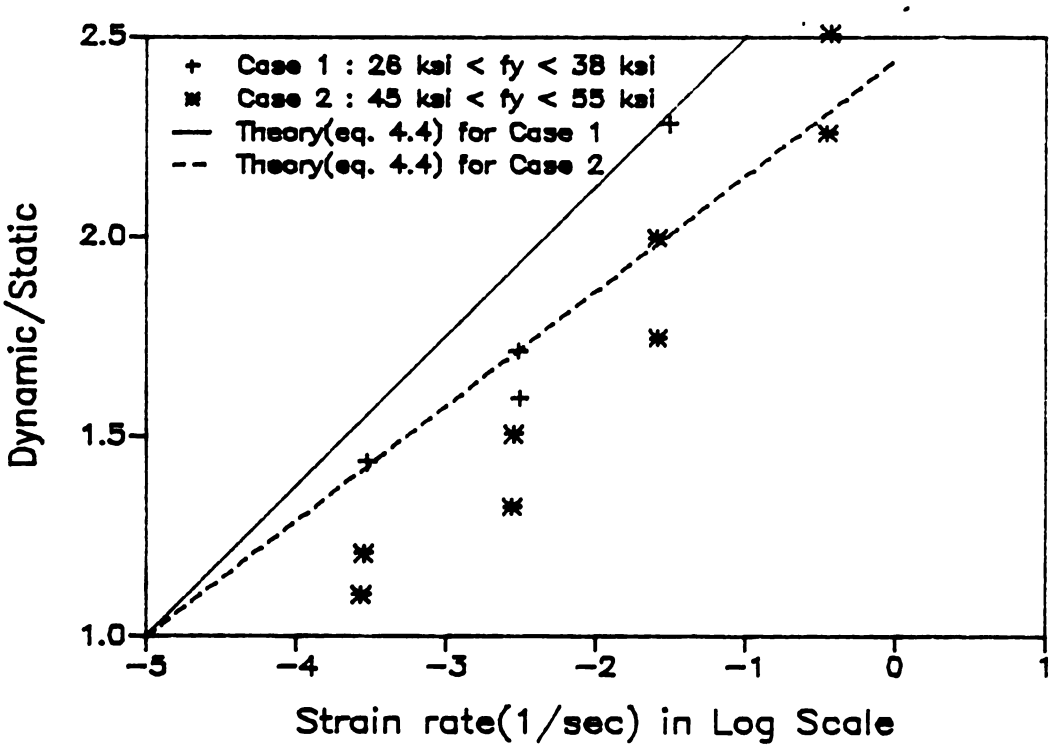

Figure 4.5 Strain Rate Effects on Strain at The Initiation of Strain Hardening of Steels with Different Yield Strengths

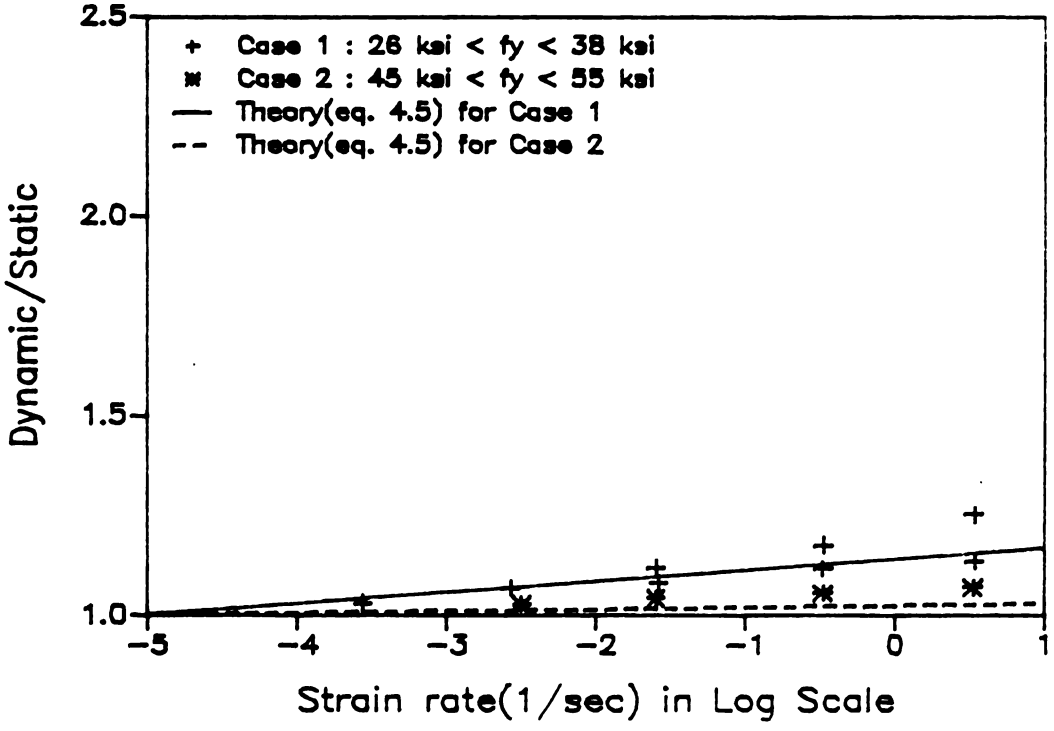

Figure 4.6 Strain Rate Effects on The Ultimate Strain of Steels with Different Yield Strengths

4.4 THE CONSTITUTIVE MODEL FOR STEEL

Considering the influence of yield strength on the strain rate-sensitivity of the steel mechanical properties, the following expressions were derived in terms of yield strength for the dynamic to static ratios of the lower and upper yield and ultimate strengths of steel and its strain hardening initiation and ultimate strains:

$$\frac{f_y'}{f_y} = (-4.51\times10^{-7}\, f_y + 1.46) + (-9.20\times10^{-7}\, f_y + 0.0927)\log_{10}\dot{\epsilon} \quad (4.1)$$

$$\frac{f_p'}{f_p} = (-6.83\times10^{-6}\, f_y + 1.72) + (-1.37\times10^{-6}\, f_y + 0.144)\log_{10}\dot{\epsilon} \quad (4.2)$$

$$\frac{f_u'}{f_u} = (-7.71\times10^{-7}\, f_y + 1.15) + (-2.44\times10^{-7}\, f_y + 0.04969)\log_{10}\dot{\epsilon} \quad (4.3)$$

$$\frac{\epsilon_h'}{\epsilon_h} = (-4.21\times10^{-5}\, f_y + 4.46) + (-8.41\times10^{-6}\, f_y + 0.693)\log_{10}\dot{\epsilon} \quad (4.4)$$

$$\frac{\epsilon_u'}{\epsilon_u} = (-8.93\times10^{-6}\, f_y + 1.40) + (-1.79\times10^{-6} f_y + 0.0827)\log_{10}\dot{\epsilon} \quad (4.5)$$

where,

f_y, f_y' = static and dynamic lower yield strengths of steel, respectively (psi) ;
f_p, f_p' = static and dynamic upper yield strengths of steel, respectively;
f_u, f_u' = static and dynamic ultimate strengths of steel, respectively;
ϵ_h, ϵ_h' = static and dynamic strain hardening initiation strains of steel, respectively; and
ϵ_u, ϵ_u' = static and dynamic ultimate strains of steel, respectively.

These expressions are shown to compare well with test results in Figures 4.2 to 4.6. In each figure, the value of f_y used in the corresponding expression is the average of the maximum and minimum yield strengths of the test results used in compression.

The above expressions together with the static values of the (lower) yield and ultimate strengths, and strain hardening initiation and ultimate strains can be used in the following expressions for constructing the steel monotonic stress-strain

diagram under the action of dynamic loads. It should be mentioned that since the upper yield stress is a local phenomenon, it is generally excluded from the steel constitutive models[8,26].

$$f_s = \begin{cases} E_s \cdot \epsilon_s & \text{for } \epsilon_s < f_y'/E_s \\ f_y' & \text{for } \dfrac{f_y'}{E_s} \leq \epsilon_s < \epsilon_h' \\ f_y' \left[\dfrac{112(\epsilon_s - \epsilon_h') + 2}{60(\epsilon_s - \epsilon_h') + 2} + \dfrac{\epsilon_s - \epsilon_h'}{\epsilon_u' - \epsilon_h'} \left(\dfrac{f_u'}{f_y'} - 1.7 \right) \right] & \\ \quad \text{for } \epsilon_h' \leq \epsilon_s < \epsilon_u' & \end{cases} \tag{4.6}$$

where,

f_s = steel stress (psi);
ϵ_s = steel strain; and
E_s = steel elastic modulus (psi)

The above constitutive model requires practically all the quasi-static characteristic stress and strain values of steel (f_y, f_u, ϵ_h, and ϵ_u) which might not be readily available. For this reasons, a simpler bilinear dynamic constitutive model was developed for steel subjected to monotonic loading. Selection of the bilinear form was mainly due to its popularity in static constitutive modeling of steel. The values required for constructing this model are the static yield stress and ultimate strain, and the static strain hardening modulus of steel (E_h), defined as the average slope of the static stress-strain diagram in the strain hardening region, which is about 100,000 psi:

$$f_s = \begin{cases} E_s \epsilon_s & \text{for } \epsilon_s < f_y'/E_s \\ f_y' + E_h' \left(\epsilon_s - \dfrac{f_y'}{E_s} \right) & \text{for } \dfrac{f_y'}{E_s} < \epsilon_s < \epsilon_u' \end{cases} \tag{4.7}$$

where,

$$E_h' = E_h \left[2\times10^{-5} + 0.0770 + (4\times10^{-6}\, f_y - 0.185) \log_{10}\dot{\epsilon}\right] \quad ;$$

f_y = static steel yield strength (psi).

The above formulation for the dynamic strain hardening modulus was derived by curve fitting to the experimentally obtained slopes of the line connecting the yield and ultimate points on the stress-strain diagrams of steel.

Figures 4.7(a) and (b) compare the constitutive models derived using Equations (4.6) and (4.7) with the experimental monotonic stress- strain diagrams presented in Reference 22 at two different strain rates for steel specimens with yield strengths of 34,000 and 44,500 psi, respectively. As shown in these figures, both models compare satisfactorily with test results. The best comparison is obtained with Equation (4.6) which requires more experimental data on steel static properties. Equation (4.7), which is in the simple and popular bilinear form, also seems to be capable of predicting test results with relatively small errors.

4.5 SUMMARY AND CONCLUSIONS

Dynamic test results reported by different investigators on structural steel, deformed bars, and deformed wires subjected to monotonic tension were used for deriving empirical expressions for the ratios of static to dynamic values of the yield and ultimate strengths, yield and ultimate strains, and the strain at the end of the yield plateau. The principal variables in the expressions are the rate of straining and the steel static yield strength. These expressions were then used for developing dynamic constitutive models for monotonically loaded steel.

The following conclusions can be drawn from this chapter:

(1) All the characteristic stress and strain values on the steel monotonic constitutive diagram increase with increasing strain rate. The yield

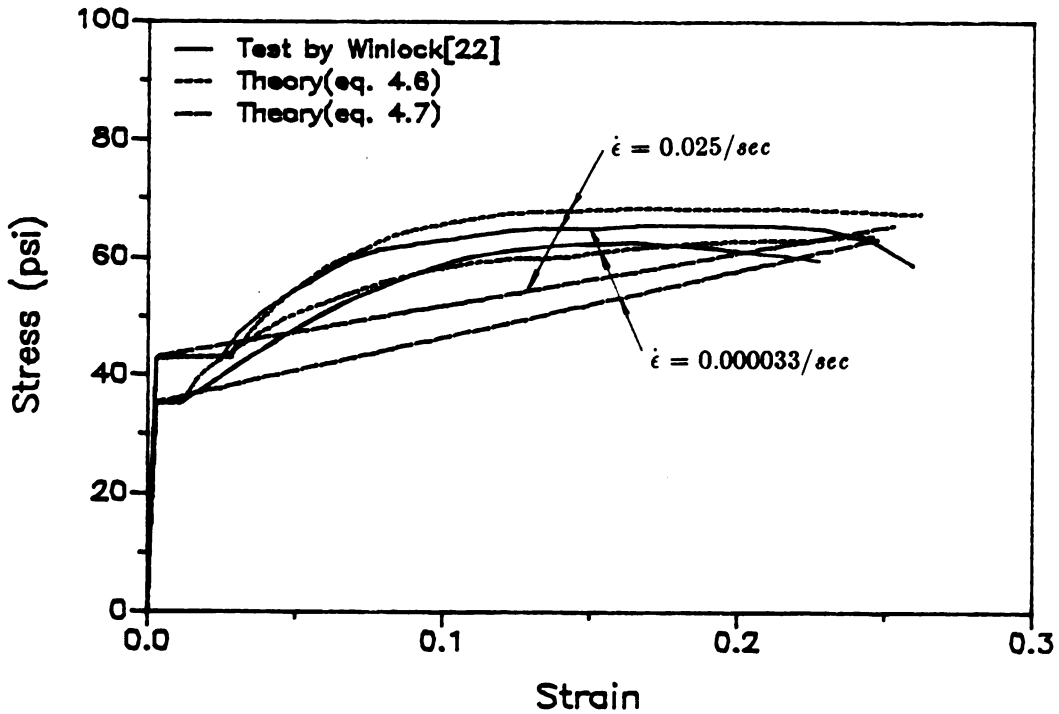

(a) f_y = 34,000 psi

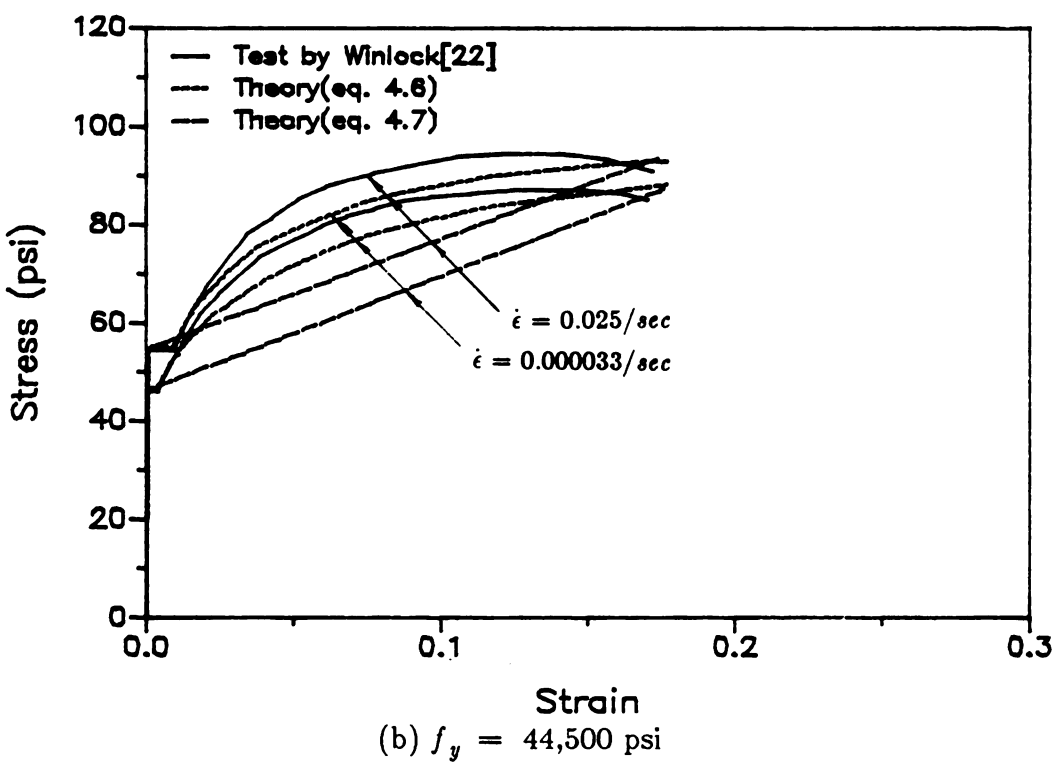

(b) f_y = 44,500 psi

Figure 4.7 Comparison of The Proposed Monotonic Constitutive Models of Steel with Test Results

strength is more strain rate-sensitive than the ultimate strength. The steel modulus of elasticity is independent of the rate of straining.

(2) The main factor influencing the strain rate effects is the static yield strength of steel. The mechanical properties of steel with lower yield strength are more strain rate-sensitive.

(3) No considerable difference was observed between the strain rate effects on structural steel, deformed bars, and deformed wires.

(4) The empirical strain rate-dependent constitutive models proposed in this chapter for steel subjected to monotonic loading compare well with test results.

(5) The proposed dynamic constitutive models of steel can be used for developing strain rate-sensitive analytical models of reinforced concrete and steel elements under the action of dynamic loads. These models can be used in dynamic analysis of structures subjected to seismic and explosive loadings.

CHAPTER 5

A STRAIN RATE-SENSITIVE MODEL FOR AXIAL/FLEXURAL ANALYSIS OF REINFORCED CONCRETE ELEMENTS UNDER DYNAMIC LOADS

5.1 INTRODUCTION

As a result of the increases in material strength and stiffness, the axial-flexural and shear strengths and stiffnesses of reinforced concrete (R/C) elements also increase at higher rates of loading (Figure 5.1). Hence, reliable information on strength and stiffness of R/C elements at higher strain rates is needed to improve the techniques currently used in dynamic analysis and design of R/C structures.

The increased strength and stiffness of R/C elements at higher loading rates might adversely influence the structural response to dynamic loads. This phenomenon can result in higher element forces induced by the application of impulsive loads on R/C structures. It might also encourage the tendency towards the brittle modes of failure, for example in shear or by pull-out of anchorage bars in joints, under dynamic loads[12].

In this chapter, a refined strain rate-sensitive analytical model for R/C elements is developed, and it is used for studying the loading rate effects on the dynamic response of R/C beams and columns. Practical axial and flexural design

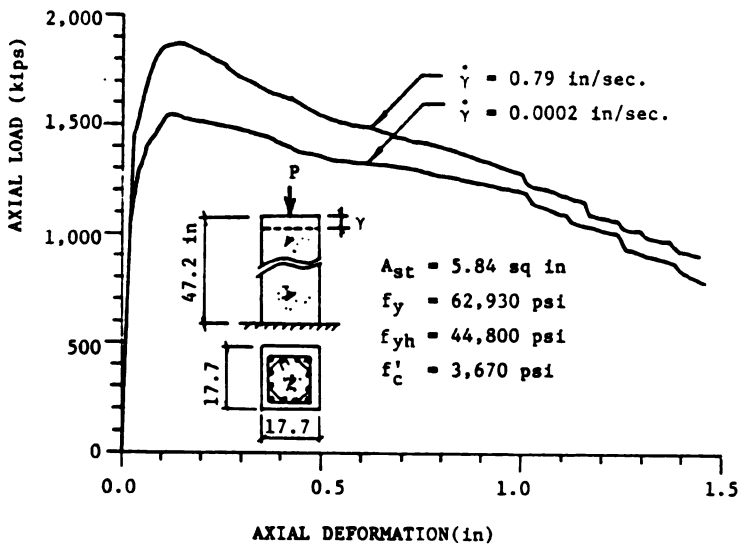

(a) Axial Behavior

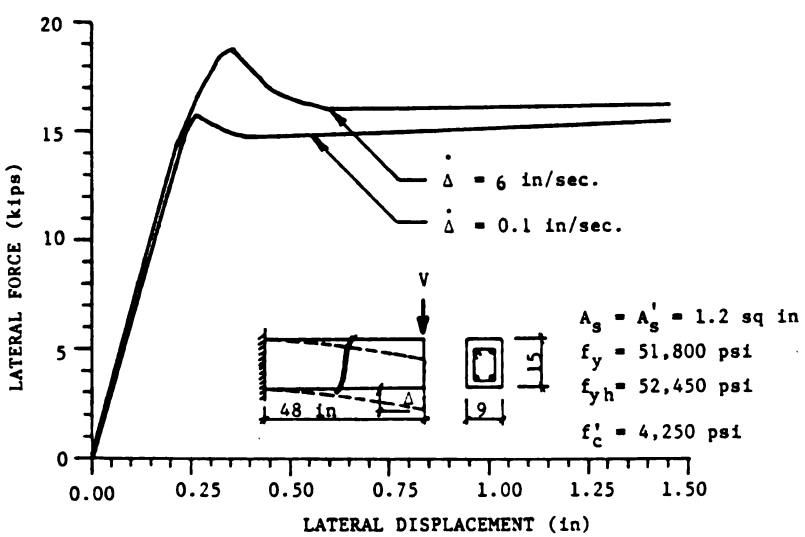

(b) Flexural Behavior

Figure 5.1 Loading Rate Effects on The Axial and Flexural Behavior of R/C Elements

techniques are also presented.

5.2 SECTION MODEL

The axial/flexural tangent stiffness matrix of R/C cross section was derived using the layer modeling technique[42]. In this technique, the cross section is divided into a number of concrete and steel layers (see Figure 5.2). The strain increments and strain rates at these layers are calculated from the values of axial strain increment and strain rate of the section plastic centroid, and the curvature increment and curvature rate of the section (assuming that plain section remains plain):

$$d\epsilon_i = d\epsilon_p + d\phi \cdot y_i \tag{5.1}$$

$$\dot{\epsilon}_i = \dot{\epsilon}_p + \dot{\phi} \cdot y_i \tag{5.2}$$

where,

$d\epsilon_i$ = strain increment in the i'th layer;
$\dot{\epsilon}_i$ = strain rate in the i'th layer;
$d\epsilon_p$ = strain increment at plastic centroid;
$\dot{\epsilon}_p$ = strain rate at plastic centroid;
$d\phi$ = section curvature increment;
$\dot{\phi}$ = section curvature rate;
y_i = distance from the centroid of the i'th layer to the plastic centroid

Once the layer strains and strain rates are obtained, tangent stiffness moduli (E_i) of various layers can be calculated using the strain rate-dependent concrete and steel constitutive models presented in chapters 2 and 3, respectively:

$$E_i = \frac{df(\epsilon_i, \dot{\epsilon}_i)}{d\epsilon_i} \tag{5.3}$$

where,

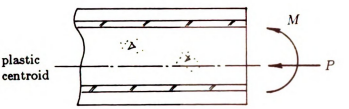

(a) Applied Forces

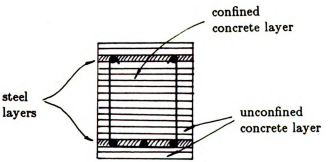

(b) Cross Section Subdivision

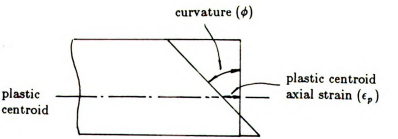

(c) Strain Distribution

Figure 5.2 Layer Model for R/C Sections

$f(\epsilon_i, \dot{\epsilon}_i)$ = constitutive equation expressing the value of stress at the i'th layer in terms of strain and strain rate.

The section stiffness matrix (K_s) can then be constructed by proper summation of the layer tangent stiffness moduli:

$$\begin{Bmatrix} dM \\ dP \end{Bmatrix} = K_s \begin{Bmatrix} d\phi \\ d\epsilon_p \end{Bmatrix} = \begin{bmatrix} K_{11} & K_{12} \\ K_{21} & K_{22} \end{bmatrix} \begin{Bmatrix} d\phi \\ d\epsilon_p \end{Bmatrix} \tag{5.4}$$

where,

dM = bending moment increment at the cross section;

dP = axial load increment at the cross section;

$K_{11} = \sum_{i=1}^{n} A_i E_i y_i^2$;

$K_{12} = K_{21} = \sum_{i=1}^{n} A_i E_i y_i$;

$K_{22} = \sum_{i=1}^{n} A_i E_i$;

A_i = area of the i'th layer.

5.3 FACTORS INFLUENCING THE AXIAL/FLEXURAL BEHAVIOR OF R/C SECTIONS

The reliability of the layer modeling technique introduced in the previous section has been confirmed through comparisons of its predictions with test results. The typical comparisons are shown in Figure 5.3[43].

The analysis procedure described in section 5.2 was used to study the effects of variations in section properties on its response to axial/flexural forces. The typical beam and column cross sections shown in Figures 5.4(a) and (b), respectively, were chosen as the "standard" sections in this study, and the influence of variations in concrete and steel strengths, steel ratio, confinement and the rate of loading on the axial/flexural response characteristics of these sections were investi-

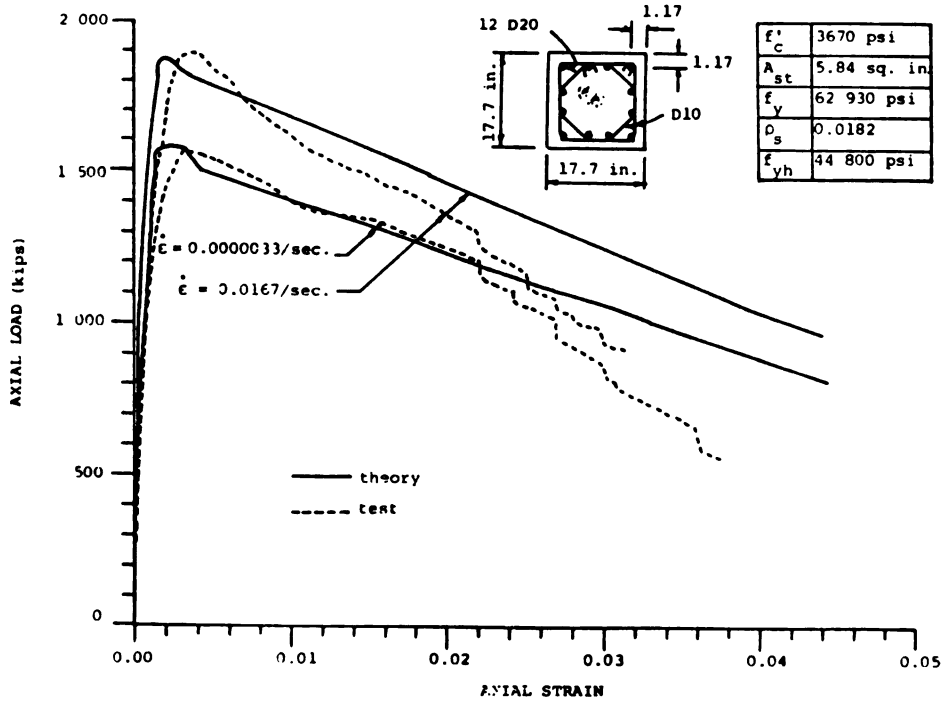

(a) Axial Behavior of Column

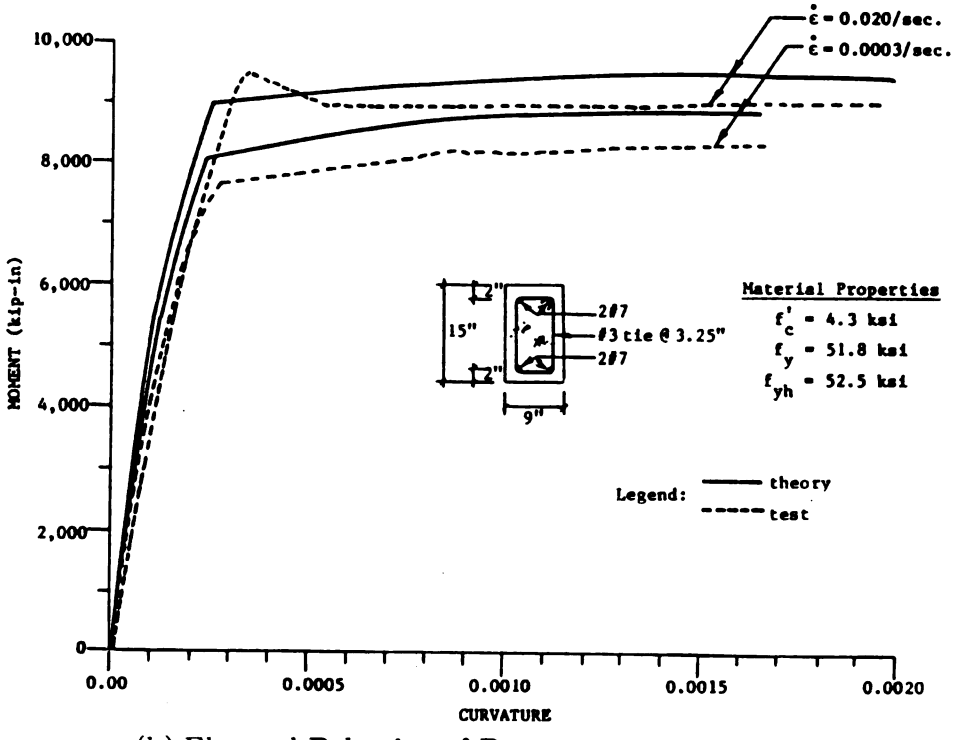

(b) Flexural Behavior of Beam

Figure 5.3 Typical Comparison of The Predictions with Test Results

Material Properties

f_y = 60 ksi
f_{yh} = 50 ksi
f'_c = 4 ksi

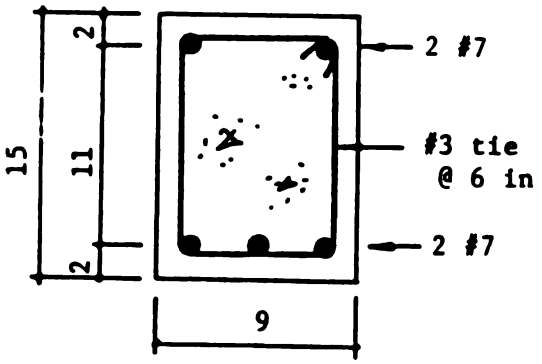

(a) Beam

Material Properties

f_y = 60 ksi
f_{yh} = 50 ksi
f'_c = 4 ksi

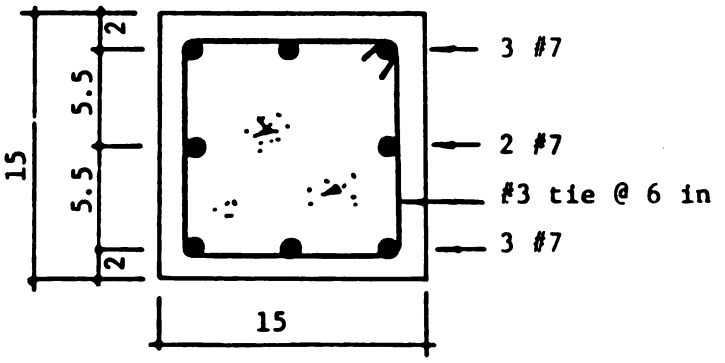

(b) Column

Figure 5.4 Standard Beam and Column Cross Section

gated.

5.3.1 Effect of the Longitudinal Steel Yield Strength

Figures 5.5(a), (b) and (c) present the quasi-static ($\dot{\epsilon} \leq 10^{-6}$/sec) moment-curvature and axial load-axial strain relationships and the interaction diagrams, respectively, for sections similar to the standard ones, except for their longitudinal steel yield strengths. It may be concluded from Figure 5.5(a) that the beam flexural strength is strongly sensitive to the variations in longitudinal steel yield strength ($\pm$ 30% change in yield strength causes about $\pm$ 30% in the flexural strength of the standard section). The effect of longitudinal steel yield strength on the column compressive strength is shown in Figure 5.5(b) to be important, though not as much as the corresponding effect on the beam flexural strength. Changing the longitudinal steel yield strength by $\pm$ 30% changes the standard column compressive strength by roughly $\pm$ 10%. Neither the axial nor the flexural initial stiffnesses of the standard beam and column cross sections were sensitive to the variations in the longitudinal steel yield strength. Figure 5.5(c), which presents the column interaction diagrams obtained at a maximum concrete strain of 0.003, confirms that the sensitivity of section strength to the changes in longitudinal steel yield strength increases as the flexural action becomes dominant.

5.3.2 Effect of the Concrete Compressive Strength

Figure 5.6 shows the quasi-static axial/flexural response characteristics of R/C beam and column cross sections similar to the standard ones, but with different concrete compressive strengths. It can be seen in Figure 5.6(a) that the changes in concrete compressive strength have relatively small effects on the beam flexural stiffness and strength. There are, however, major effects on the column compressive stiffness and strength resulting from the variations in concrete strength as shown in Figure 5.6(b). Changing the compressive strength by $\pm$ 30%

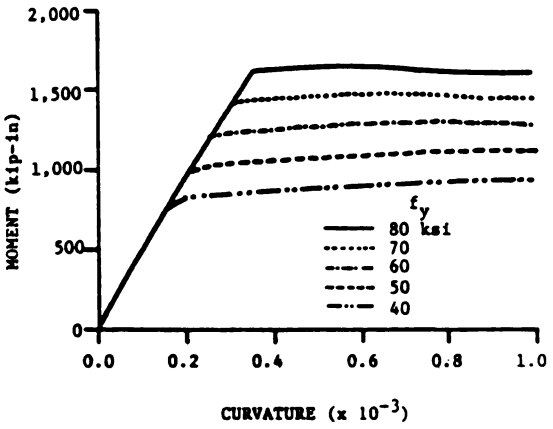

(a) $M - \phi$ curves

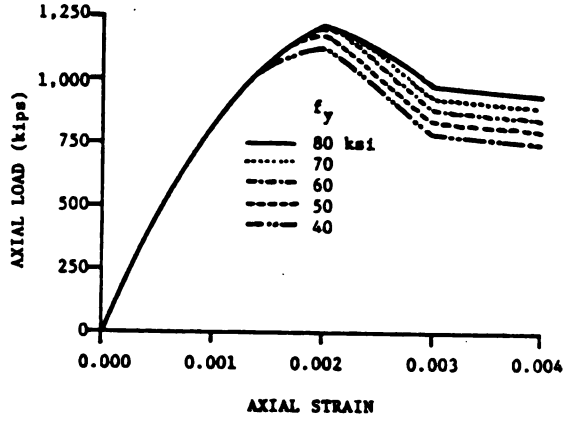

(b) $P - \epsilon_p$ curves

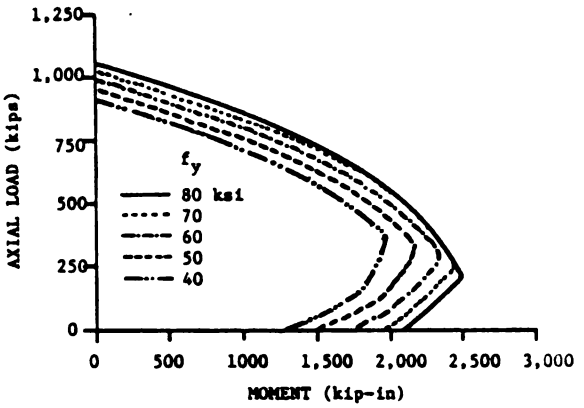

(c) Interaction Curves

Figure 5.5 Effect of Longitudinal Steel Yield Strength

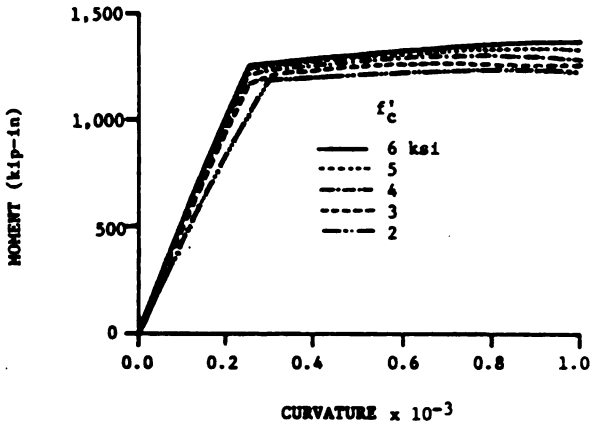

(a) $M - \phi$ curves

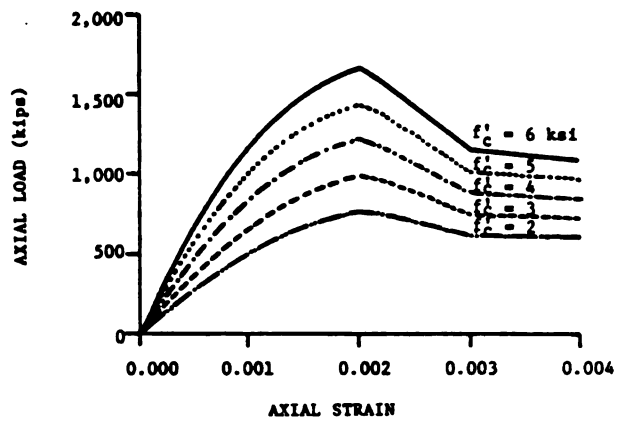

(b) $P - \epsilon_p$ curves

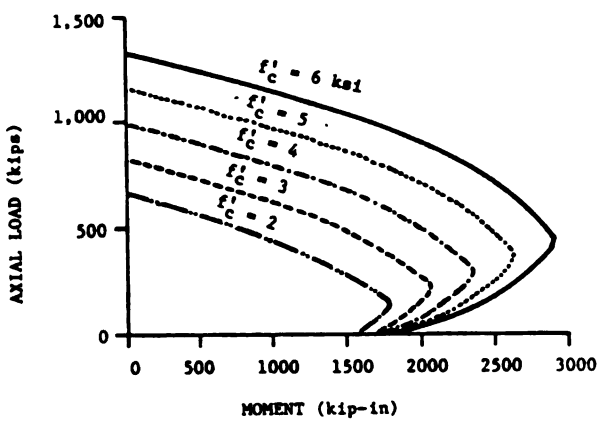

(c) Interaction Curves

Figure 5.6 Effect of Concrete Compressive Strength

results in about ± 3% and ± 25% variations, respectively, in the flexural and compressive strengths (and stiffnesses).

5.3.3 Effect of the Longitudinal Steel Ratio

As shown in Figure 5.7(a), the changes in tension steel ratio have major effects on the beam quasi-static flexural behavior (± 30% changes in the ratio of tension steel changes the flexural stiffness and strength of the standard beam section by about ± 30%). The quasi-static flexural response is not, however, much sensitive to the changes in the ratio of compression steel, as shown in Figure 5.7(b). The reduction in compression steel, however, tends to reduce the ductility of the beam flexural behavior (that is the flexural resistance at larger deformations). Figures 5.7(c) and (d) show the axial load-axial strain relationships and interaction diagrams of sections similar to the standard column, except for their total steel areas. It is observed that the column axial strength and, to some extent, its axial stiffness are influenced by the changes in the total area of the longitudinal steel. The column compressive strength changes by about ± 15% as the total longitudinal steel ratio changes by ± 30%. Figure 5.7(d) indicates that the column compressive strength tends to be more sensitive to the variations in the total steel area as the flexural forces increase.

5.3.4 Effect of Confinement

Better confinement of concrete can be achieved by increasing the transverse steel ratio (e.g. by reducing the spacing of lateral steel), and to some extent by raising the yield strength of transverse steel. Improved confinement increases the compressive ductility and to a lesser extent the compressive strength of concrete. Figure 5.8(a) shows that the changes in concrete confinement produced by reducing the spacing of transverse steel does not influence the beam quasi-static flexural behavior, noticing that the analytical model used in this study does not account

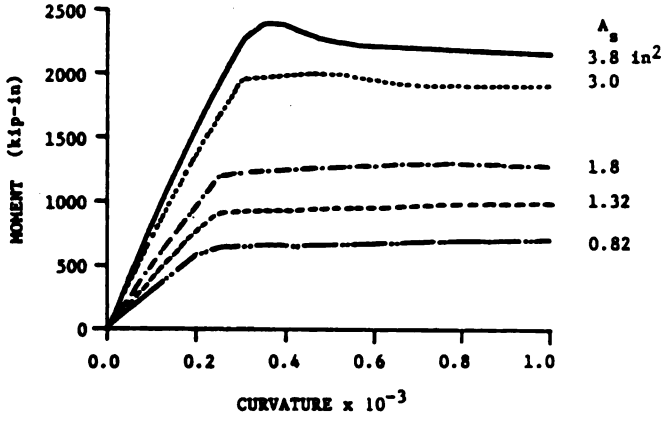

(a) $M - \phi$ curves

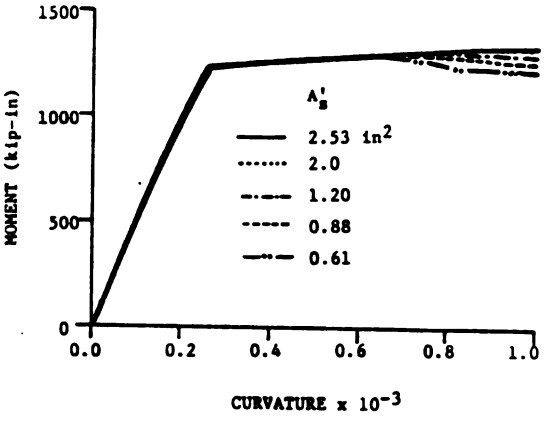

(b) $M - \phi$ curves

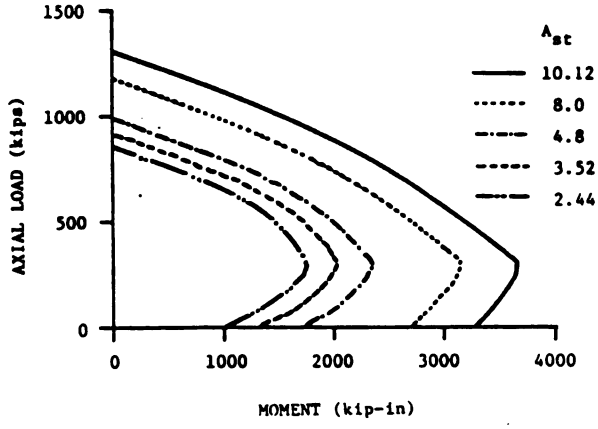

(c) $P - \epsilon_p$ curves

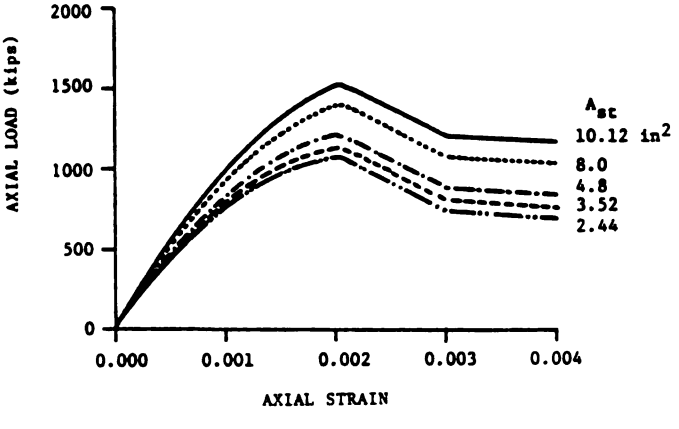

(d) Interaction Curves

Figure 5.7 Effect of Longitudinal Steel Area

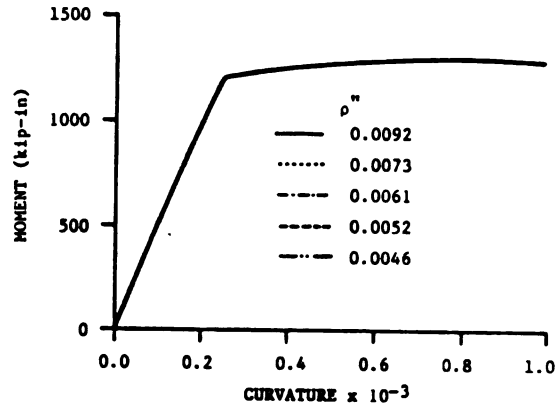

(a) $M - \phi$ curves

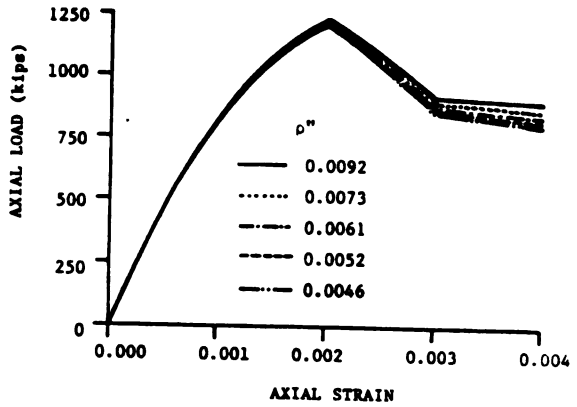

(b) $P - \epsilon_p$ curves

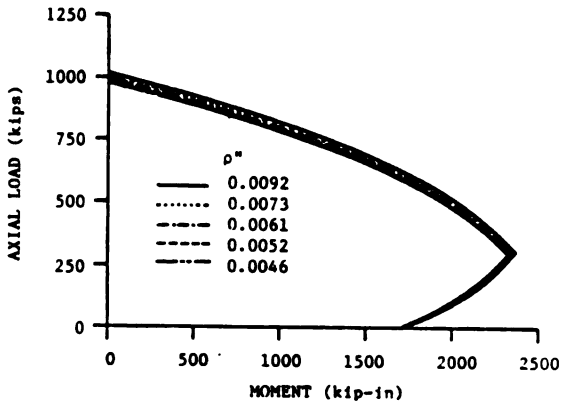

(c) Interaction Curves

Figure 5.8 Effect of Confinement

for the possibility of compression steel buckling. It is shown in Figure 5.8(b) that the column quasi-static compressive strength and ductility (represented by strength at large deformations) are slightly improved by increasing the confinement. Figure 5.8(c) confirms that the confinement effects become slightly larger as the compression action tends to dominate the column behavior.

5.3.5 Effect of the Loading Rate

The loading rate variations are shown in Figure 5.9 to have major effects on the axial/flexural behavior of R/C beams and columns. The data presented in Figures 5.4 to 5.8 were all preduced at quasi-static loading rates (maximum strain rate in the order of 10^{-6}/sec). From Figure 5.9(a) it may be concluded that the flexural strength of the standard beam cross section increases by about 20% as the maximum compressive strain rate of concrete increases from the quasi-static value to 10^{-1}/sec (expected under earthquake and impulsive loads). The initial flexural stiffness of the beam is not, however, significantly influenced by the changes in loading rate. Figures 5.9(b) and (c) indicate that the element axial behavior is more sensitive to the variations in loading rate than its flexural behavior. The compressive strength and secant stiffness are increased by about 30% as the maximum compressive strain rate of concrete in the section is raised from a quasi-static value of 10^{-6}/sec to a dynamic value of 10^{-1}/sec.

5.4 ELEMENT MODEL

The section stiffness matrix derived in section 5.2 was incorporated into an algorithm for nonlinear axial/flexural analysis of R/C cantilever elements. In flexural analysis, the inputs to the element analysis are the increments in lateral displacement, time, bending moment, and axial load at the free end of the cantilever element. In axial analysis, the inputs are the increments in axial deformation

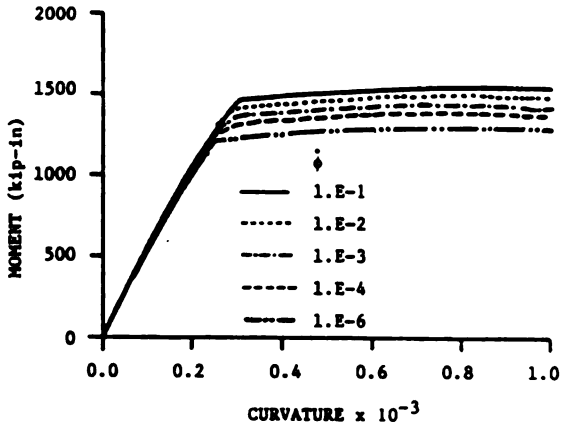

(a) $M - \phi$ curves

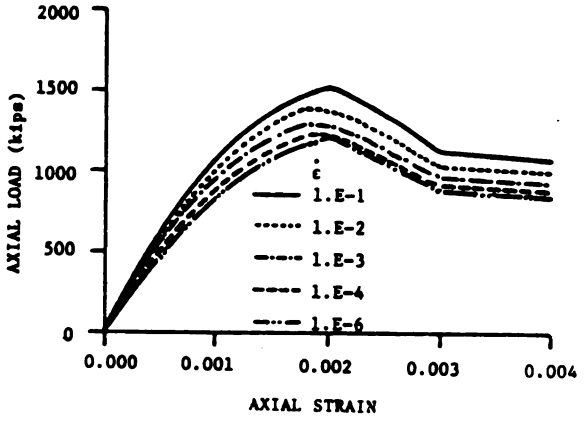

(b) $P - \epsilon_p$ curves

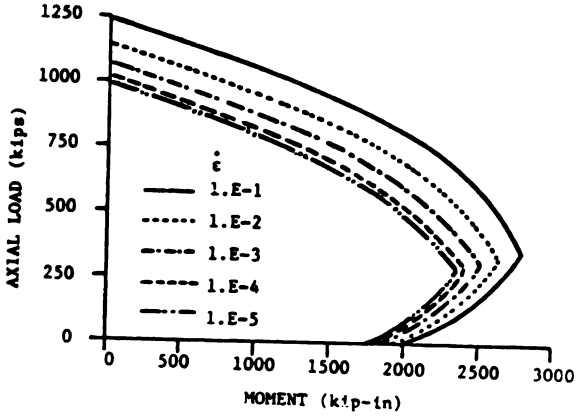

Figure 5.9 Effect of Loading Rate

(of the plastic centroid), time, bending moment and lateral load at the free end. The model for axial/flexural analysis of R/C cantilever elements was constructed by: (a) dividing the element into a number of slices along its length as shown in Figure 5.10(a) (the devisions being more refined near the fixed end that is generally more critically stessed), and (b) subdiving each slice to a number of steel and concrete layers as discussed in the previous section (Figure 5.10b).

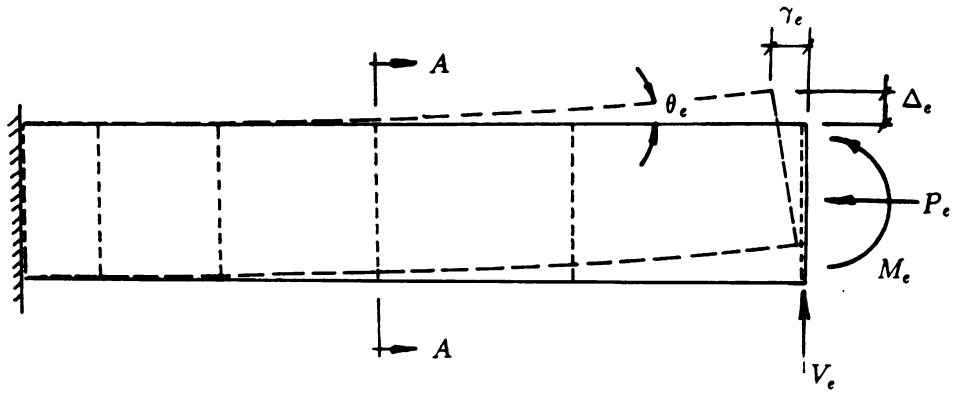

(a) Division of Element by Slices

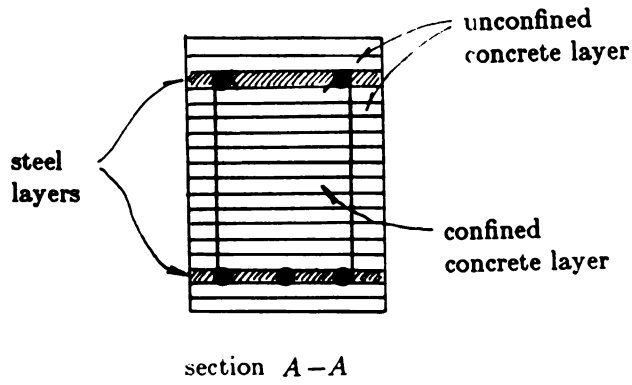

(b) Subdivision of Slices by Layers

Figure 5.10 Layer Model for R/C Elements

The numerical algorithm for inelastic flexural [or axial] analysis of R/C cantilever elements is presented below. This method accounts for the loading rate effects as well as the material and geometric nonlinearities.

(1) Input the incremetal values of free end lateral displacement ($d\Delta_e$), time (dt), bending moment (dM_e), and axial load (dP_e) for flexural analysis [or lateral load (dV_e), time (dt), bending moment (dM_e), and axial displacement ($d\gamma_e$) for axial analysis]; add these increments to the values at the end of the previous time step to get the total amounts.

(2) Estimate the total value of lateral load (V_e) at the free end for flexural analysis [or the total value of axial force (P_e) for axial analysis] at the completion of the current time step.

(3) For each slice:

   (a) calculate the values of axial force and bending moment at the end of current time step resulting from the application of the input (and estimated) values of end flexural, axial and lateral forces. The contribution of axial load to the bending moment (P-Δ effect) should be considered.

   (b) using the strain rate-sensitive section analysis formulations presented earlier, obtain the values of curvature and plastic centroid axial strain corresponding to the values of applied bending moment and axial load at a specified loading rate.

(4) Calculate the end lateral displacement in flexural analysis [or axial displacement in axial analysis] of the element corresponding to the estimated values of end forces by proper integration of the curvatures in flexural analysis [or plastic centroid axial strains in axial analysis] of slices along the element length.

(5) Compare the calulated value of end lateral displacement in flexural analysis [or end axial displacement in axial analysis] with the corresponding input value. If the error is unacceptable, revise the estimated value of lateral force [or axial load], and repeat the procedure from step (3). Otherwise, the analysis for this time step is complete, and the end values of rotation and axial displacement in flexural analysis [or ratation and lateral displacement in axial analysis] can be obtained using the curvatures and plastic centroid axial strains of slices along the element length. The analysis can then be continued for the next time step starting from step (1).

5.5 COMPARISON WITH TEST RESULTS

The developed strain rate-sensitve methods for axial/flexural analysis of R/C elements was used to predict the results of some tests, performed at different loading rates, on R/C columns[4,44] and beams[28].

Reference 14 has reported the results of column tests in which a concentric axial load was applied at a constant displacement rate. The rate of displacement increase varied in different tests. Figures 5.11(a) to (d) compare the experimental axial load-displacement relationships reported in References 4 and 44 with the predictions of the axial analysis procedure introduced in section 5.4. It can be seen in these figures that the loading rate effects on axial behavior of R/C columns are significant, and the developed theoretical approach is capable of closely predicting the test results.

Experimental lateral load-deflection envelope curves for R/C beams loaded at different displacement rates are reported in Reference 28. Figures 5.12(a) and (b) compare these test results with the predictions of the suggested strain rate-sensitive flexural analysis technique. The proposed analytical approach is

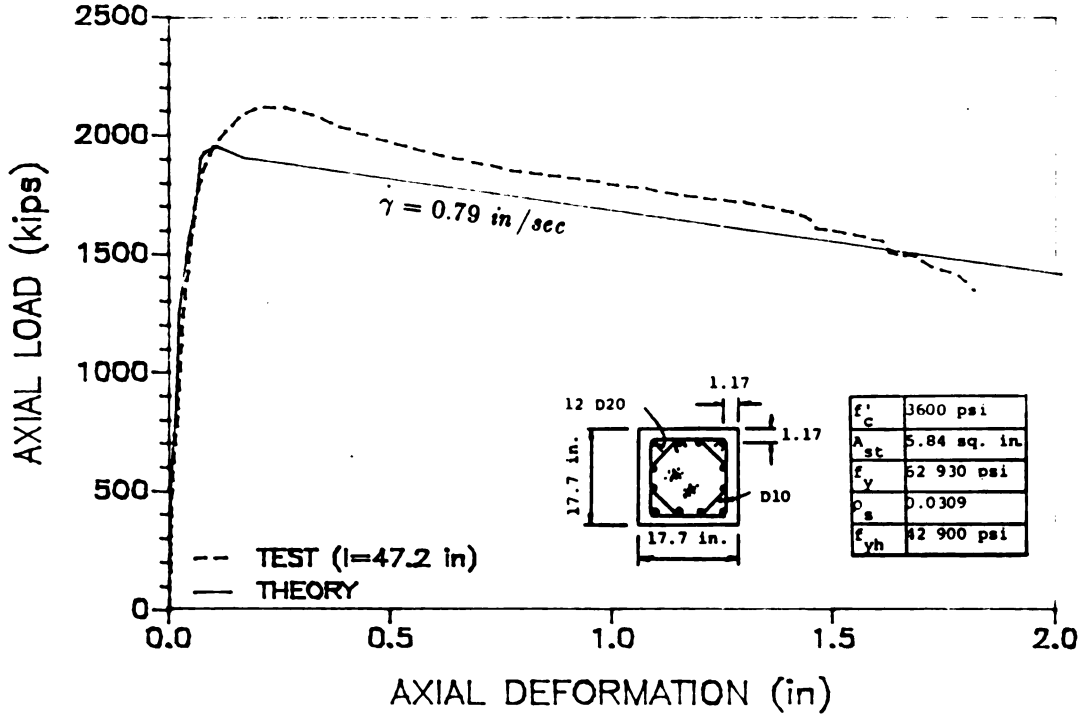

(a) Test Results from Reference 4

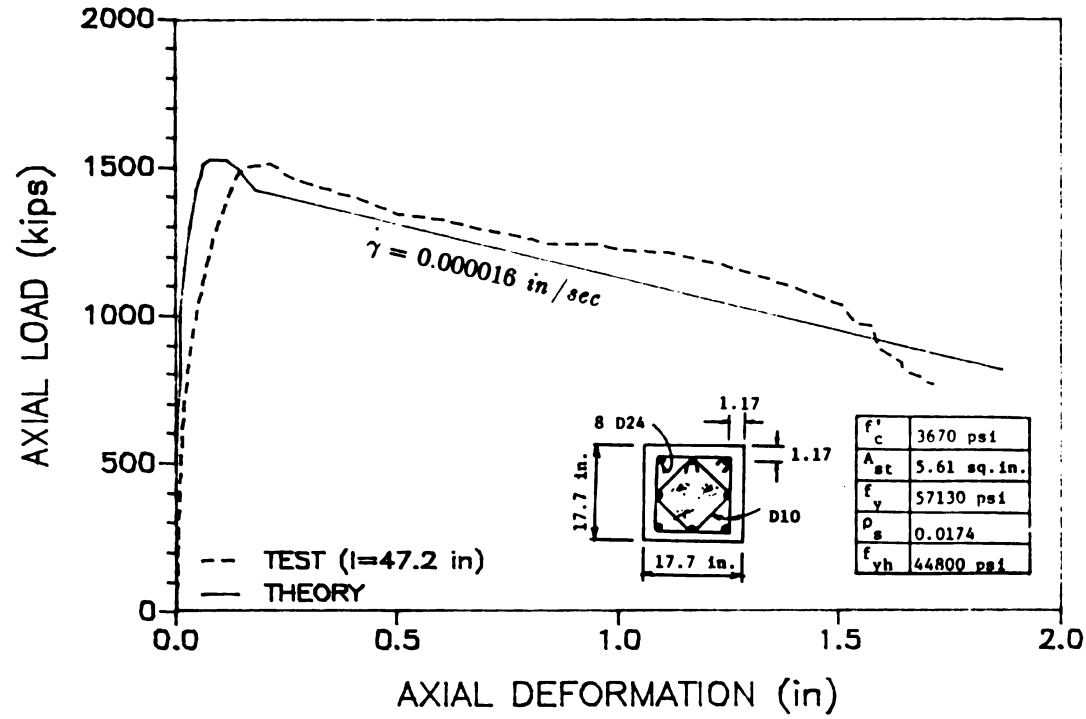

(b) Test Results from Reference 4

Figure 5.11 Experimental and Analytical Axial Performances of R/C Columns at Different Loading Rates

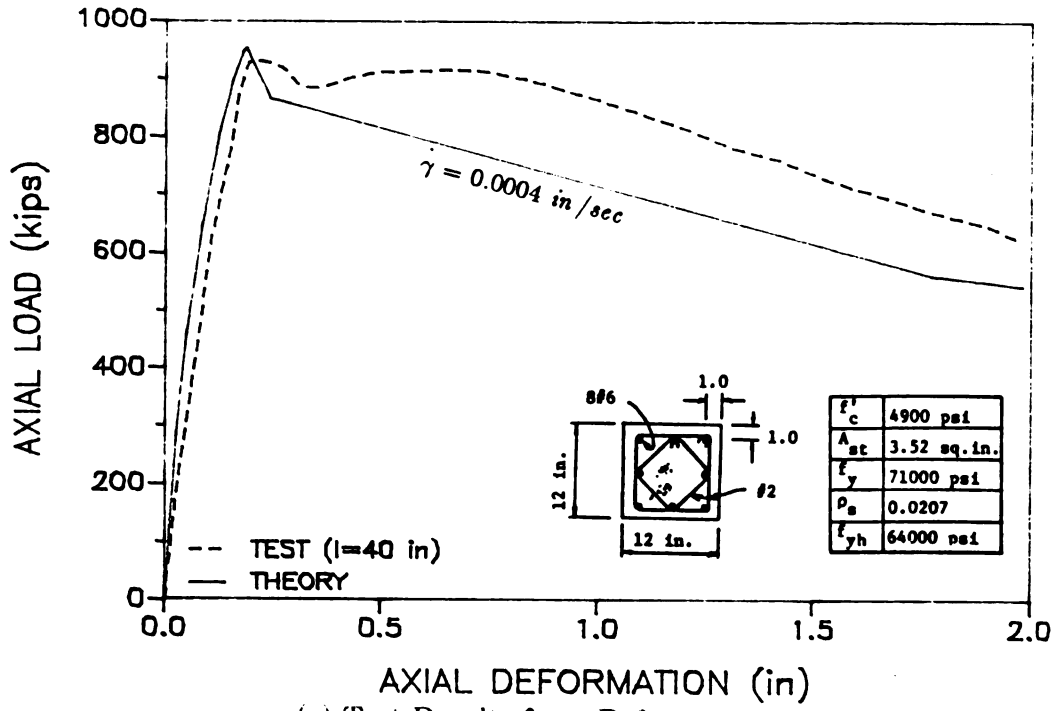

(c) Test Results from Reference 44

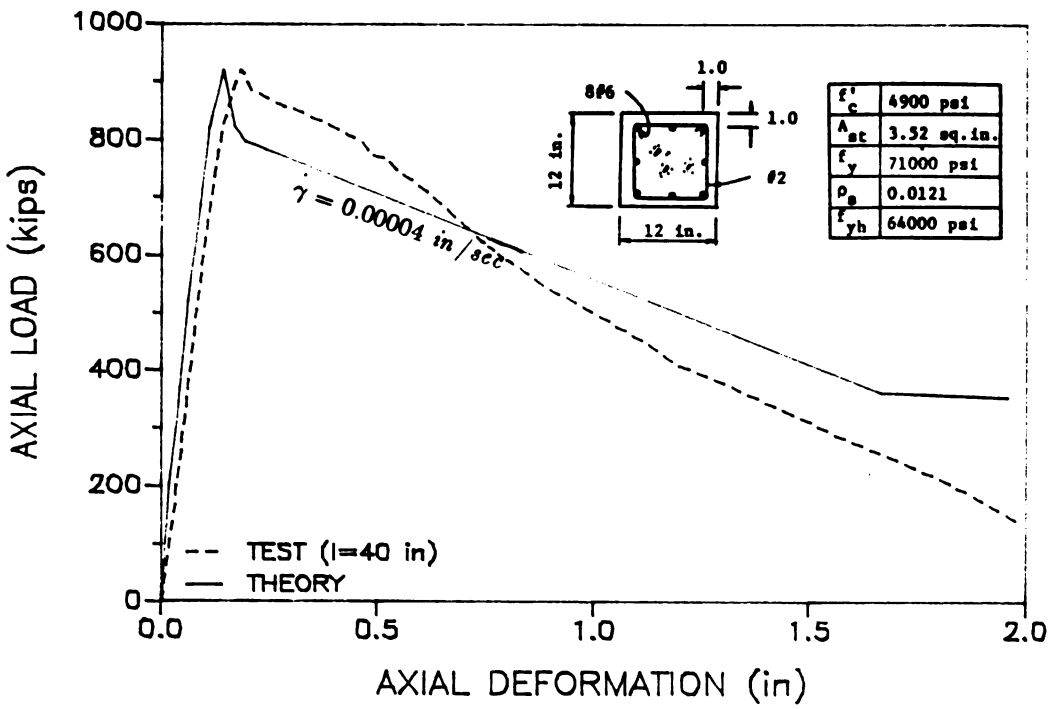

(d) Test Results from Reference 44

Figure 5.11 Experimental and Analytical Axial Performances of R/C Columns at Different Loading Rates(cont'd)

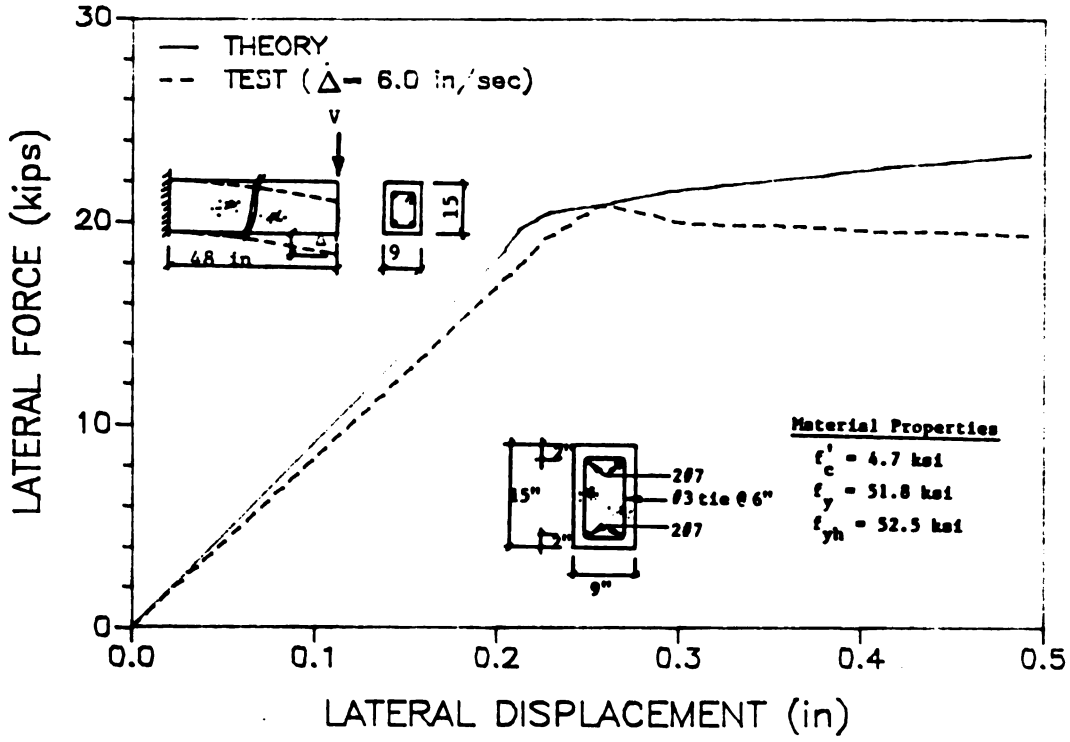

(a) Test Results from Reference 28

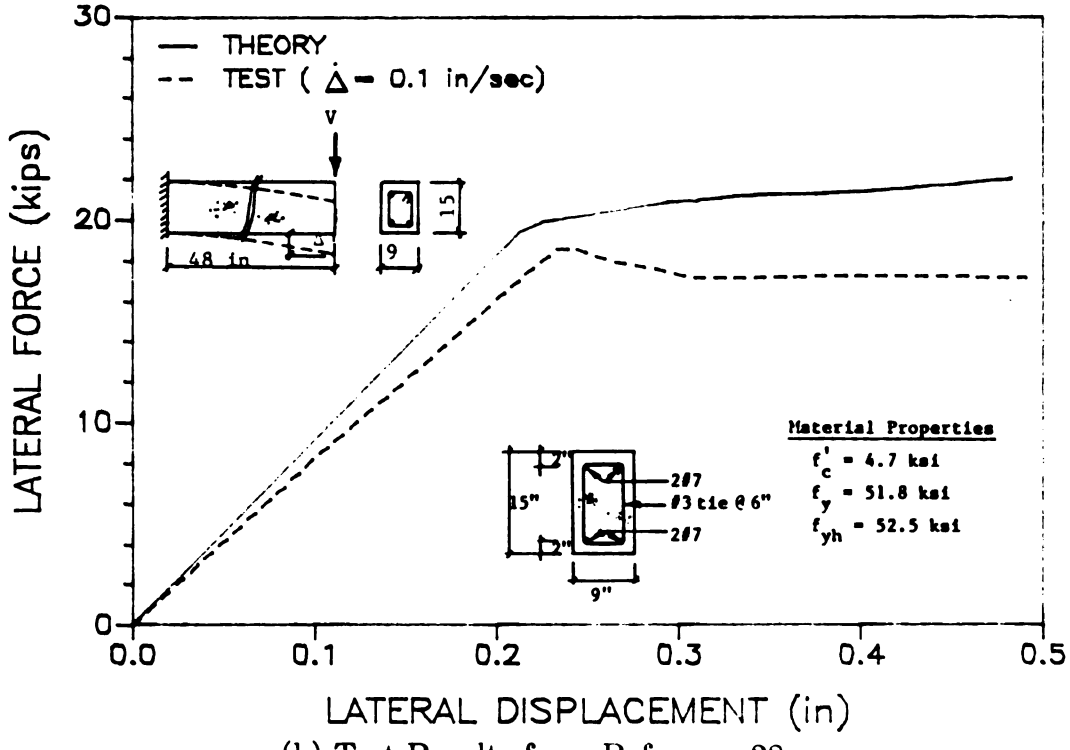

(b) Test Results from Reference 28

Figure 5.12 Experimantal and Analytical Flexural Performances of R/C Beams at Different Loading Rates

observed to compare satisfactorily with test results.

5.6 PARAMETRIC STUDIES ON ELEMENT BEHAVIOR

In this section, the effects of the variations in different material and geometric properties of R/C columns and beams on the sensitivity of their axial/flexural response to strain rate variations are discussed. The following discussion first concentrates on the column axial behavior and then covers the beam flexural performance.

5.6.1 Axial Behavior of Columns

The typical column shown in Figure 5.13(a) was chosen as the "standard" column in this study, and the effects of the variations in different properties of this column on its strain rate-sensitivity were investigated by the developed analytical technique. Figure 5.13(b) presents the axial load-displacement relationships of the standard column derived analytically at four different displacement rates (covering the range from quasi-staic to impulsive loading rates, noticing that even higher loading ratio might occur under impulsive loads). It is obvious in this figure that axial strength and stiffness of the standard column increases with increasing rate of load application. At the highest loading rate, an increase of 30% in column axial strength over the quasi-staic value is observed. The corresponding increase in column secant stiffness (which is measured at 45% of its peak axial strength) is also about 30%. The other observation in this figure is that with increasing loading rate, the deformation at peak axial load is slightly increased.

The effect of loading rate variations on the column axial strength and secant stiffness are summarized, among other information, in Table 5.1. In this table,

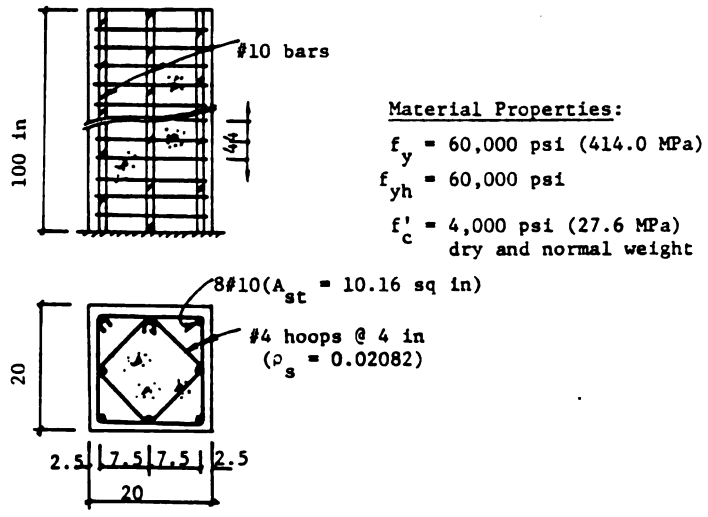

(a) Standard Column

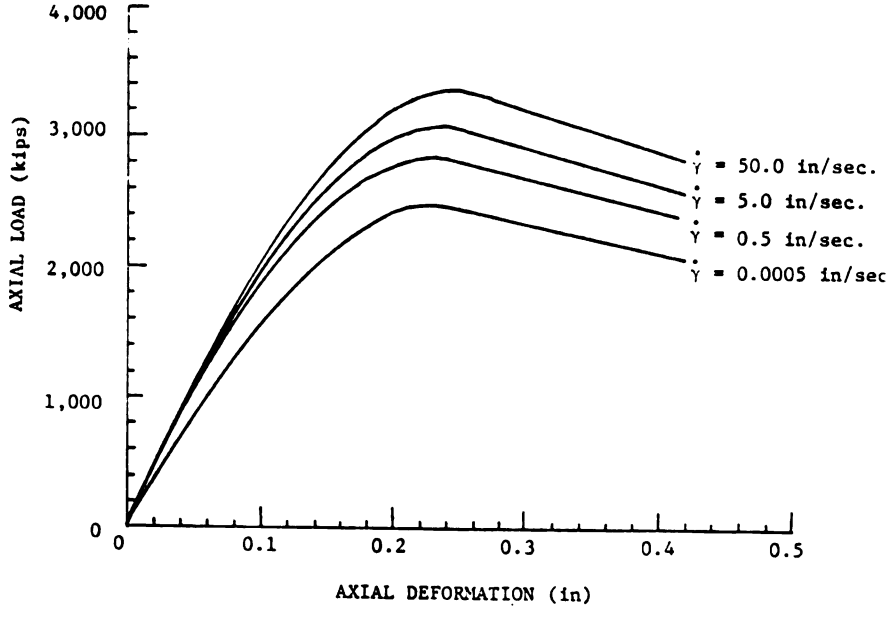

(b) Axial Behavior of Standard Column

Figure 5.13 Loading Rate Effects on The Axial Behavior of R/C Columns

Table 5.1 Summary of The Loading Rate Effects on The Axial Behavior of R/C Columns

SECTION	$\dot{\gamma}$ (*in*/sec)	P_n'/P_n		K_γ'/K_γ
		refined analysis	practical Eqn. (5.6)	refined analysis
standard	0.5	1.16	1.16	1.22
	5.0	1.25	1.25	1.28
	50.0	1.36	1.35	1.31
low f_y ($f_y = 40$ *ksi*)	0.5	1.18	1.17	1.23
	5.0	1.28	1.27	1.28
	50.0	1.40	1.39	1.37
high f_y ($f_y = 80$ *ksi*)	0.5	1.12	1.13	1.23
	5.0	1.20	1.21	1.29
	50.0	1.31	1.30	1.32
low A_{st} ($A_{st} = 8.0\ in^2$)	0.5	1.16	1.16	1.23
	5.0	1.26	1.25	1.29
	50.0	1.37	1.37	1.32
high A_{st} ($A_{st} = 12.48\ in^2$)	0.5	1.15	1.15	1.22
	5.0	1.24	1.24	1.27
	50.0	1.35	1.34	1.30
low confinement ($\rho_s = 0.0139$)	0.5	1.14	1.16	1.23
	5.0	1.23	1.25	1.28
	50.0	1.35	1.35	1.31
high confinement ($\rho_s = 0.4164$)	0.5	1.17	1.16	1.23
	5.0	1.25	1.24	1.26
	50.0	1.37	1.35	1.31
low f_c' ($f_c' = 3$ *ksi*)	0.5	1.16	1.15	1.21
	5.0	1.25	1.24	1.26
	50.0	1.36	1.34	1.29
high f_c' ($f_c' = 6$ *ksi*)	0.5	1.15	1.16	1.24
	5.0	1.25	1.26	1.30
	50.0	1.37	1.37	1.33
saturated concrete	0.5	1.39	1.37	1.51
	5.0	1.69	1.65	1.78
	50.0	2.07	2.00	2.05
circular shape ($D = 22.56$ *in*)	0.5	1.23	1.16	1.15
	5.0	1.29	1.25	1.24
	50.0	1.31	1.35	1.36

P_n and P_n' are the quasi-static and dynamic axial strengths, and K_γ and K_γ' are the quasi-static and dynamic secant axial stiffnesses, respectively. Table 5.1 also summarized the strain rate effects on columns similar to the standard column, except for the change in a single variable which could be confinement, concrete compressive strength, degree of saturation of concrete, or cross sectional shape. From the data presented in Table 5.1, it may be concluded that the variations in steel ratio, concrete compressive strength, confinement and cross sectional shape of columns do not significantly influence the column loading rate-sensitivity. There is, however, a slight increase in the loading rate-sensitivity of column axial strength with decreasing yield strength of steel. Both the axial strength and stiffness of the saturated concrete column are also observed to be far more loading rate-sensitive than those of air-dried concrete columns.

5.6.2 Flexural Behavior of Beams

In the sudies on strain rate-sensitivity of the R/C beam flexural behavior, a typical R/C beam shown in Figure 5.14(a) was chosen as the "standard" one. Figure 5.14(b) shows the lateral load-displacement relationships of this beam derived analytically at four diffrent displacement rates. The flexural strength, but not the initial stiffness of the beam, is observed to increase at higher loading rates. The maximum increase in flexural strength is about 15% at the highest rate of lateral displacement application used in this study. Table 5.2 summarizes the loading rate effects on the lateral strength of the standard R/C beams as well as beams similar to the standard one except for the change in a single variable which could be steel yield strength, concrete compressive strength, the ratio of compression or tension steel, confinement, degree of concrete saturation, or the beam length. In this table, V_n and V_n' are the quasi-static and dynamic values of lateral strength, respectively. From the data presented in Table 5.2, it can be concluded that R/C beams with lower yield strength steels and higher tension to compression steel

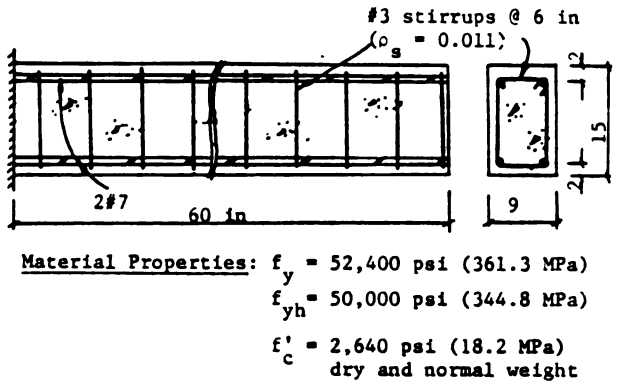

(a) Standard Beam

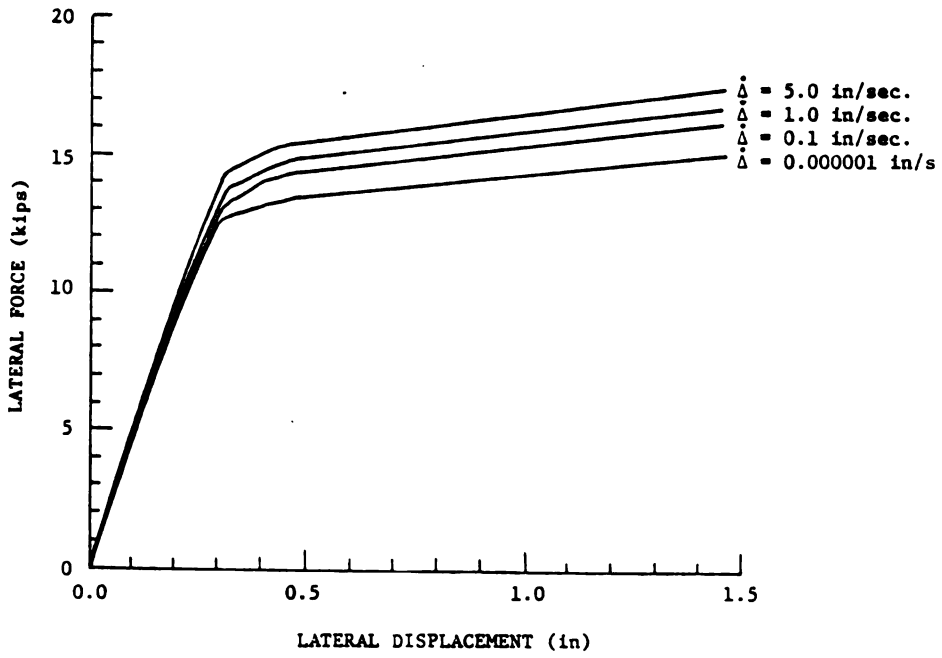

(b) Flexural Behavior of Standard Beam

Figure 5.14 Loading Rate Effects on The Flexural Behavior of R/C Beams

Table 5.2 Summary of The Loading Rate Effects on The Flexural Behavior of R/C Beams

SECTION	$\dot{\Delta}$ (*in*/sec)	V_n'/V_n refined analysis	V_n'/V_n practical Eqn. (5.7)
standard	0.1	1.08	1.09
	1.0	1.11	1.13
	5.0	1.15	1.18
low f_y ($f_y = 40$ *ksi*)	0.1	1.11	1.10
	1.0	1.14	1.15
	5.0	1.17	1.21
high f_y ($f_y = 60$ *ksi*)	0.1	1.08	1.08
	1.0	1.10	1.12
	5.0	1.13	1.16
low A_s' ($A_s' = 0.61\ in^2$)	0.1	1.08	1.09
	1.0	1.12	1.13
	5.0	1.17	1.18
high A_s ($A_s = 2.0\ in^2$)	0.1	1.10	1.09
	1.0	1.15	1.14
	5.0	1.18	1.18
high confinement($\rho_s = 0.016$)	0.1	1.07	1.09
	1.0	1.10	1.13
	5.0	1.15	1.18
high f_c' ($f_c' = 6$ *ksi*)	0.1	1.07	1.09
	1.0	1.12	1.13
	5.0	1.15	1.17
saturated concrete	0.1	1.09	1.09
	1.0	1.13	1.12
	5.0	1.17	1.16
T - beam (flange width = 18 *in*)	0.1	1.08	1.07
	1.0	1.11	1.12
	5.0	1.15	1.16
short beam ($l = 40$ *in*)	0.1	1.09	1.10
	1.0	1.12	1.14
	5.0	1.15	1.19

ratios are more sensitive to the variations in loading rate. Beams with saturated concrete are also more loading rate-sensitive than those with air-dried concrete. The variations in concrete compressive strength and confinement, element length, and cross sectional shape do not seem to influence the loading rate-sensitivity of the flexural behavior of R/C beams.

5.7 PRACTICAL DESIGN PROCEDURES

The layer modeling technique developed in this chapter for loading rate-sensitive axial/flexural analysis of R/C elements is not convenient for every day use by designers. This section illustrates two simple design techniqes developed for computing the axial and flexural strengths of R/C cross sections as functions of the applied deformation rates. The results of these simple techniques are also compared with those obtained from the more refined layer analysis procedures described in section 5.2.

5.7.1 Dynamic Axial Strength

ACI code (318-83)[9] suggests the following equation for calculating the nominal axial strength (P_n) of R/C columns:

$$P_n = 0.85\, f_c^{'}\, (A_g - A_{st}) + A_{st}\, f_y \tag{5.5}$$

where,

A_g = gross cross sectional area of concrete;
A_{st} = total area of longitudinal steel.

The above equation has been based on the results of quasi-static tests. This equation can be modified as follows for calaulating the column axial strength at high loading rates ($P_n^{'}$):

$$P_n^{'} = 0.85\, f_c^{''}\, (A_g - A_{st}) + A_{st}\, f_y^{'} \tag{5.6}$$

where,

f_c'' = dynamic compressive strength of concrete (psi);

$$= \begin{cases} f_c' \left[1.48 + 0.160 \log_{10}\dot{\epsilon} + 0.0127(\log_{10}\dot{\epsilon})^2\right] \\ \qquad \text{for air-dried concrete} \\ f_c' \left[2.54 + 0.580 \log_{10}\dot{\epsilon} + 0.0543(\log_{10}\dot{\epsilon})^2\right] \\ \qquad \text{for saturated concrete} \end{cases}$$

f_y' = dynamic yield strength of steel (psi);

$= f_y \left[-4.51 \times 10^{-6} f_y + 1.46 + (-9.20 \times 10^{-7} f_y + 0.0927) \log_{10}\dot{\epsilon}\right]$;

$\dot{\epsilon}$ = strain rate (1/sec) $\geq 10^{-5}$;

f_y = standard (quasi-static) yield strength of steel (psi).

Table 5.1 compares the ratios of dynamic to static compressive strengths obtained from the above equation with those obtained from the refined (layer) analysis procedure described earlier. The suggested simple approach is observed to compare well with the test results of the refined analysis.

5.7.2 Dynamic Flexural Strength

The ACI code (318-83)[9] flexural design procedure is based on simplified ultimate flexural strain and stress distributions at cross section shown in Figure 5.15. It should be noticed that the tension steel area in this approach is assumed to be small enough (i.e. below balanced area) such that the tension steel yields at the ultimate flexural condition. In order to develop a simple procedure for computing the dynamic flexural strength of R/C beams, it was assumed that the absolute values of strain rate in concrete under compression and steel under compression and tension are equal to the rate of straining at the extreme compression fiber. This assumption leads to the following procedure for calculating the loading rate-sensitive flexural capacity of a doubly reinforced beam cross section:

(1) Assume a value for the depth of neutral axis (c in Figure 5.15).

(2) Find steel stresses:

$$\text{In compression, } f_{sc} = 87{,}000\frac{c - d'}{c} \leq f_y'$$

$$\text{In tension, } f_y'$$

(3) Find the new value of c for the above steel stresses:

$$a = \frac{A_s f_y' - A_s' f_{sc}}{0.85 f_c'' b}$$

$$c = \frac{a}{\beta_1}$$

where,

$$\beta_1 = 0.85 - \frac{0.05(f_c'' - 4{,}000)}{1{,}000} \qquad \text{but, } 0.65 \leq \beta_1 \leq 0.85$$

(4) Repeat from step (2) with the new value of c until the change in c is realtively small.

(5) Find the strain rate-dependent flexural strength of the section:

$$M_n' = A_s f_y'(d - d') + 0.85 f_c'' ab\left(\frac{a}{2} - d'\right) \tag{5.7}$$

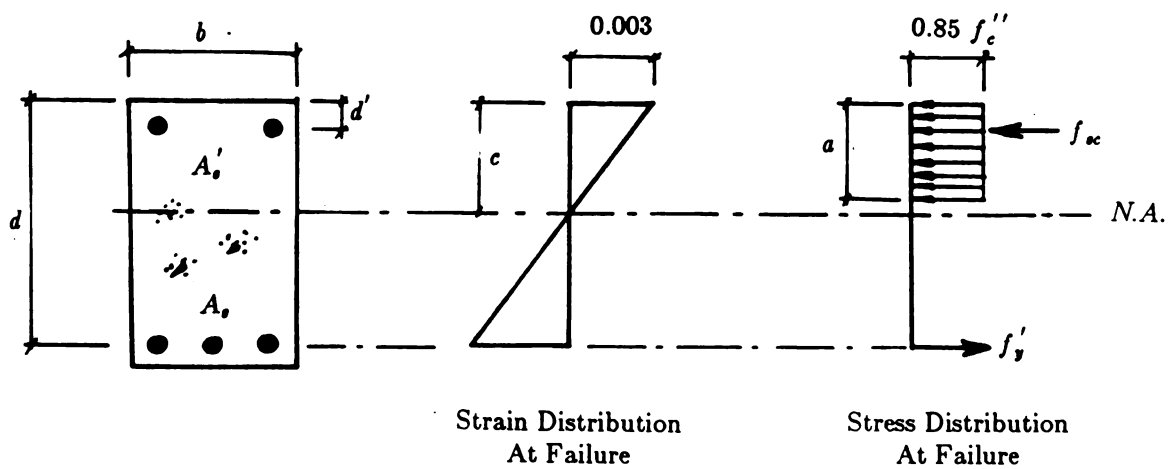

Figure 5.15 Simplified Flexural Strain and Stress Distributions at Failure

The value of strain rate at the extreme compressive fiber ($\dot{\epsilon}$) used for calculating $f_y^{'}$ and $f_c^{''}$ in the above equation should be obtained from the given rates of displacement application to the beam, using approximate analytical techniques.

The suggested procedure for calculating the loading rate-dependent flexural strength of R/C sections was applied to all the beams used in the numerical study discussed earlier. The results are compared with the predictions of the refined (layer) modeling technique in Table 5.2, and the comparison is observed to be satisfactory.

5.8. SUMMARY AND CONCLUSIONS

Empirical strain rate-sensitive constitutive models of steel and concrete were incorporated into an analytical procedure for axial/flexural analysis of R/C beam-columns at different loading rates. The analytical predictions compared well with quasi-static and dynamic test results. Simple practical analysis procedures were also developed for calculating the axial and flexural strengths of R/C columns and beams as functions of the applied loading rates.

The refined (layer) analytical method was used to perform a numerical study on the sensitivity of the axial and flexural performances of R/C sections and elements to the changes in steel and concrete strengths, concrete confinement and the rate of load application. The results of this numerical study indicated that:

(a) Variations in longitudinal steel yield strength have major effects on the flexural strength, and some important effects on the axial strength of the typical beam and column cross sections considered in this study ($\pm$ 30% variations in the longitudinal steel yield strength causes changes of the order of $\pm$ 30% in flexural strength and $\pm$ 10% in axial compressive strength). The axial and flexural stiffnesses, however, are not much influenced by the varia-

tions in yield strength.

(b) Variations in the concrete compressive strength have relatively small effects on the beam flexural behavior, but major effects on the column compressive stiffness and strength. For the typical beam and column cross sections studied here, ± 30% changes in concrete compressive strength resulted in variations of about ± 3% and ± 25%, respectively, in the flexural and compressive strengths (and stiffnesses).

(c) The flexural behavior of reinforced concrete beam sections is strongly influenced by the variations in the tension steel ratio, but not much by the changes in compression steel ratio. A ± 30% change in tension steel ratio results in about ± 30% change of a typical beam flexural stiffness and strength. The axial strength and stiffness of R/C column cross sections are also found to be sensitive to the variations in their total steel area. Changes of the order of ± 15% were observed in strength of a typicaal column as a result of ± 30% changes in the total steel area.

(d) Increased confinement does not have major effects on the beam flexural behavior (neglecting the possibility of compression steel buckling). It, however, slightly increases the compression strength and ductility of the column.

(e) Under typical impulsive loading rates, the axial strength and stiffness of typical R/C columns increase by about 30% over the corresponding quasi-static values.

(f) The flexural strengths of typical R/C beams increase by about 15% at typical impulsive loading rates over the quasi-static values. The flexural stiffnesses of R/C beams is not much influenced by the loading rate variations.

(g) The loading rate-sensitivity of R/C column axial behavior increases with decreasing yielding strength and increasing degree of saturation of concrete.

The variations in steel ratio, concrete compressive strength, confinement and cross sectional shape of columns do not significantly influence the column loading rate-sensitivity.

(h) The loading rate-sensitivity of R/C beam flexural behavior increases with decreasing steel yield strength and increasing steel ratio and concrete degree of saturation. The variations in concrete compressive strength, confinement, and element length and cross sectional shape do not significantly influence the loading rate-sensitivity of R/C beams in flexure.

CHAPTER 6

INELASTIC MODELING OF REINFORED CONCRETE ELEMENTS UNDER CYCLIC FLEXURAL AND SHEAR FORCES

6.1 INTRODUCTION

Total lateral displacements in reinforced concrete beams result from the flexural and shear deformations. Each of these displacement components has distinct hysteretic characteristic (Figure 6.1) [6,28]. The shear hysteresis is distinguished from the flexural one by severe stiffness and strength deteriorations and lower energy dissipation. Shear deformations, due to their deteriorating nature, tend to gradually dominate the lateral response of R/C beams to repeated inelastic load reversals.

The available analytical models for predicting the hysteretic behavior of R/C beams are generally based on the assumption that flexure fully dominates the element behavior[32]. These models can not properly idealize the inelastic shear deformation, and this generally leads to poor comparisons between the analytical and experimental hysteretic curves, especially after large inelastic cyclic deformations in elements subjected to relatively high shear stresses.

A practical model for predicting the hysteretic behavior of R/C beams has been developed in this chapter. The model accounts for the distinct hysteretic characteristics of shear and flexural deformations, and its predictions compare well with test results performed on R/C elements with a variety of geometric and material properties.

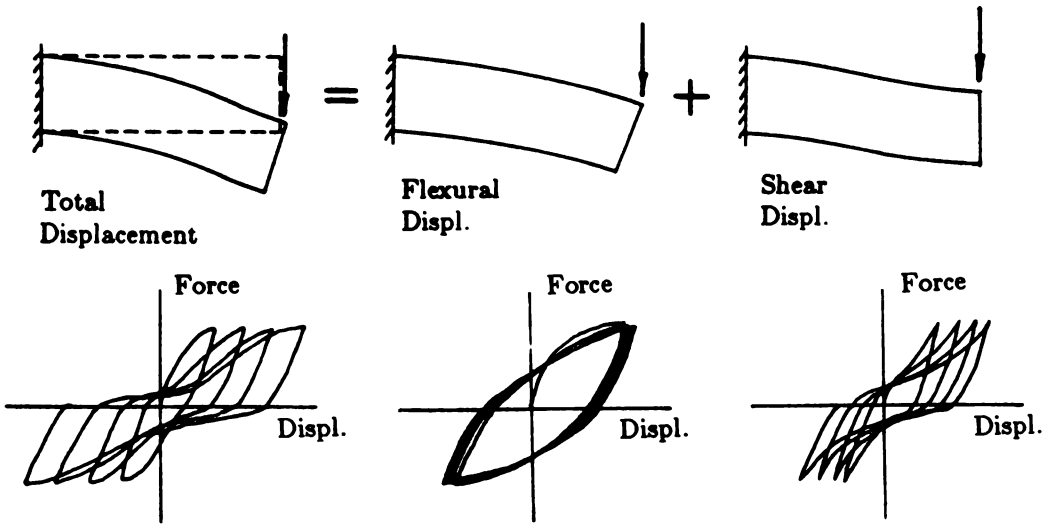

Figure 6.1 Lateral Displacement Components of R/C Beams, and Their Hysteretic Characteristics

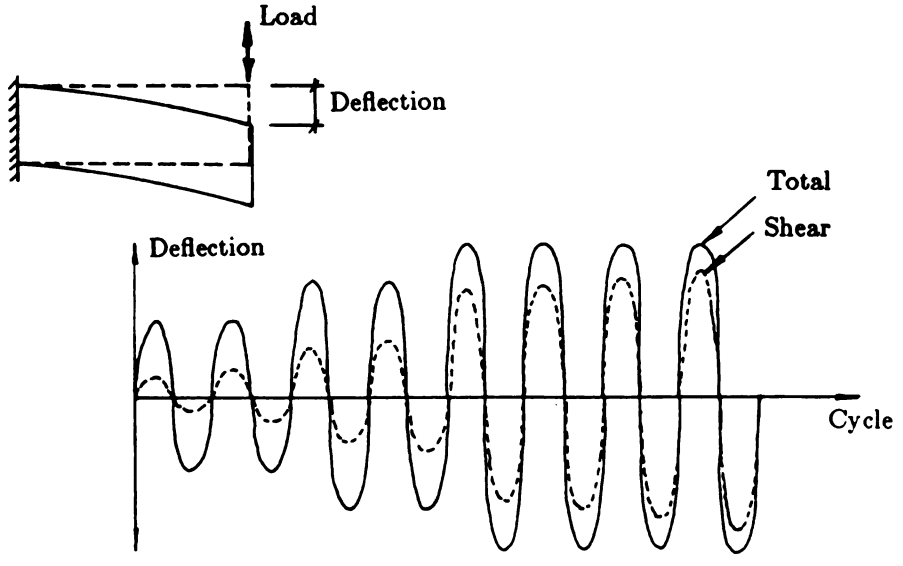

Figure 6.2 Contrtibution of Shear Deformations to The Overall Element Displacements under Cyclic Loads

6.2 BACKGROUND

In this section, first the hysteretic characteristics of R/C beams observed in test results will be discussed, and then the available models for these characteristics will be critically reviewed. The section will conclude with a brief discussion on the influence of element models on the overall seismic response characteristics of R/C structures.

6.2.1 Test Results

Reference 33 has compared the histories of shear and flexural displacements in a beam under cyclic loads (Figure 6.2). The results confirmed that the shear deformations, due to their deteriorating nature, tend to dominate the behavior at later cycles.

The beam inelastic deformations are generally concentrated in the critical regions near the beam-column connections, where the flexural and shear forces are both relatively large. The performance in these regions is marked by the appearance of flexural and shear cracks (Figure 6.3a) which intersect the opposite cracks under load reversals (Figure 6.3b) and from vertical slip lines[45].

The relatively small flexural degradations observed under cyclic loads are usually attributed to the reduction in stiffness during the closure of cracks (that have opened under loads in the opposite direction), the Bauschinger effect in steel bars, and buckling of the compression reinforcement[45,46]. The relatively large shear deteriorations are caused by closure of the diagonal cracks that remain open when the loading in the opposite direction is removed, sliding shear along the vertical slip lines shown in Figure 6.3(b), and the loss of shear transfer by truss action resulting from spalling of the concrete in critical regions[6,8,28,46].

The R/C beam hysteretic characteristics are influenced by the element shear stress level (or shear span-to-depth ratio), longitudinal steel percentage and configuration, and transverse steel ratio. In general, the stiffness and strength

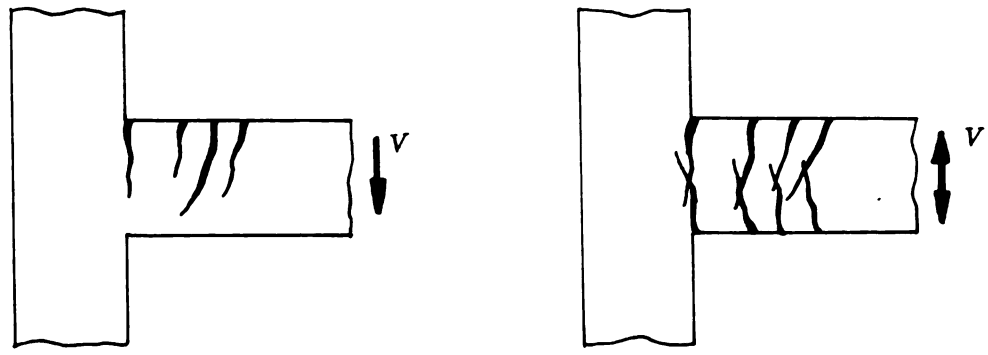

(a) Under Monotonic Load (b) Under Cyclic Load

Figure 6.3 Typical Crack Patterns in Critical Regions of R/C Elements

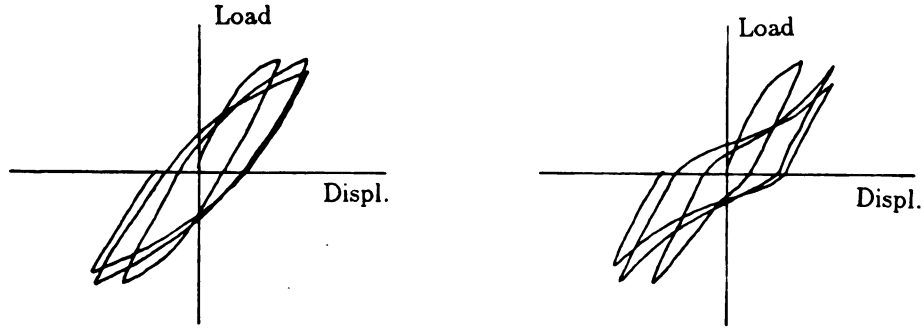

(a) Low Shear Stress Level (b) High Shear Stress Level

Figure 6.4 Effect of The Shear Stress Level on The Overall Hysteretic Characteristics of R/C Beams

deteriorations are more pronounced in elements with higher shear stress levels[7,45,46](see Figure 6.4). An increase in the percentage of longitudinal steel increases the flexural stength and consequently the maximum shear stresses that can be applied in R/C beams. This increase in shear strength seems to be the main reason for the inferior hysteretic behavior of elements with higher longitudinal steel ratios[45,46]. The configuration of longitudinal steel also influences the element hysteretic characteristics. With the ratio of top to bottom steel areas approaching unity, the flexural hysteresis is observed to become more stable[46]. Finally, the increase in transverse steel ratio generally improves the element hysteretic behavior by increasing the shear friction resistance, confinement of the concrete core, and by providing support against buckling of the longitudinal bars[7,45].

6.2.2 Analytical Models

This section briefly reviews the common physical idealizations for simulating the flexural and shear behaviors of R/C beams, and then presents the hysteretic models commonly applied to R/C elements.

The flexural behavior of R/C beams has been physically idealized by the layer modeling technique[16] (Figure 6.5a), the multi-spring models[32] (Figure 6.5b), the single component simulation[8] (Figure 6.5c), the parallel multi-component models[47] (Figure 6.5d), and the single component models with distributed inelasticities[32] (Figure 6.5e). The physical idealizations of shear behavior in R/C beams have generally been based on a rotational simulation[48] (Figure 6.6a), a truss simulation[8] (Figure 6.6b), or a single spring simulation[8] (Figure 6.6c) of the performance. Many investgators have neglected the shear deformation, and some have assumed that the ratio of shear to flexural stiffnesses in the inelastic range is constant and equal to this ratio in the elastic range[28,32].

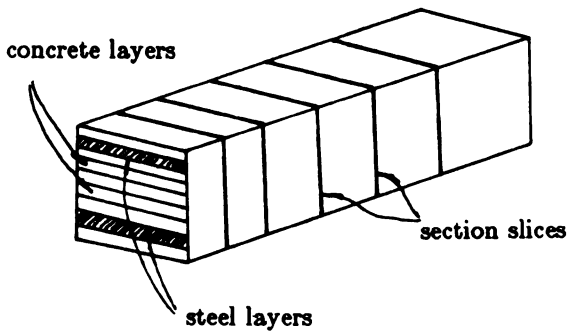

(a) Fiber Model

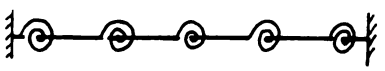

(b) Multiple Spring Model

(c) Single Component Model

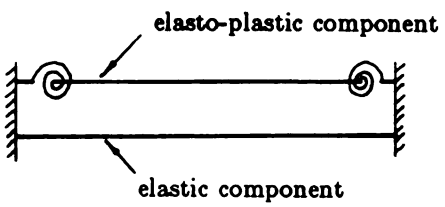

(d) Multi-Component Model

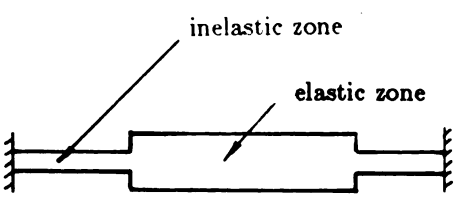

(e) Single Component Model with
Distributed Inelasticities

Figure 6.5 Physical Models for Simulating The Flexural Behavior of R/C Beams

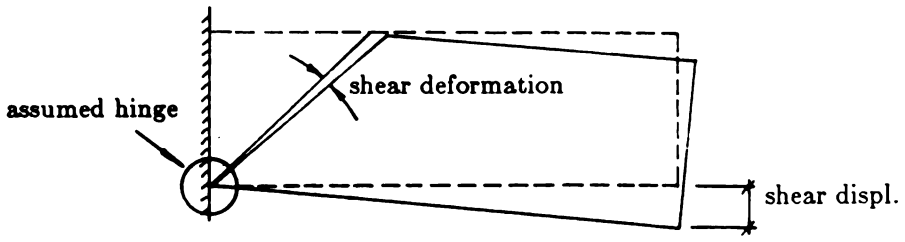

(a) Rotational Idealization

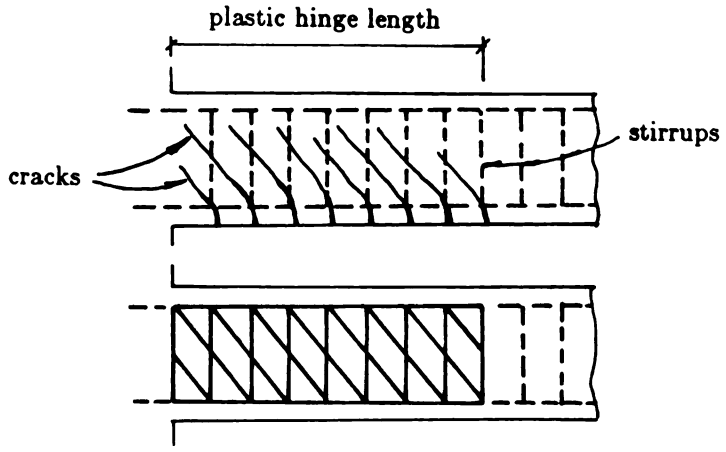

(b) Truss Idealization

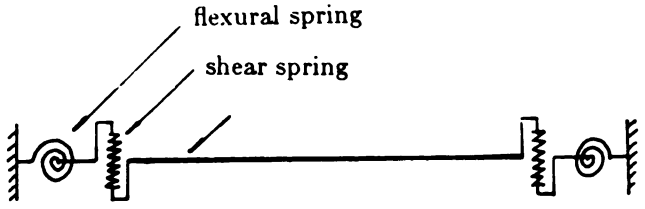

(c) Spring Idealization

Figure 6.6 Physical Models for Simulating The Shear Behavior of R/C Beams

The physical models presented above generally require certain hysteresis rules for predicting the element behavior under cyclic loads. A wide variety of hysteresis models (or rules) are available in the literature, a number of which are presented in Figure 6.7 [8,32,37,48-54].

The avialable analytical models for predicting the hysteretic behavior of R/C beams, usually consisting of a physical model (Figures 6.5 and 6.6) and some hysteretic rules (Figure 6.7), generally disregard the significant increase in shear deformations caused by repeated inelastic load reversals. A very popular (and typical) model proposed in Reference 55 has been based on a single component physical idealization of flexural behavior (Figure 6.5c) and the Takeda hysteresis rules (Figure 6.7c). The shear deformations are accounted for in this model by assuming that the ratio of the shear to flexural deformations is constant in both the elastic and inelastic ranges. This ratio is, however, relatively small in the elastic range and it has been observed to increase (due to the more severe deteriorations of the shear resisting mechanisms compared with the flexural ones) under inelastic load reversals. Disregard for this increase in shear deformations is shown in Figures 6.8(a), (b), and (c) to lead to major discrepancies between the analytical and experimental results. These discrepancies are observed to be more pronounced for beams with smaller shear span-to-depth ratios (and consequently higher shear stress levels).

The analytical predictions of the inelastic seismic response characteristics of R/C frames have generally been based on element models incapable of accurately predicting inelastic shear deformations. Large deviations from test results, similar to the one shown in Figure 6.8, are expected in the analytical predictions of these element models. This shortcoming can produce large discrepancies in the predicted response of frame structures (especially those with relatively deep elements) under severe seismic excitations. The disregard for the deteriorations in

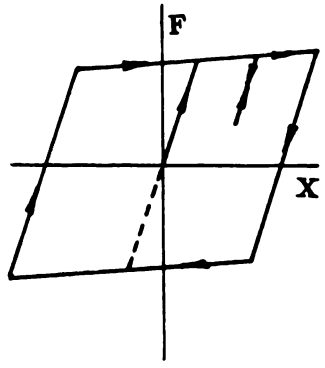

(a) Bilinear Model

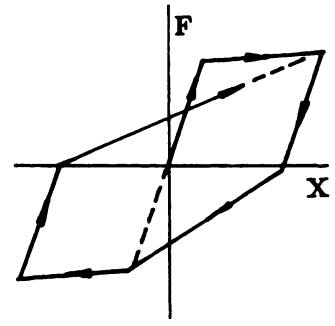

(b) Clough Model[49]

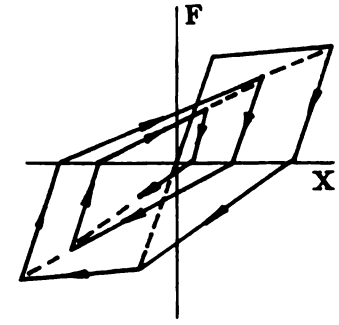

(c) Takeda Model[50]

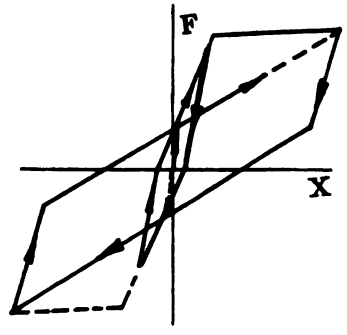

(d) D-Tri Model[8]

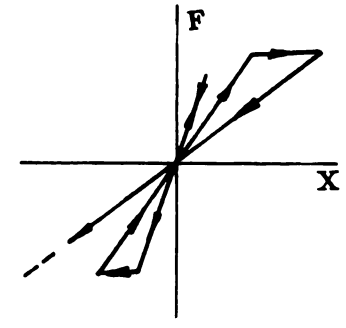

(e) Origin-Oriented Model[8]

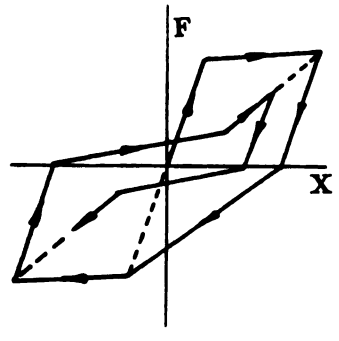

(f) Sinha Model[53]

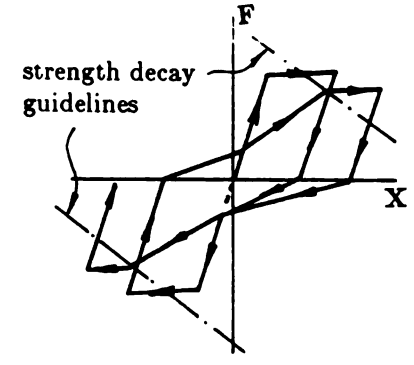

(g) Model with Strength Decay[32]

Figure 6.7 Examples of Hysteretic Models

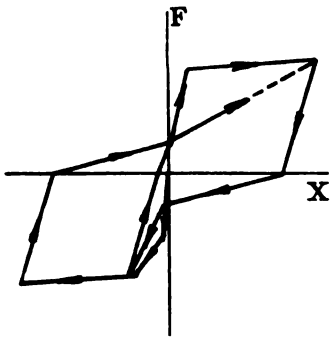

(h) Kustu Model for Flexure[48]

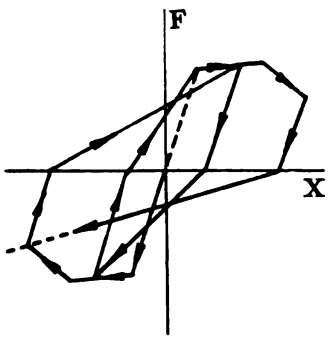

(i) Kustu Model for Shear[48]

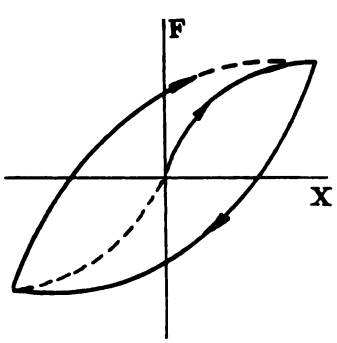

(j) Ramberg-Osgood Model[51]

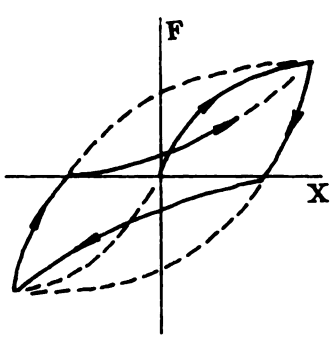

(k) Celebi Model[52]

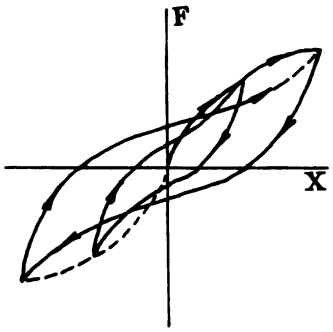

(l) Cubic Model[54]

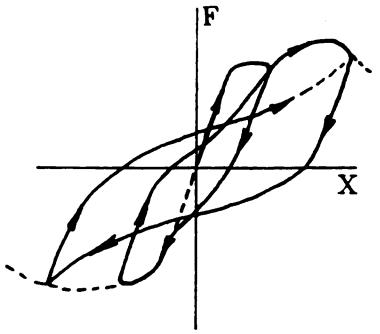

(m) Modified Cubic Model[37]

Figure 6.7 Examples of Hysteretic Models(cont'd)

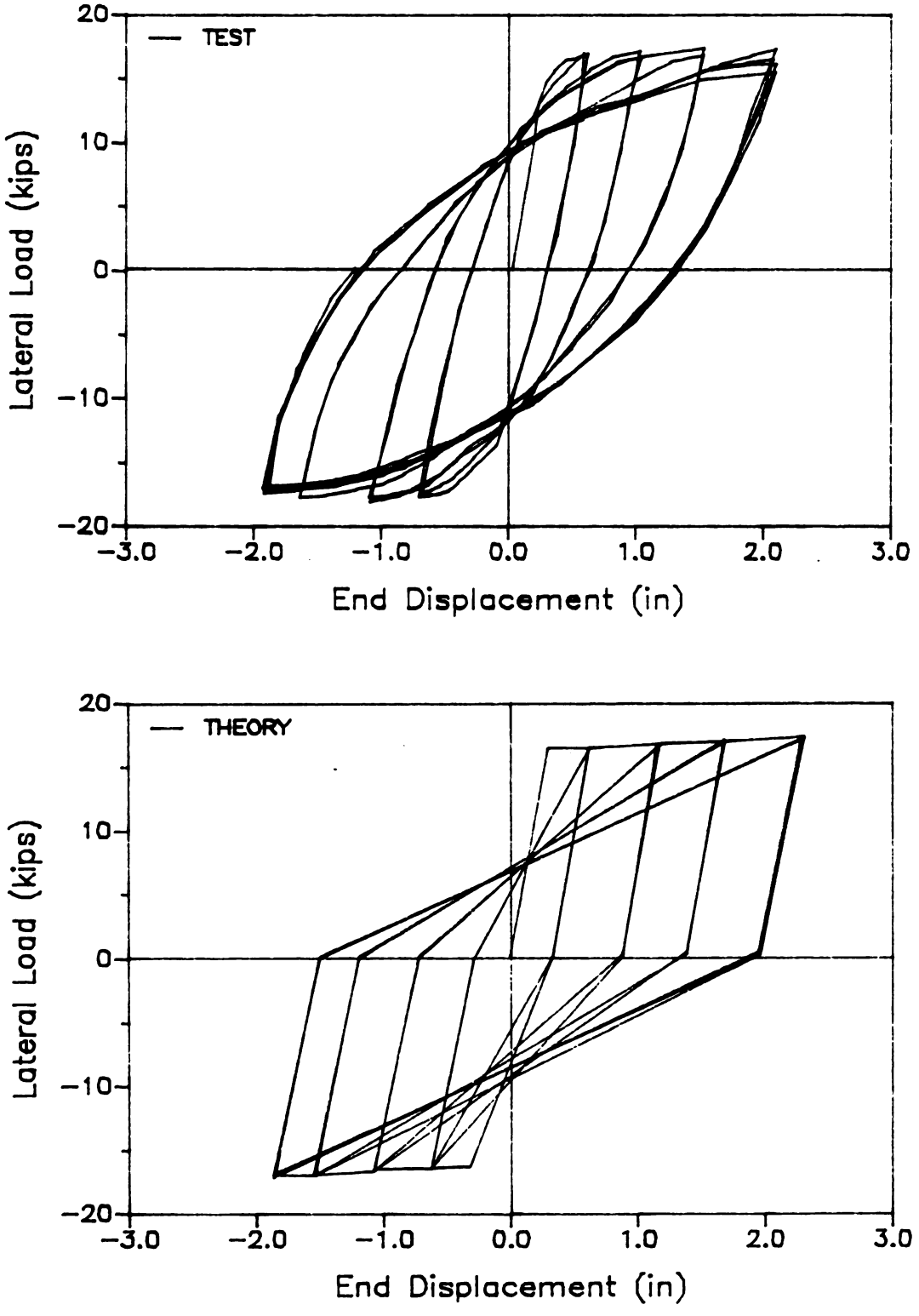

Figure 6.8(a) Comparison of Experimental and Analytical Cyclic Load-Deflection Relationships for R/C Beams with large a/d

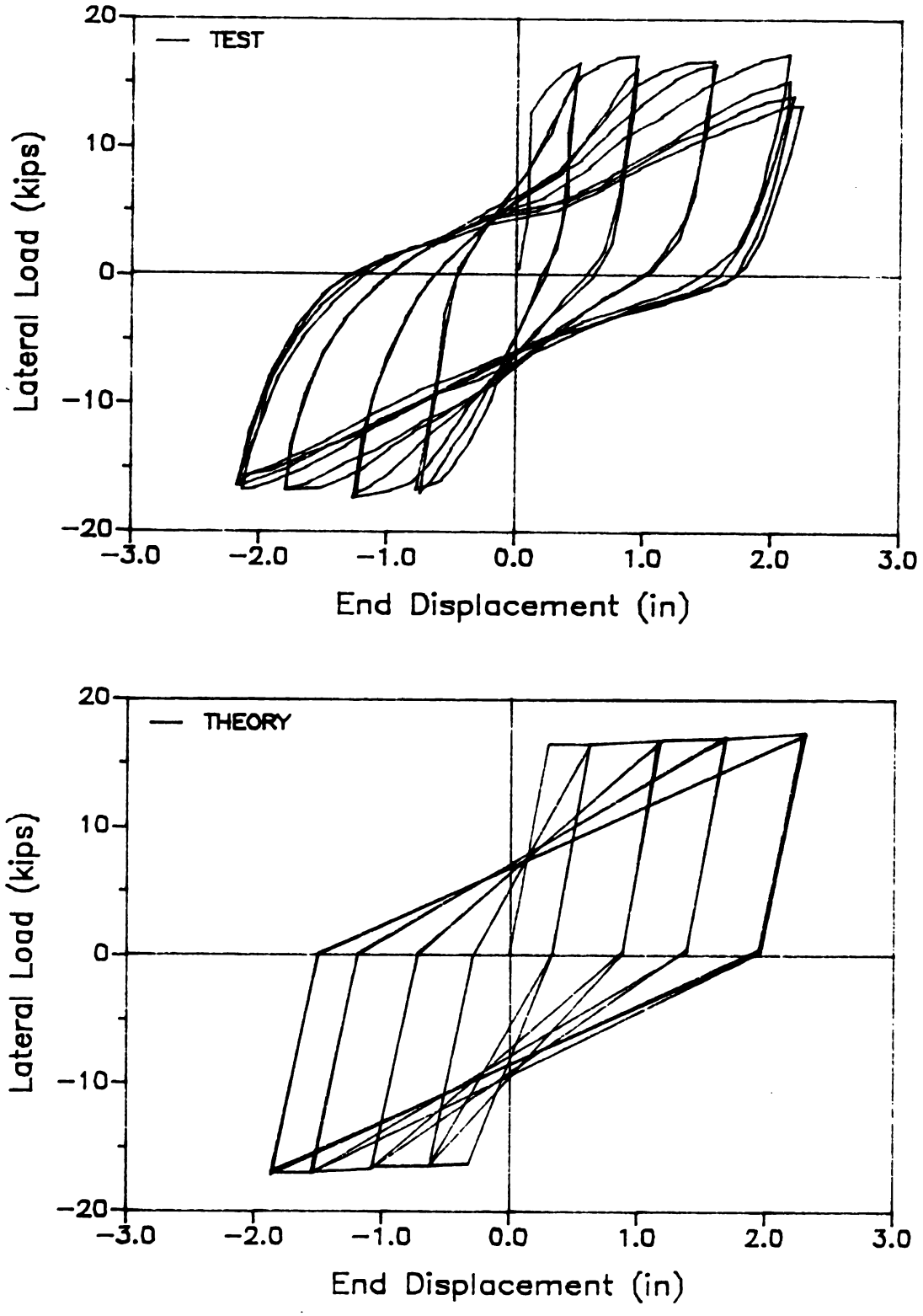

Figure 6.8(b) Comparison of Experimental and Analytical Cyclic Load-Deflection Relationships for R/C Beams with medium a/d

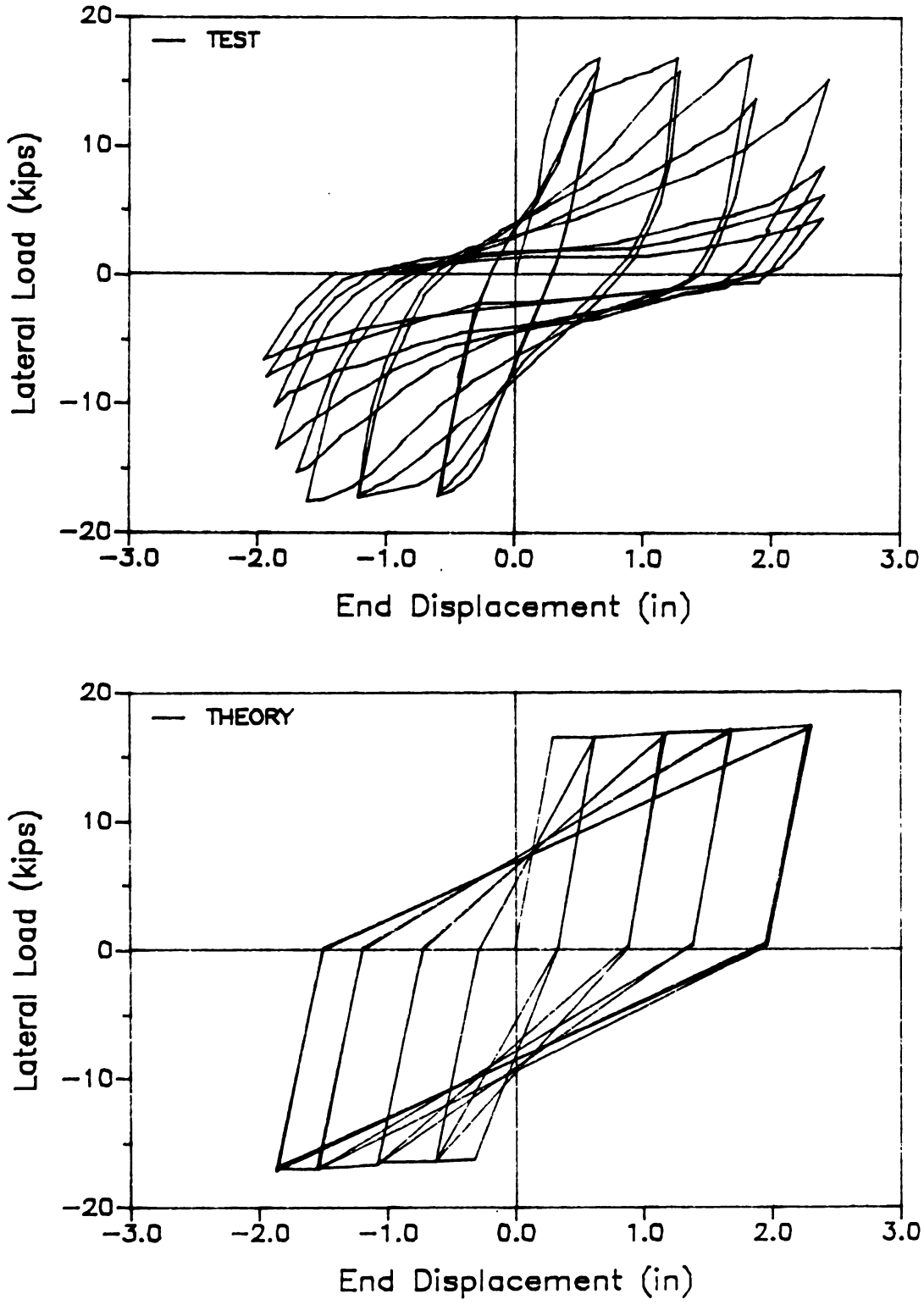

Figure 6.8(c) Comparison of Experimental and Analytical Cyclic Load-Deflection Relationships for R/C Beams with small a/d

shear stiffness and strength have been observed to result in increased deformations, longer periods of vibration and premature failures in actual structures when compared with the idealized ones under earthquake ground motions. Hence, it is important to develop element models which account for the inelastic shear deformations in predicting the hysteretic behavior of R/C beams, in order to achieve more reliable predictions of nonlinear seismic response characteristics of R/C structures.

6.3 THE PROPOSED ELEMENT MODEL

The element model developed in this study, which consists of a physical idealization of the element and hysteretic rules for flexural and shear force resistance mechanisms, is described below.

6.3.1 Physical Idealization

Figure 6.9 presents the physical model of R/C beams used in this study. In this model, all the shear and flexural elasto-plastic deformations under seismic forces are assumed to be concentrated at dimensionless end springs. In order to differentiate between the hysteretic rules of shear and flexure, distinct springs representing each of these types of behavior are attached to the beam. The behavior of each spring is defined by a skeleton curve and a set of hysteretic rules.

The model shown in Figure 6.9 is a refined version of the single-component model. It is practical (economical), because it involves limited number of degrees of freedom. A comprehensive review of the literatures also indicates that its accuracy in predicting the flexural response is comparable to that of the more complex ones like the multiple spring model (Figure 6.5d) and the single component model with distributed inelasticies (Figure 6.5e). The key advantage of the model proposed in Figure 6.9 is, of course, its capacity to account for the distinct hysteretic characteristics of shear and flexural deformations which leads to major

improvements in its accuracy as the shear deformations tend to dominate the behavior in later inelastic load cycles.

6.3.2 Hysteretic Rules of Flexure and Shear

In order to form the tangent stiffness matrix of the element model presented in Figure 6.9, the tangent stiffness of each of the springs needs to be derived (using its force-deformation relationship) as a function of the level and history of loading. In the following, first a general set of hysteresis rules capable of simulting a variety of hysteresis characteristics (by proper selection of the variables involved) are introduced. Then the hysteretic parameters for flexural and shear types of behavior, which have been derived empirically, are presented. In this presentation, the spring forces (F) might be flexural or shear force, depending on the type of the spring, and the spring deformation (X) might be flexural rotation or shear deformation. The cyclic force-deformation model presented below consists of a skeleton curve and a set of hysteresis rules.

A bilinear curve (Figure 6.10) has been selected in this study, mainly due to the fact that the more complex trilinear and cuvilinear ones do not significantly improve the accuracy of the model[8,32,49]. The initial loading takes place linearly with the stiffness K_i up to the yield force F_y, at deformation X_y. Thereafter the stiffness drops to a strain hardening value of K_h.

Unloading before yielding takes place on the loading curve (with a stiffness equal to K_i). In the post-yield region, the unloading stiffness (K_u) will be decided using the parameter α (see Figure 6.10). This parameter should be derived empirically for each spring type.

The rule for reloading towards the skeleton curve in the opposite direction is illustrated in Figure 6.11. The point on the skeleton curve (R) towards which the reloading occurs is defined by a parameter β that can have any value greater than zero.

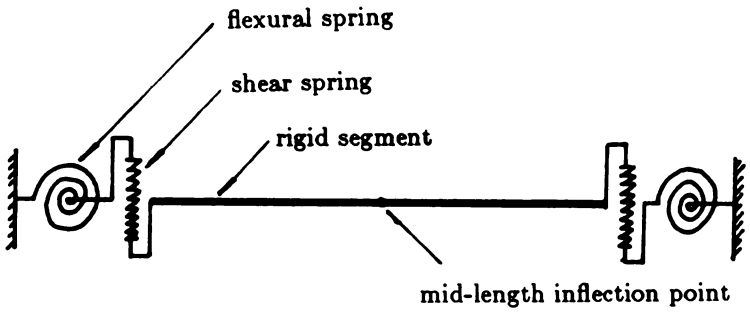

Figure 6.9 Proposed Physical Idealization of Element

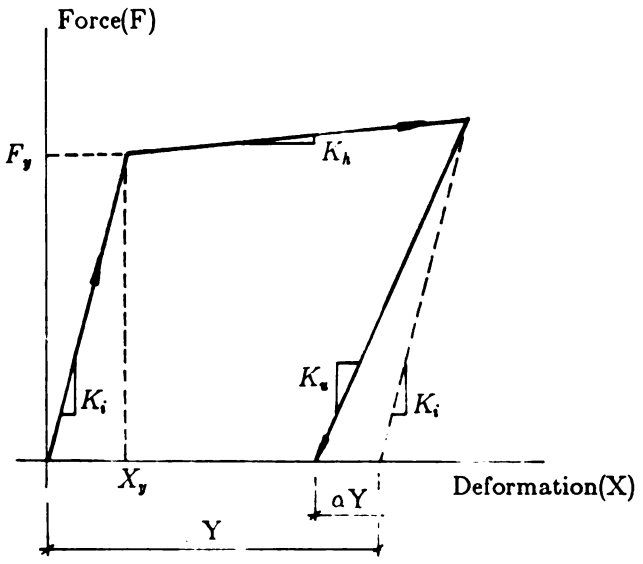

Figure 6.10 Skeleton Curve and Unloading from The Skeleton Curve

The basic reloading rules presented in Figure 6.11 have to be refined to account for the pinching effect which is dominant in shear behavior and the Bauschinger effect displayed especially by the flexural behavior. For this purpose, a line is specified which intersects the horizontal (deformation) axis at the same point as the strain hardening portion of the skeleton curve, and its slope is a fraction (ς) of the skeleton curve hardening stiffness (see Figure 6.12). Another hysteretic parameter γ, that is between -1.0 and 1.0, defines the degree to which the actual reloading path deviates from a straight line. A positive value of γ (Figure 6.12a) is indicative of the Bauschinger effect, while a negative value (Figure 6.12b) leads to the pinching of the reloading path.

The majority of load cycles sustained by a structural element during a seismic event have deformation amplitudes within the bound of previous maximum and minimum deformations. Upon a small-amplitude load reversal, if the reloading takes place towards the skeleton curve (indicating a large-amplitude reversal from the skeleton curve in the previous half-cycle), the path shown in Figure 6.13 will be followed. If reloading is in a direction with the previous load reversal being incomplete, the reloading would take place towards the peak point of the incomplete cycle. This reloading path will involve pinching and bowing if the incomplete cycle peak is above the line with slope ς discussed earlier (Figure 6.14a). Otherwise, it will simply be a straight line from the horizontal axis to the peak of the previous incomplete cycle (Figure 6.14b).

It should be noted that the small amplitude rules apply as far as the cyclic deformations are within the previous maximum and minimum values. If any of these limits are exceeded, the regular large-amplitude rules will be effective again.

The suggested hysteretic rules are quite versatile and, depending on the values of their parameters, they can represent a wide variety of hysteretic characteristics as shown in Figure 6.15.

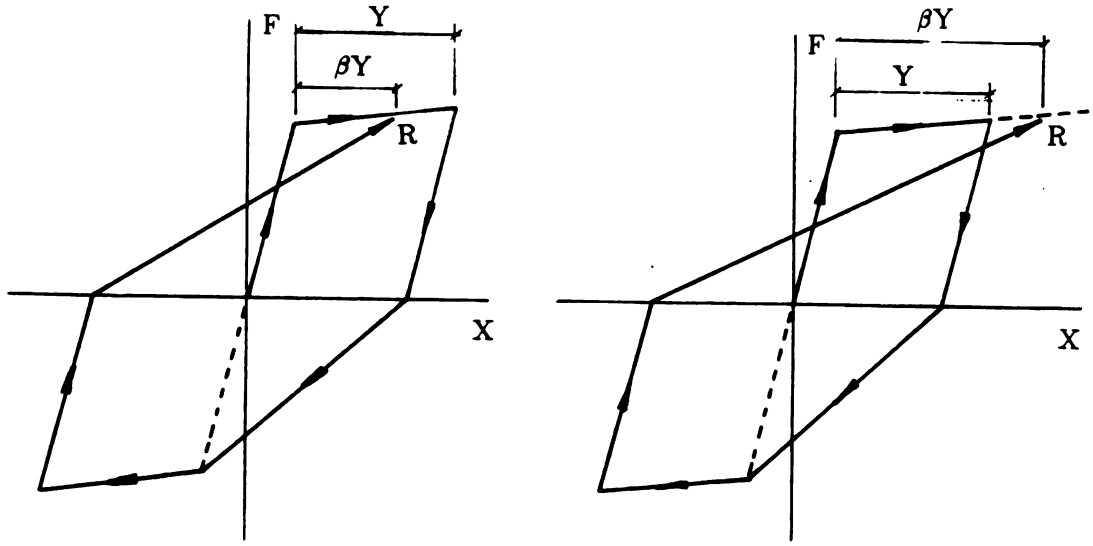

(a) $0.0 \leq \beta \leq 1.0$ (b) $1.0 \leq \beta$

Figure 6.11 Reloading towards The Skeleton Curve

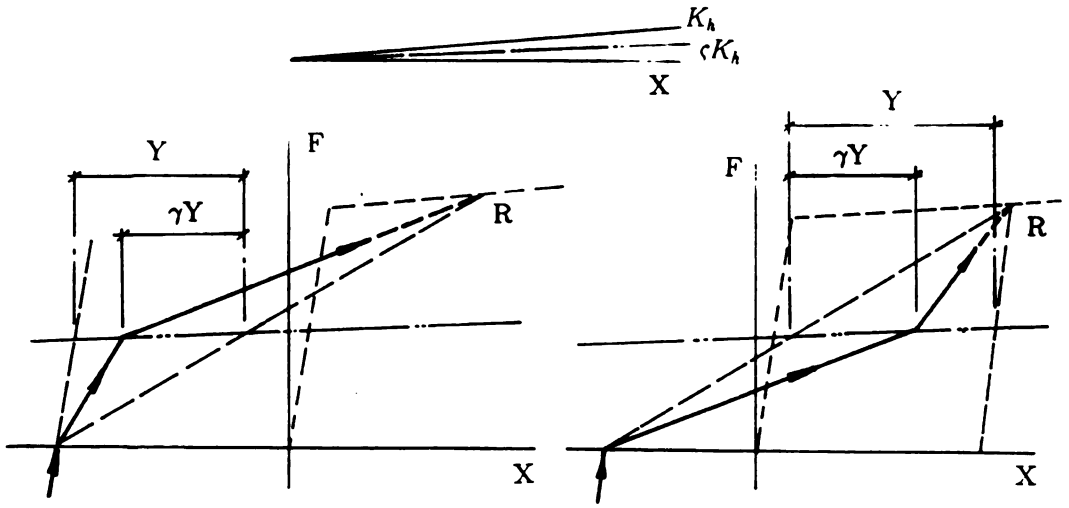

(a) $0.0 \leq \gamma \leq 1.0$ (b) $-1.0 \leq \gamma \leq 0.0$

Figure 6.12 The Bauschinger and Pinching Effect on The Reloading Path

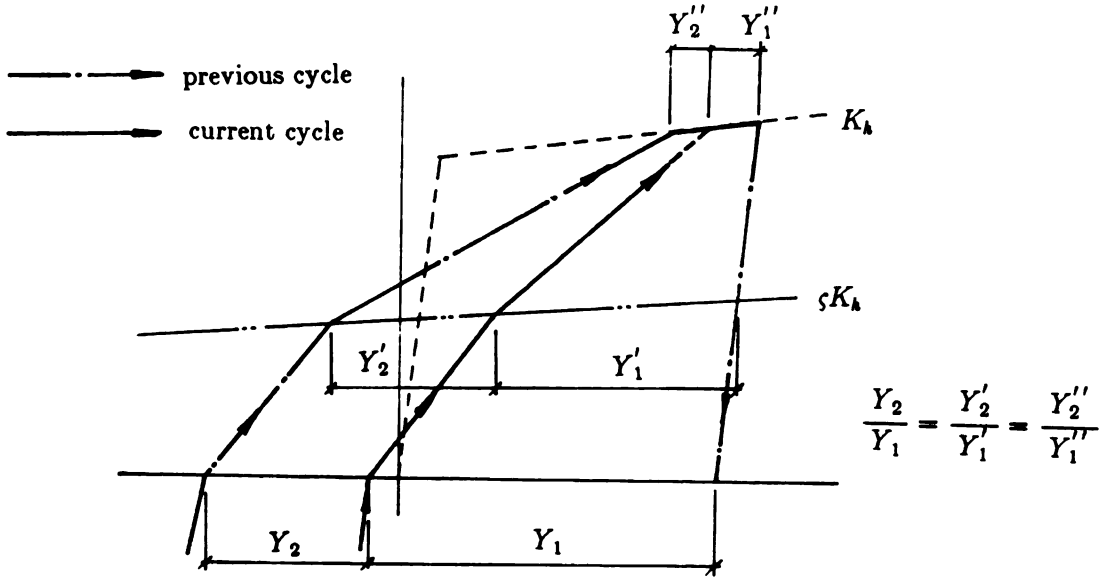

Figure 6.13 Small-Amplitude Reloading towards The Skeleton Curve

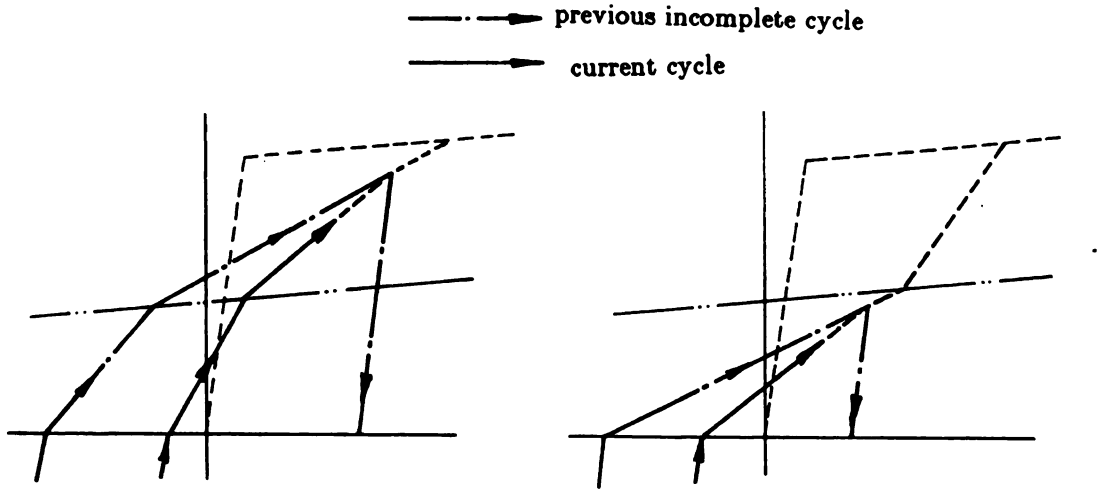

(a) Case 1 (b) Case 2

Figure 6.14 Small-Amplitude Reloading in A Direction with Previous Incompete Cycle

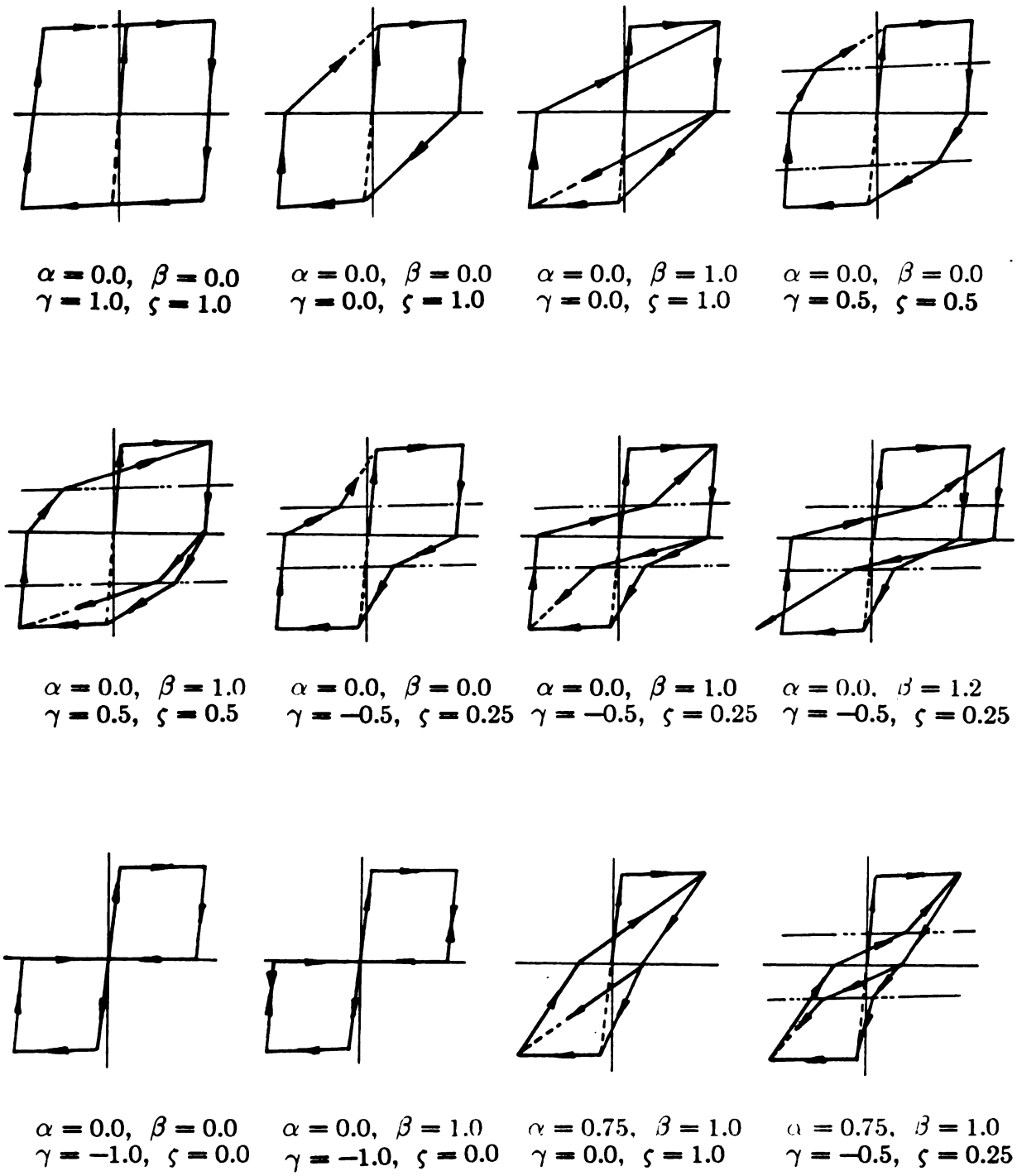

Figure 6.15 Different Hysteresis Diagrams Formed By Varing Their Parameters of The Proposed Hysteretic Model

6.3.3 Selection of The Hysteretic Parameters

In order to complete the hysteretic simulation of the flexural and shear springs in the proposed element model, the yield force, the initial and strain hardening stiffnesses and the hysteretic parameters (α, β, γ, and ς) of these springs have to be determined. The empirical values of these variables or the analytical methods for calculating them are presented below.

Yielding of the flexural and shear springs in Figure 6.9 is assumed to occur simultaneously when the bending moment in the flexural spring reaches the flexural yield strength of the R/C cross section. The reported test data of R/C beams support this assumption. The yield moment in flexure can be derived using the simplified strain and stress distributions presented in Figure 6.16. At the yield point, the concrete stress distribution across the section is assumed to be linear, and yielding of the tension steel is assumed to mark the yield point. The depth of neutral axis in Figure 6.16 can be obtained from the equilibrium of axial forces, and then the yield moment of the cross section can be derived. The force in the shear spring at yielding of the flexural spring is assumed to be the yield shear force. For unsymmetric sections, the yield values of shear force and bending moment should be calculated for both loading directions.

The initial flexural and shear stiffnesses of the springs are based on the moment of inertia and the area of the cracked transformed cross section (Figure 6.17), using the conventional elastic formulations.

It should be mentioned that in calculating both the yield and initial stiffnesses of the flexural and shear springs, it is assumed that the inflection point of the element under seismic forces is at the element mid-length (Figure 6.19). Hence, the shear spring force is always equal to the flexural spring bending moment devided by half the element length, and the initial stiffnesses of the flexural and shear springs at each end represent the elastic flexural and shear

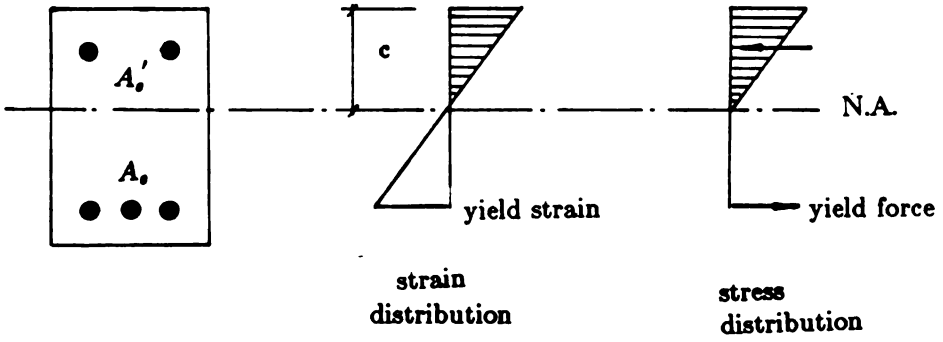

Figure 6.16 Simplified Flexural Strain and Stress Distributions at Yielding

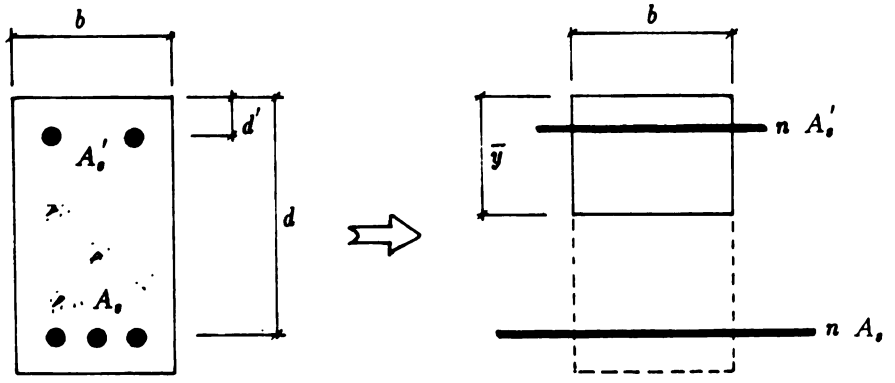

Figure 6.17 Cracked Transformed Cross Section for Calculating The Initial Flexural and Shear stiffnesses

stiffnesses of half the element (treated as a cantilever beam with a cracked trasformed cross section). The variations in inflection point location under seismic forces has been observed to have relatively small effects on the element response characteristics[39], and the assumption of a fixed inflection point at mid-length seems to be warranted.

The strain hardening ratio (the strain hardening stiffness over the initial stiffness) and the hysteretic parameters of the flexural and shear springs were derived empirically using the test data presented in References 6-8, 28, 37, 45 and 46. All these references have reported the results of cyclic tests on R/C beams with separate measurements of the flexural and shear deformations. The test techniques used in these refernces have eliminated, to a large extent, the deformations associated with the fixed-end rotation. Table 6.1 presents the values of these vaiables for the flexural and shear springs (see Figure 6.18).

Table 6.1 Empirical Values of The Strain Hardening Ratio and Hysteretic Parameters of The Flexural and Shear Springs

Spring Type	Strain Hardening Ratio	α	β	γ	ς
Flexural	0.021	0.16	0.97	0.42	0.75
Shear	0.043	0.11	1.22	-0.49	0.29

6.4 FORMULATION OF THE ELEMENT TANGENT STIFFNESS MATRIX

The hysteretic models of the flexural and shear springs in the proposed element model (Figure 6.9) can be used to derive the tangent stiffnesses of these springs at any step in the loading history. These stiffnesses can be used in constructing the overall tangent stiffness matrix of the element. In the following, the

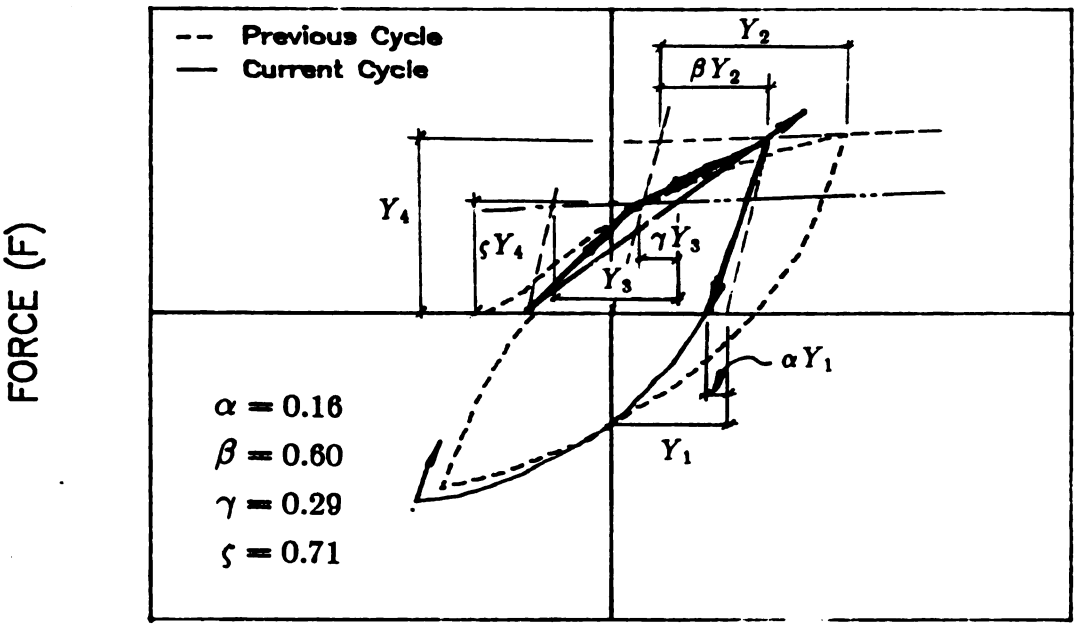

(a) Flexural Spring

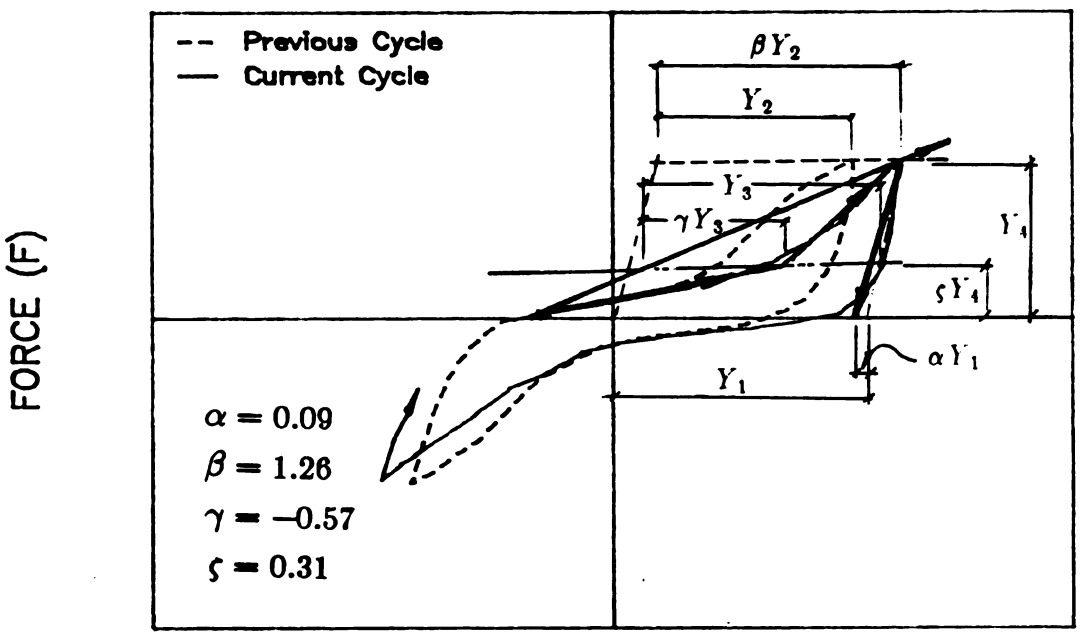

(b) Shear Spring

Figure 6.18 Empirical Values of The Strain Hardening Ratio and Hysteretic Parameters of The Flexural and Shear Springs

tangent stiffness matrices for cantilever beams (commonly used in experimental studies) and a general beam element (for incorporation in the overall structural analysis programs) will be developed.

The cantilever beam (Figure 6.20) has only one degree of freedom, that is the lateral displacement (δ) at the free end of the element. This displacement results from the shear deformation of the shear spring and rotation of the flexural spring:

$$\begin{aligned} d\delta &= d\delta_s + l \cdot d\theta_f \\ &= \frac{dV}{K_s} + \frac{dV \cdot l}{K_f} \\ &= dV\left(\frac{1}{K_s} + \frac{l}{K_f}\right) \end{aligned} \tag{6.1}$$

where,

$d\delta$ = incremental displacement at free end ;
$d\delta_s$ = shear spring incremental deformation ;
$d\theta_f$ = flexural spring incremental rotation ;
dV = incremental lateral load at free end ;
l = cantilever element length ;
K_s = shear spring tangent stiffness ;
K_f = flexural spring tangent stiffness.

Hence, the tangent stiffness (K_t) of cantilever element shown in Figure 6.8 can be derived from the following expression:

$$\begin{aligned} dV &= K_t \cdot d\delta \\ &= \left(\frac{1}{\frac{1}{K_s} + \frac{l}{K_f}}\right) d\delta \end{aligned} \tag{6.2}$$

In a general beam element, there are six displacement degrees of freedom (r_{xi}, r_{yi}, $r_{\theta i}$, r_{xj}, r_{yj}, and $r_{\theta j}$), shown in Figure 6.21(a). These six degrees of freedom may be condensed to the rotation at each end of the element (θ_i, θ_j) and the change in element length ΔL, as shown in Fig. 6.21(b). The beam axis will be

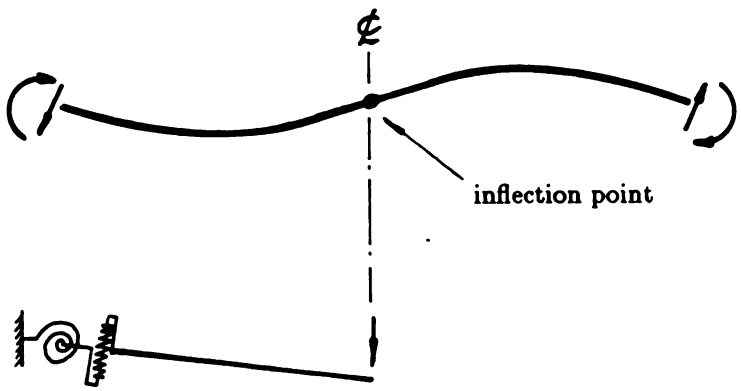

Figure 6.19 Mid-Length Inflection Point under Seismic Forces

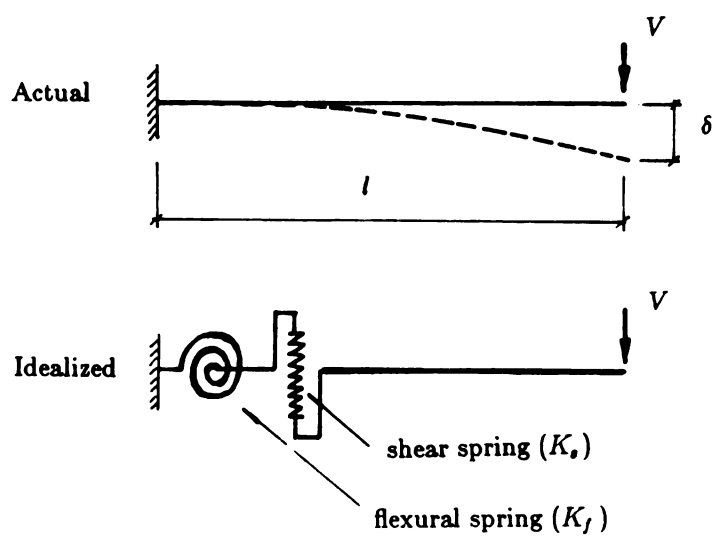

Figure 6.20 Cantilever Element

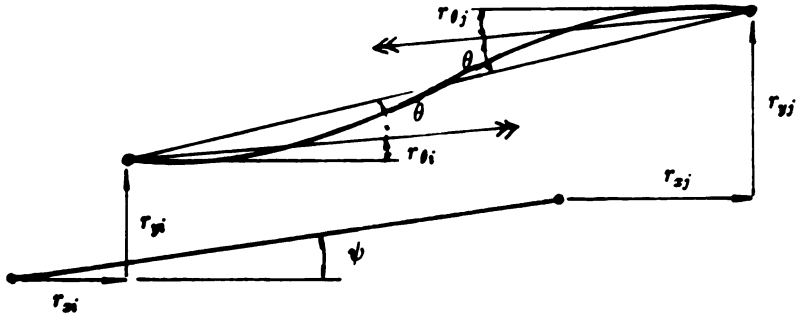

(a) Six Degrees of Freedom

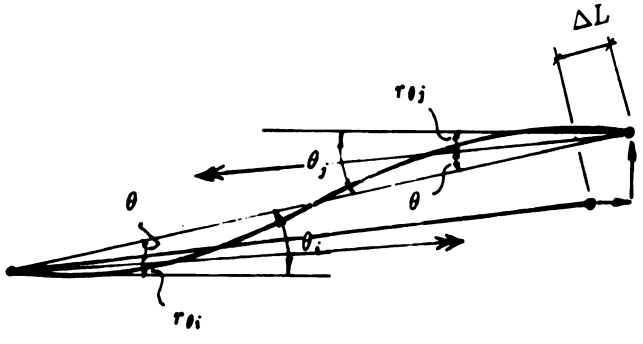

(b) Condensed Degrees of Freedom

Figure 6.21 Displacement Degrees of Freedom in A Genaral Beam Element

rotated due to the end translation by an amount θ, and it will be

$$\theta = \left[(r_{yj} - r_{yi})\cos\psi - (r_{xj} - r_{xi})\sin\psi\right]/L \tag{6.3}$$

where,

ψ = element orientation angle;
L = total element length.

Hence, the total rotation of each end of the element will be

$$\begin{aligned}\theta_i &= \theta + r_{\theta i}\\ \theta_j &= \theta + r_{\theta j}\end{aligned} \tag{6.4}$$

The change in element length is given by

$$\Delta L = (r_{xj} - r_{xi})\cos\psi + (r_{yj} - r_{yi})\sin\psi \tag{6.5}$$

Deformations of the element degrees of freedom are correlated with the shear and rotational deformations in the shear and flexural springs, respectively. Incremental deformations in the shear springs change the element rotation ($d\theta_s$) by:

$$d\theta_s = \frac{dV}{K_s \cdot L} \tag{6.6}$$

where,

dV = incremental shear force at element ends
$= \left(\dfrac{dM_i + dM_j}{L}\right)$;
dM_i = incremental moment at end i ;
dM_j = incremental moment at end j ;
L = total element length ;
$K_s = \dfrac{1}{1/K_{si} + 1/K_{sj}}$;
K_{si} = tangent stiffness of shear spring at end i ;
K_{sj} = tangent stiffness of shear spring at end j.

The incremental element end rotations caused by the flexural spring rotations ($d\theta_{fi}$ and d θ_{fj}) are given by:

$$d\theta_{fi} = \frac{dM_i}{K_{fi}}$$
$$d\theta_{fj} = \frac{dM_j}{K_{fj}} \tag{6.7}$$

Adding the shear and flexural components, the total element end rotations can be obtained as follow:

$$\begin{Bmatrix} d\theta_i \\ d\theta_j \end{Bmatrix} = \begin{Bmatrix} d\theta_s + d\theta_{fi} \\ d\theta_s + d\theta_{fj} \end{Bmatrix}$$
$$= \begin{bmatrix} \frac{1}{K_s L^2} + \frac{1}{K_{fi}} & \frac{1}{K_s L^2} \\ \frac{1}{K_s L^2} & \frac{1}{K_s L^2} + \frac{1}{K_{fj}} \end{bmatrix} \begin{Bmatrix} dM_i \\ dM_j \end{Bmatrix} \tag{6.8}$$

Hence, the element tangent stiffness matrix (K) is,

$$K = \begin{bmatrix} \frac{1}{K_s L^2} + \frac{1}{K_{fi}} & \frac{1}{K_s L^2} \\ \frac{1}{K_s L^2} & \frac{1}{K_s L^2} + \frac{1}{K_{fj}} \end{bmatrix}^{-1} \tag{6.9}$$

The element tangent stiffness matrix (K_G) in the global coordinates, for incorperation into the structural stiffness matrix, can be obtained through an appopriate transformation:

$$[K_G] = [T]^T \cdot [K] \cdot [T] \tag{6.10}$$

where, $[T]$ is a transformation matrix which can be obtained from Equations (6.3) and (6.4):

$$T = \begin{array}{c} \begin{matrix} r_{xi} & r_{yi} & r_{\theta i} & r_{xj} & r_{yj} & r_{\theta j} \end{matrix} \\ \begin{bmatrix} -\frac{\sin\psi}{L} & \frac{\cos\psi}{L} & 1 & \frac{\sin\psi}{L} & -\frac{\cos\psi}{L} & 0 \\ -\frac{\sin\psi}{L} & \frac{\cos\psi}{L} & 0 & \frac{\sin\psi}{L} & -\frac{\cos\psi}{L} & 1 \end{bmatrix} \end{array}; \tag{6.11}$$

In Equation (6.10), $[T]^T$ is the transpose matrix of $[T]$.

The above element tangent stiffness matrix can be used to construct the overall tangent stiffness matrix of complete structural systems for performing incremental nonlinear static and dynamic analysis of structures.

6.5 COMPARISON WITH TEST RESULTS

A large number of cyclic test data on R/C cantilever beams have been reported in the literature. This section compares the experimental cyclic load-deformation relationships with the predictions of the developed models. Six tested R/C beams with a variety of geometric and material characteristics were selected for this comparative study. Some major properties of these elements are given in Table 6.2. In this table, l is the element length, l/d is the shear span to depth ratio, b is the (rectangular) cross sectional width, ρ and ρ' are the ratios of bottom and top reinfocements, and ρ_s is the volumetric ratio of transverse reinfocement at the critical location near the fixed end, and f_c' and f_y are the concrete compressive strength and steel yield strength, respectively.

Table 6.2 Properties of R/C Beams Used in Comparison Between The Tests and Theory

Beam No.	$l(in)$	l/d	b	$\rho = \rho'$	ρ_s	$f_c'(ksi)$	$f_y(ksi)$	Ref. No.
1	59	3.1	7.9	0.0178	0.0043	6.11	45.11	51
2	59	3.1	7.9	0.0178	0.0043	5.45	44.38	51
3	59	3.1	7.9	0.0178	0.0043	4.82	45.11	51
4	60	4.7	15.0	0.0103	0.011	4.75	54.4	35
5	60	4.7	15.0	0.0103	0.013	4.06	51.8	35
6	60	4.7	15.0	0.0103	0.020	4.25	51.8	35

Figures 6.22(a) and (b) compare the total cyclic force-deformation relationships obtained experimentally and theoretically, respectively, for the cantilever beam No. 1 (see Table 6.2). The proposed model is observed to be capable of predicting the test results with a reasonable accuracy. Figures 6.22(c) and (d) compare the experimental and theoretical flexural components, and Figures 6.22(e) and (f) compare the experimantal and theoretical shear components of the cyclic deformations. These figures (both experimental and theoretical ones) indicate that shear deformations play an increasingly important role in the element deformations under repeated inelastic load cycles.

Another comparison between the experimental and the theoretical total, flexural, and shear cyclic load-deformation relationships is presented in Figure 6.23 for the beam No. 2 of Table 6.2. Here also the model is observed to satisfactorily predict the test results. It is also interesting to notice that at the relatively large inelastic cycles repeated with the same amplitude (see for example, the last four cycles in Figures 6.23a and b), the flexural end displacements (Figures 6.23c and d) tend to decrease while the shear deformation (Figures 6.23e and f) continue to increase under repeated cycles.

Another comparison between the experimental and theoretical total, flexural and shear load-displacement relationships is given in Figure 6.24. The theoretical results for this beam (No. 3 of Table 6.2) are also observed to compare well with the experimental ones.

Figures 6.25 through 6.27 present comparisons between the experimental and theoretical total cyclic load-displacement relationships for beam Nos. 4, 5 and 6, respectively, of Table 6.2. In all these beams, which have relatively low shear forces compared to beam Nos. 1 to 3, a reasonable comparison can be observed between the experimental and theoretical results.

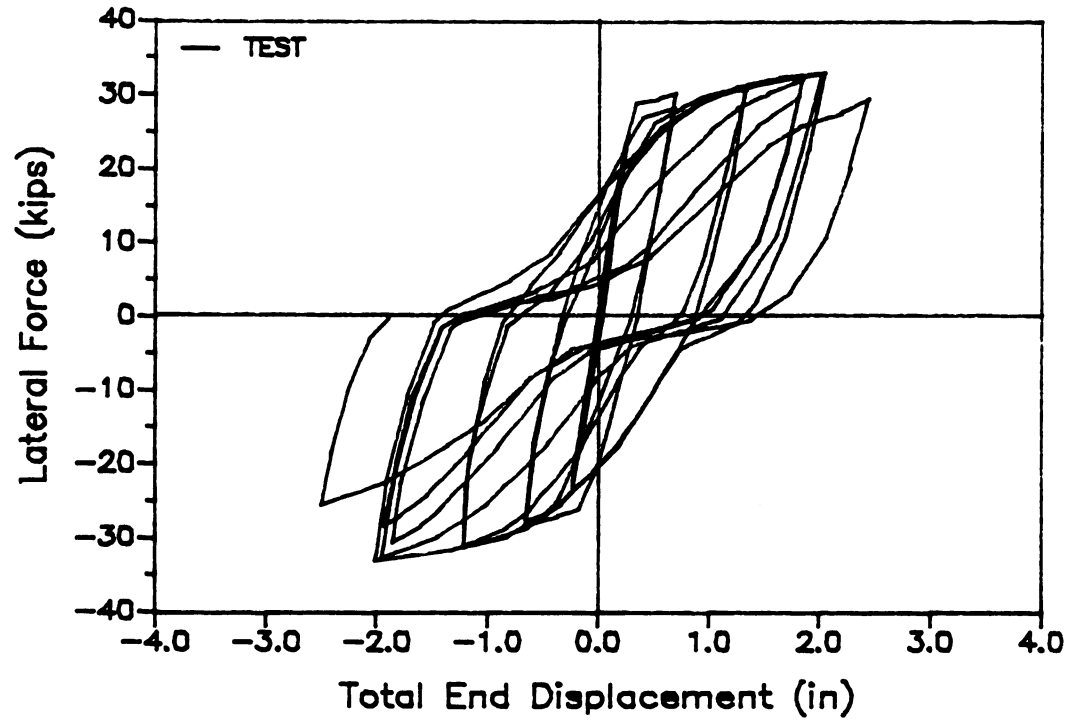

(a) Total Deformation (Experiment)

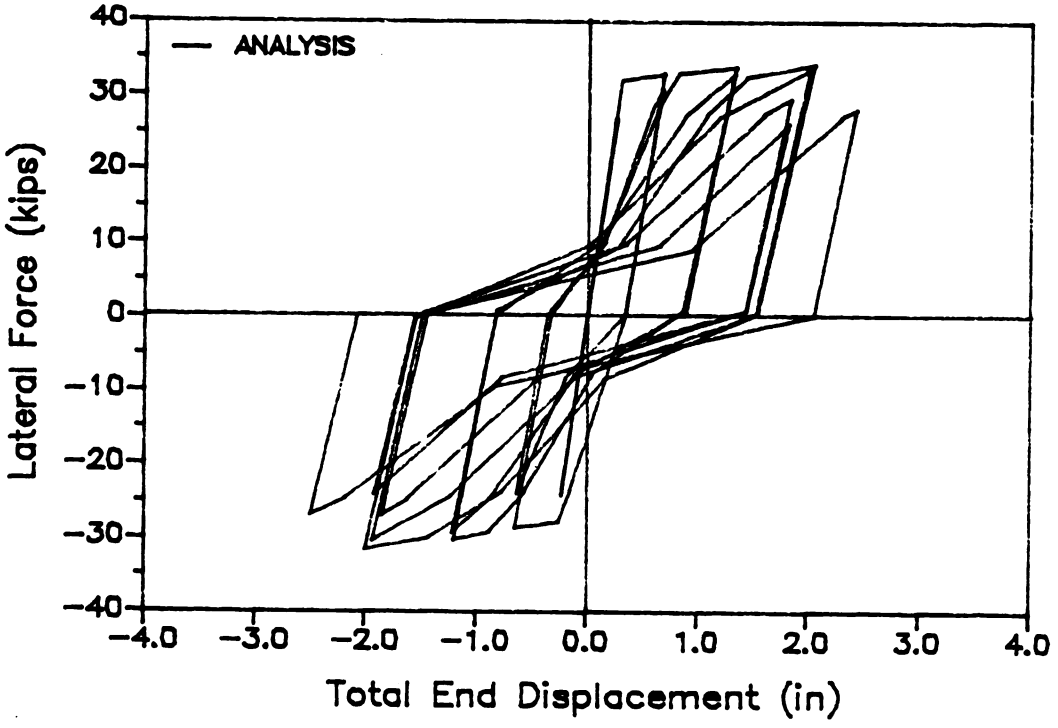

(b) Total Deformation (Theory)

Figure 6.22 Experimental and Theoretical Cyclic Load-Deformation Relationships of Beam No. 1

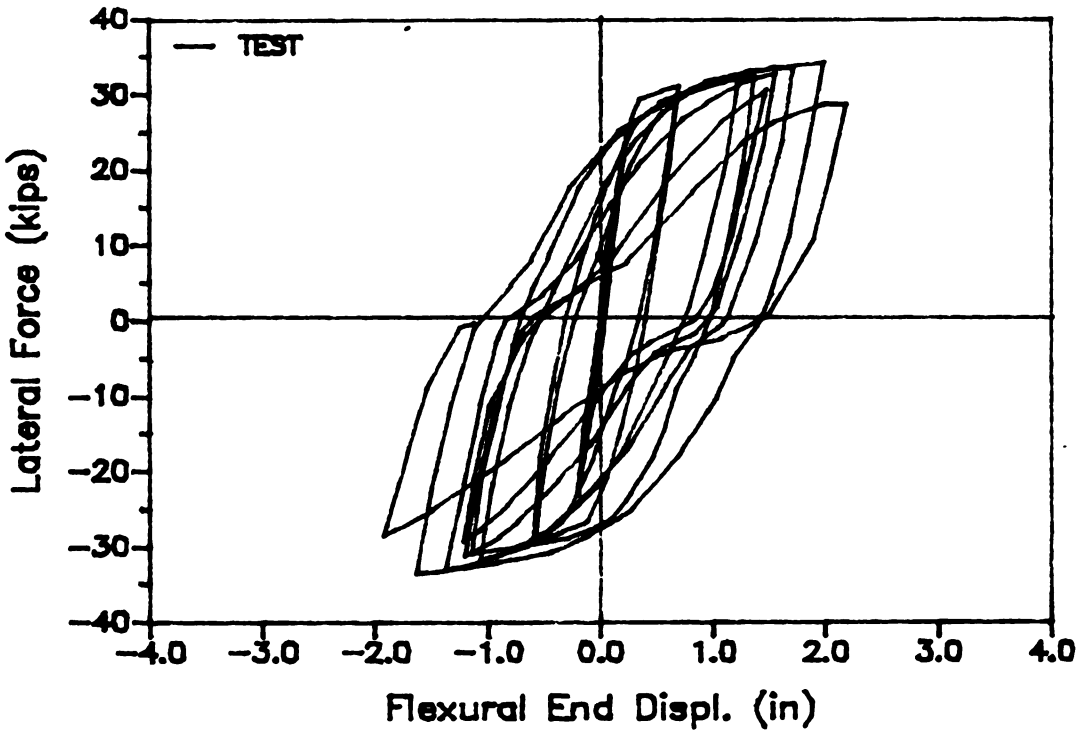

(c) Flexural Deformation (Experiment)

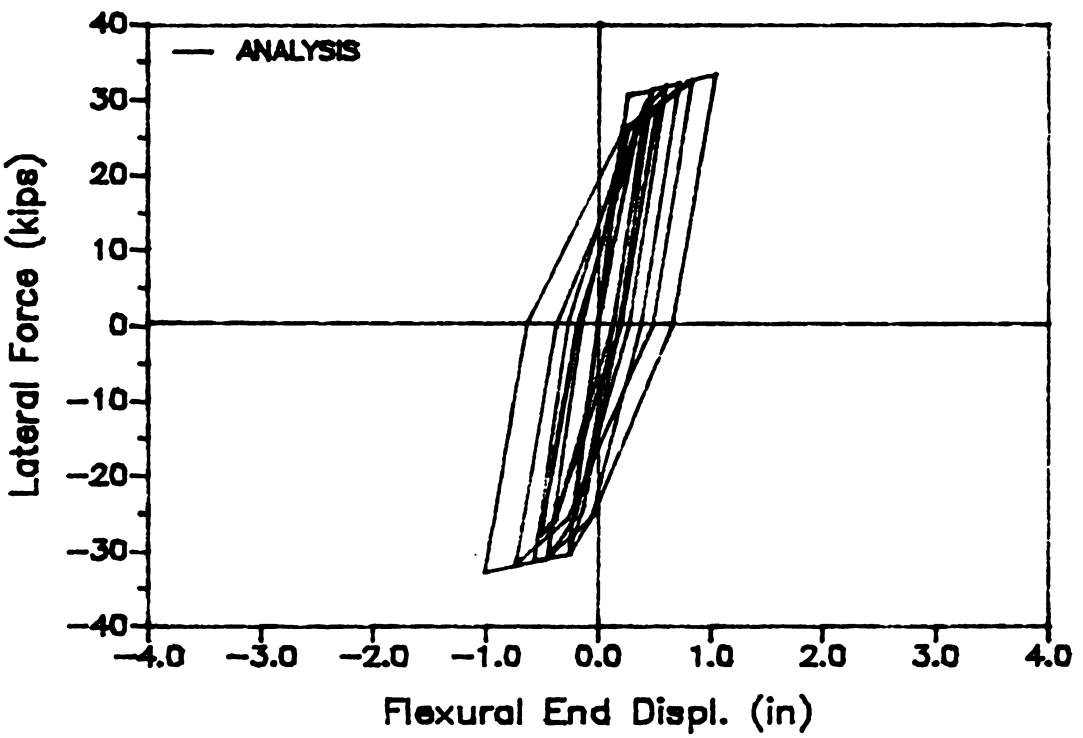

(d) Flexural Deformation (Theory)

Figure 6.22 Experimental and Theoretical Cyclic Load-Deformation Relationships of Beam No. 1(cont'd)

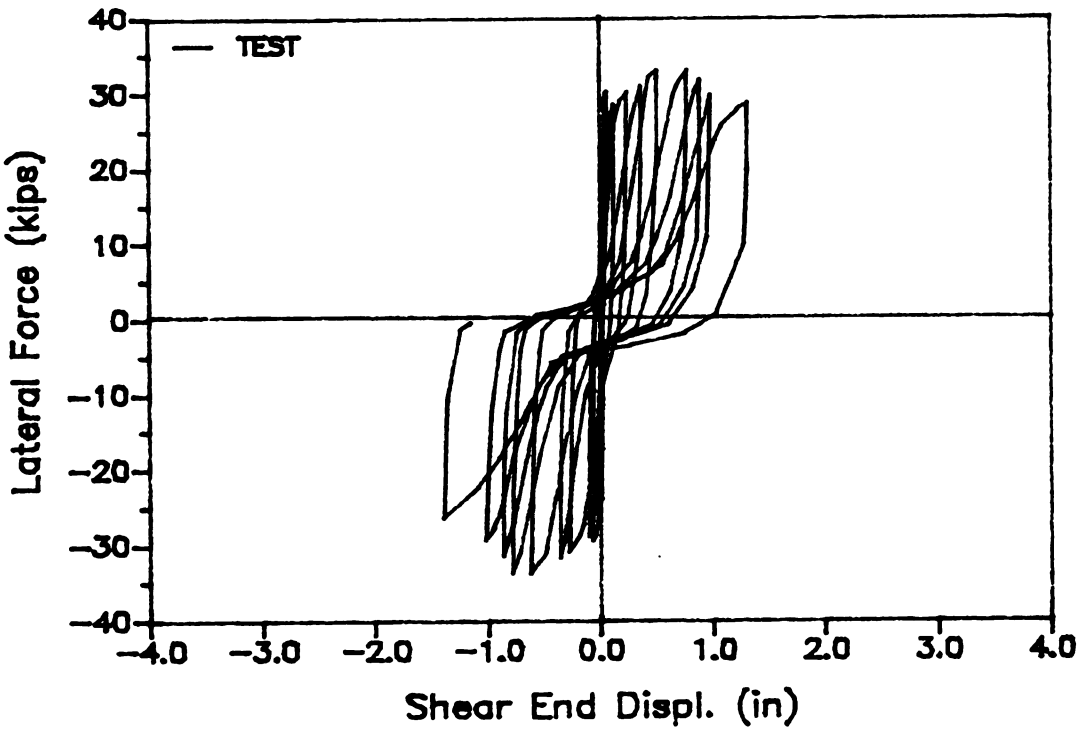

(e) Shear Deformation (Experiment)

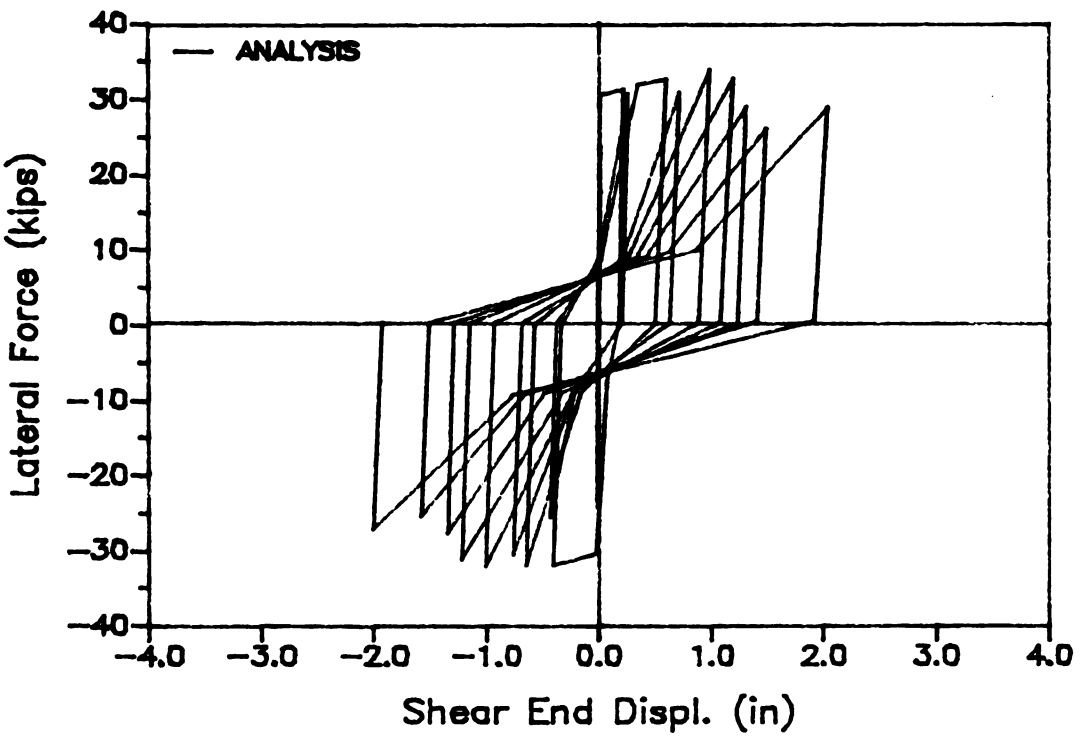

(f) Shear Deformation (Theory)

Figure 6.22 Experimental and Theoretical Cyclic Load-Deformation Relationships of Beam No. 1(cont'd)

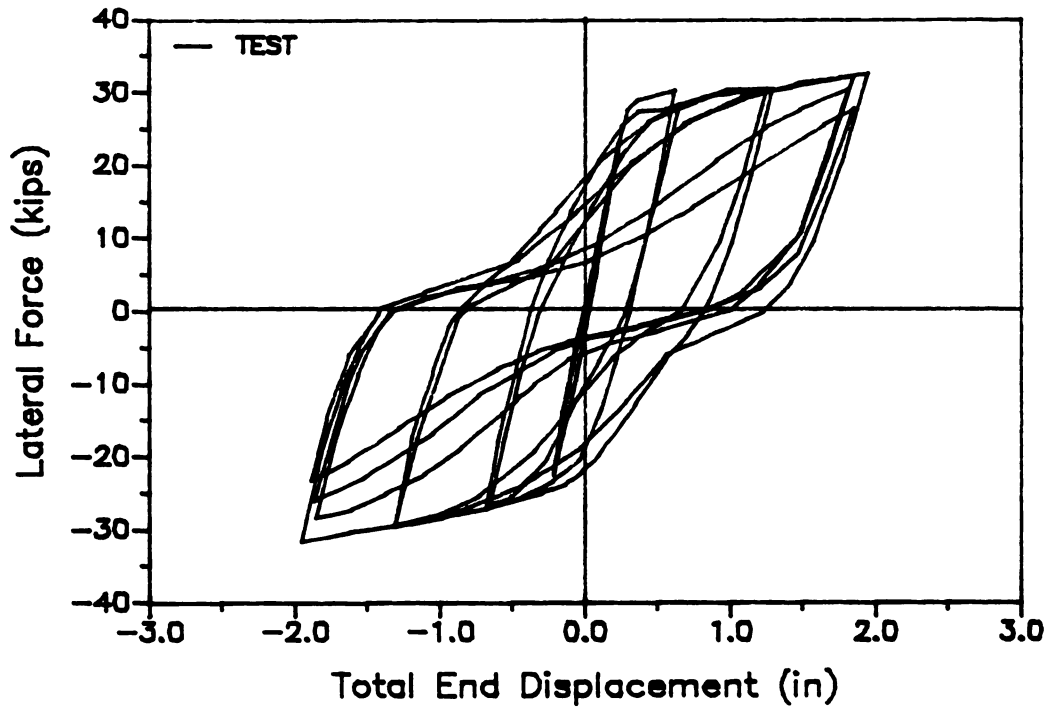

(a) Total Deformation (Experiment)

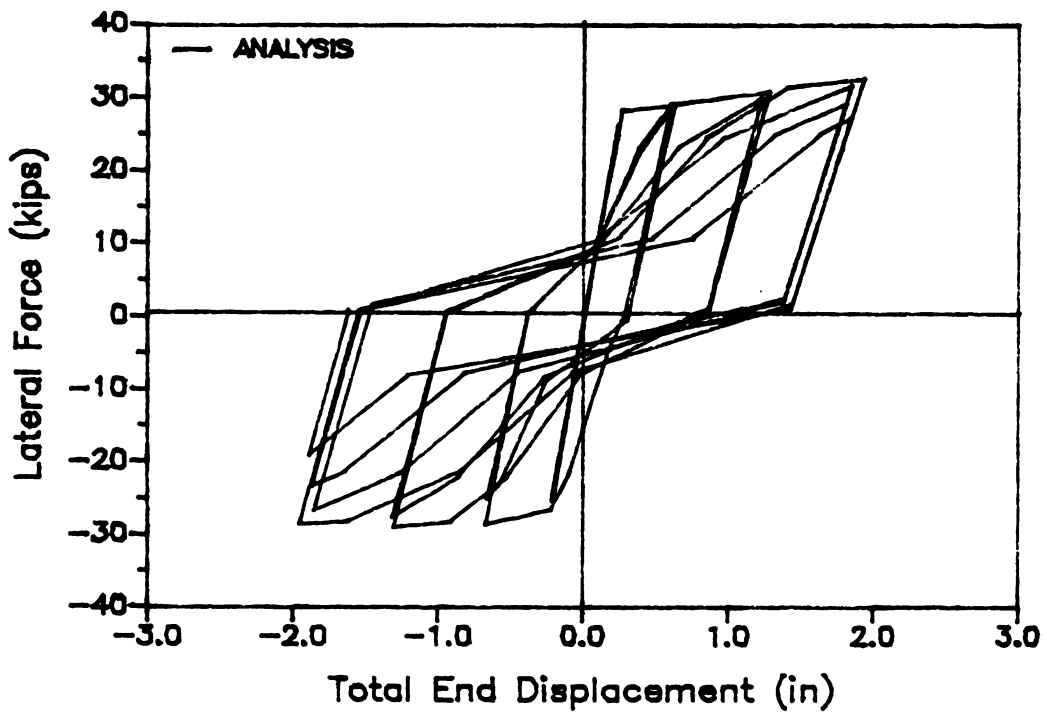

(b) Total Deformation (Theory)

Figure 6.23 Experimental and Theoretical Cyclic Load-Deformation Relationships of Beam No. 2

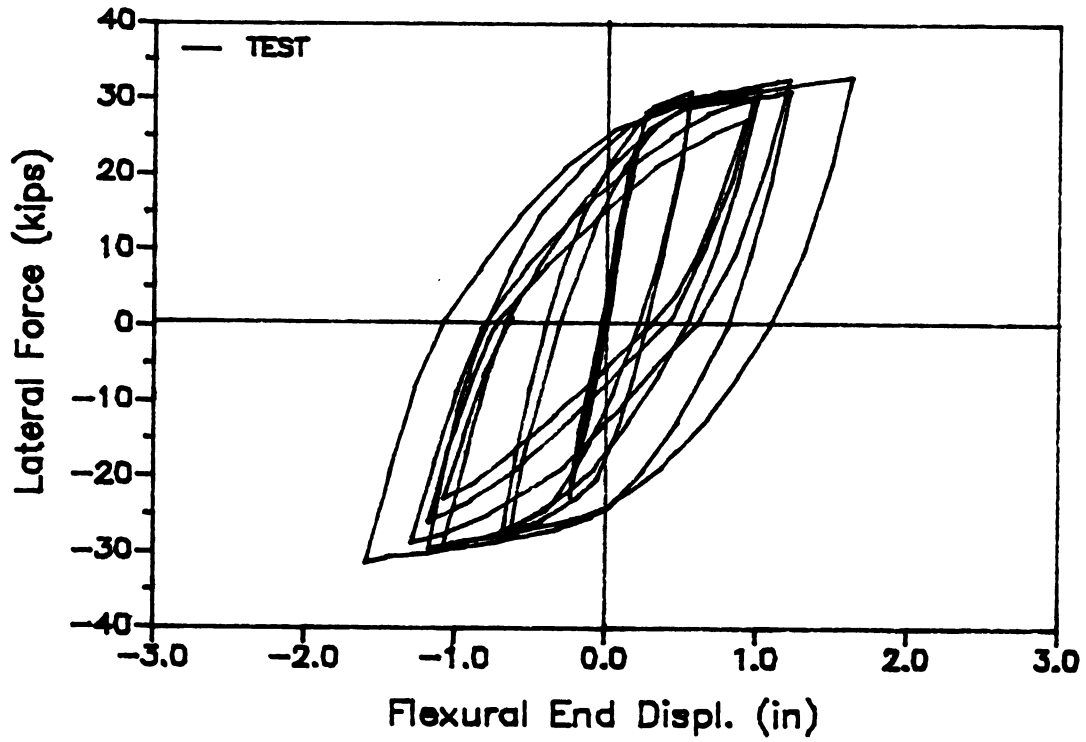

(c) Flexural Deformation (Experiment)

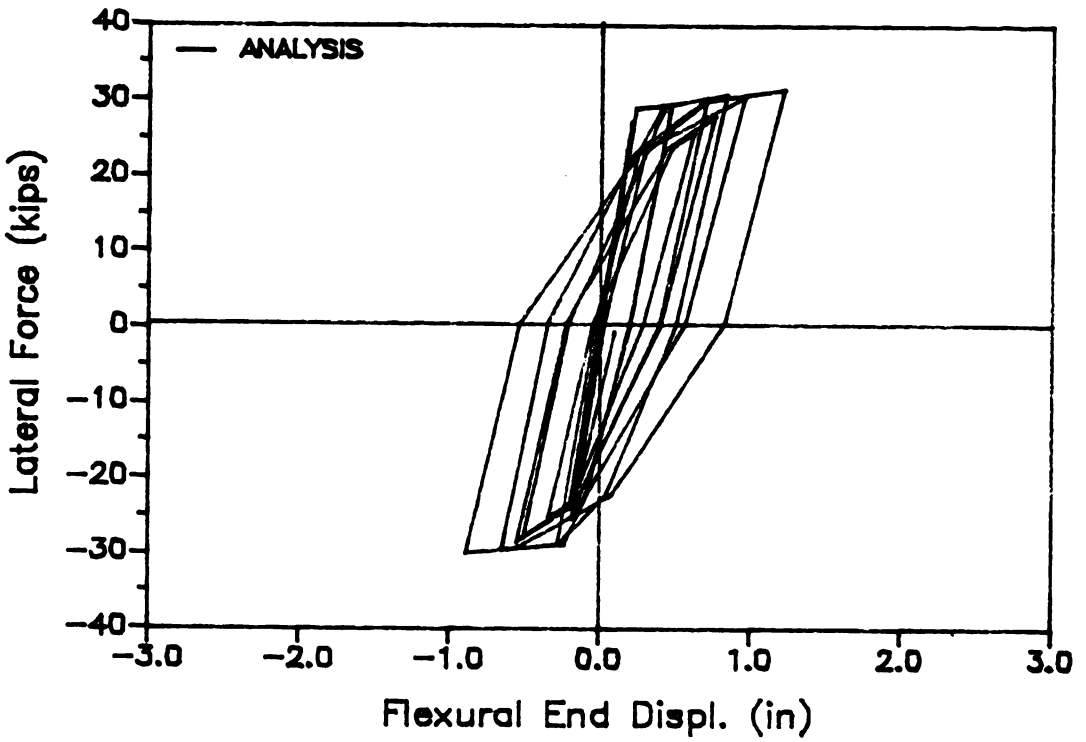

(d) Flexural Deformation (Theory)

Figure 6.23 Experimental and Theoretical Cyclic Load-Deformation Relationships of Beam No. 2(cont'd)

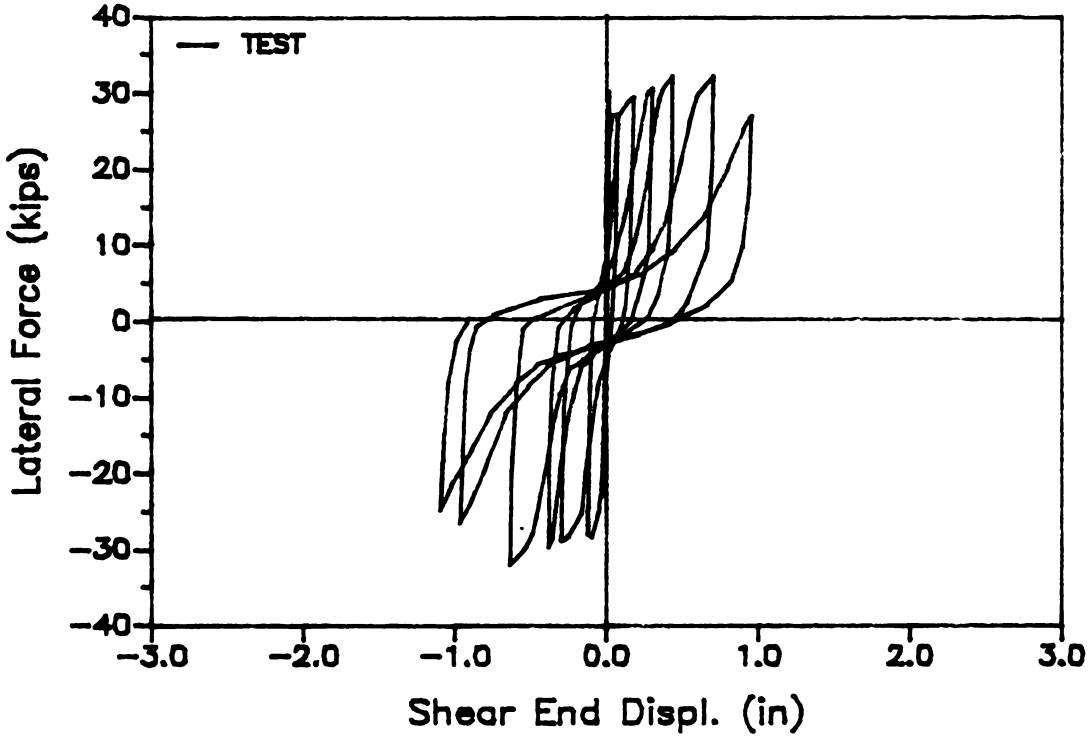

(e) Shear Deformation (Experiment)

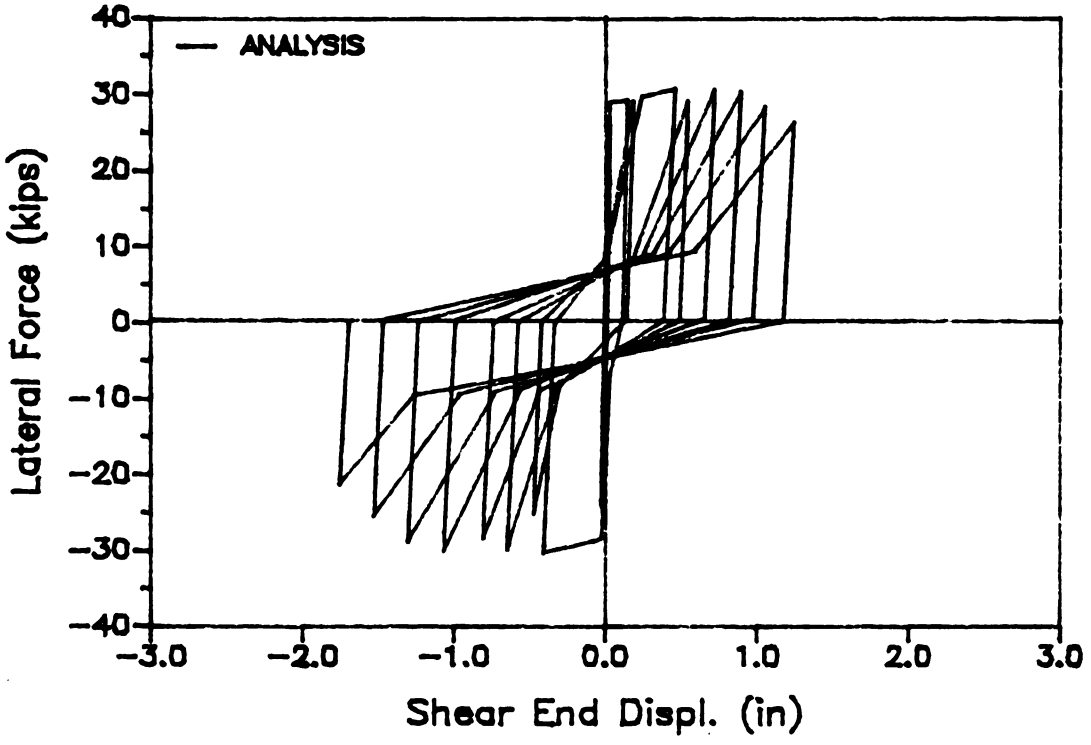

(f) Shear Deformation (Theory)

Figure 6.23 Experimental and Theoretical Cyclic Load-Deformation Relationships of Beam No. 2(cont'd)

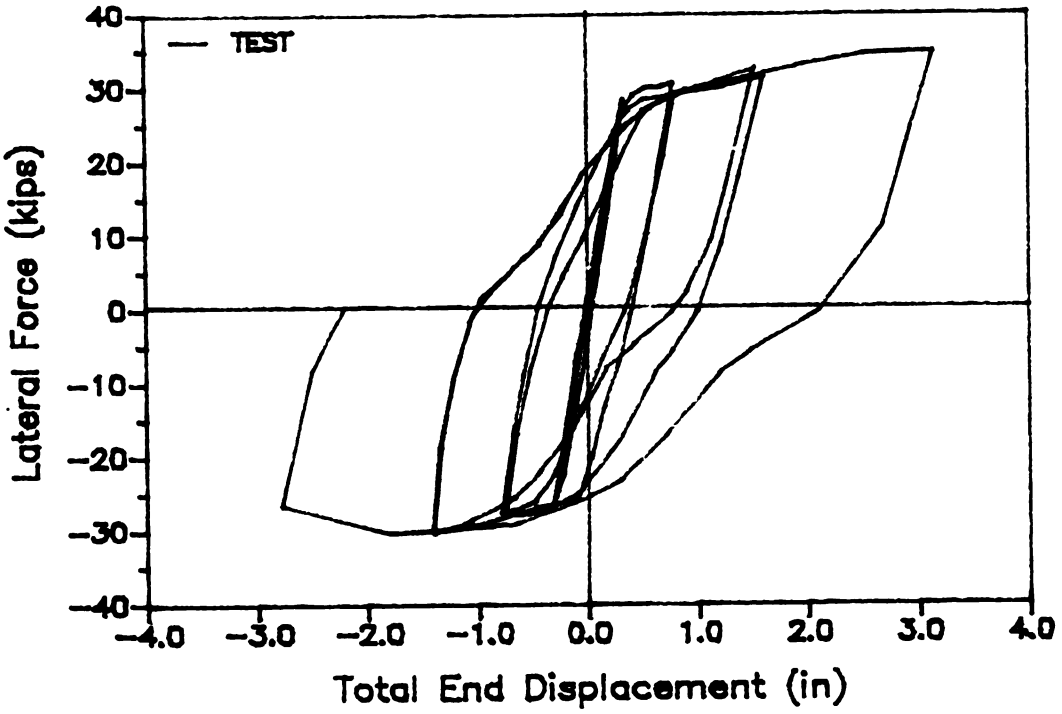

(a) Total Deformation (Experiment)

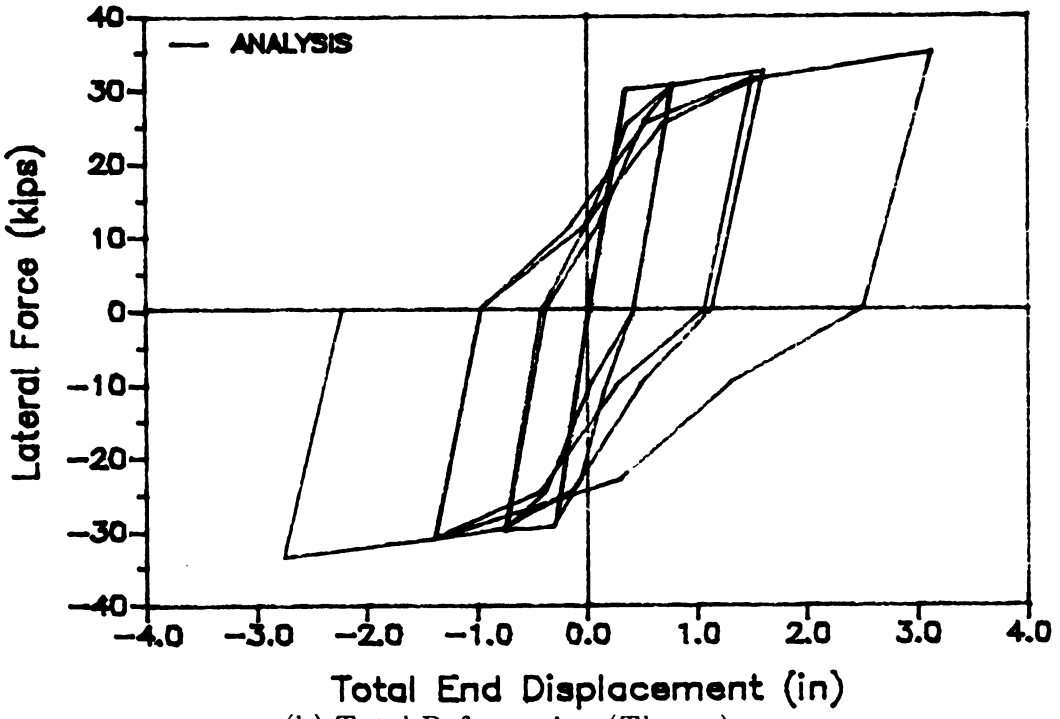

(b) Total Deformation (Theory)

Figure 6.24 Experimental and Theoretical Cyclic Load-Deformation Relationships of Beam No. 3

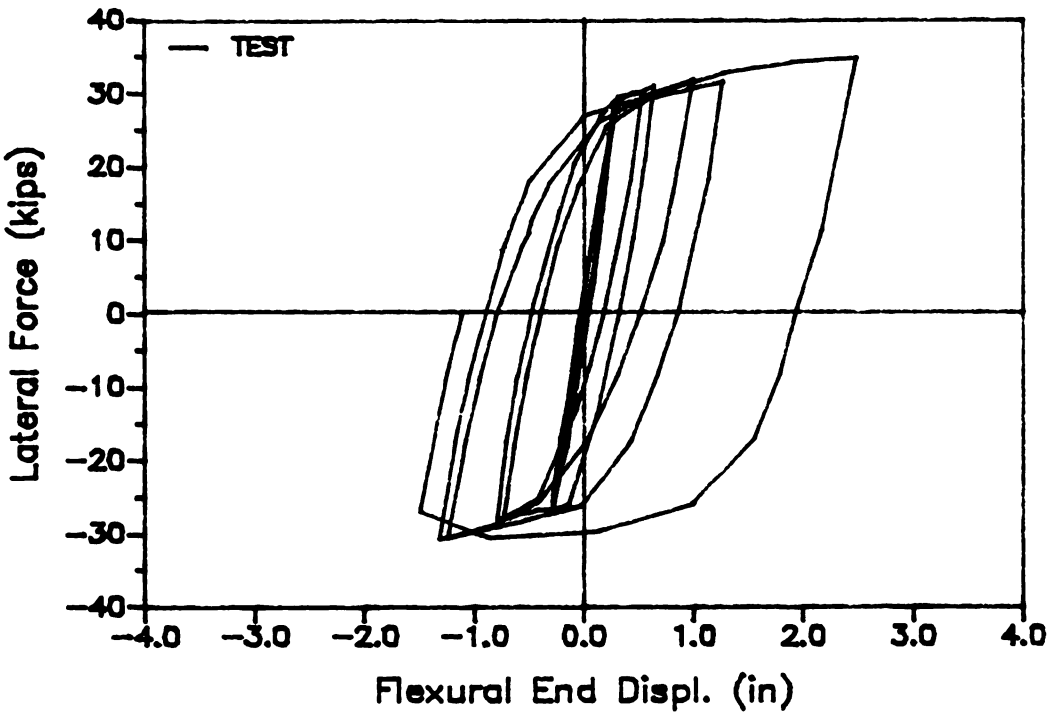

(c) Flexural Deformation (Experiment)

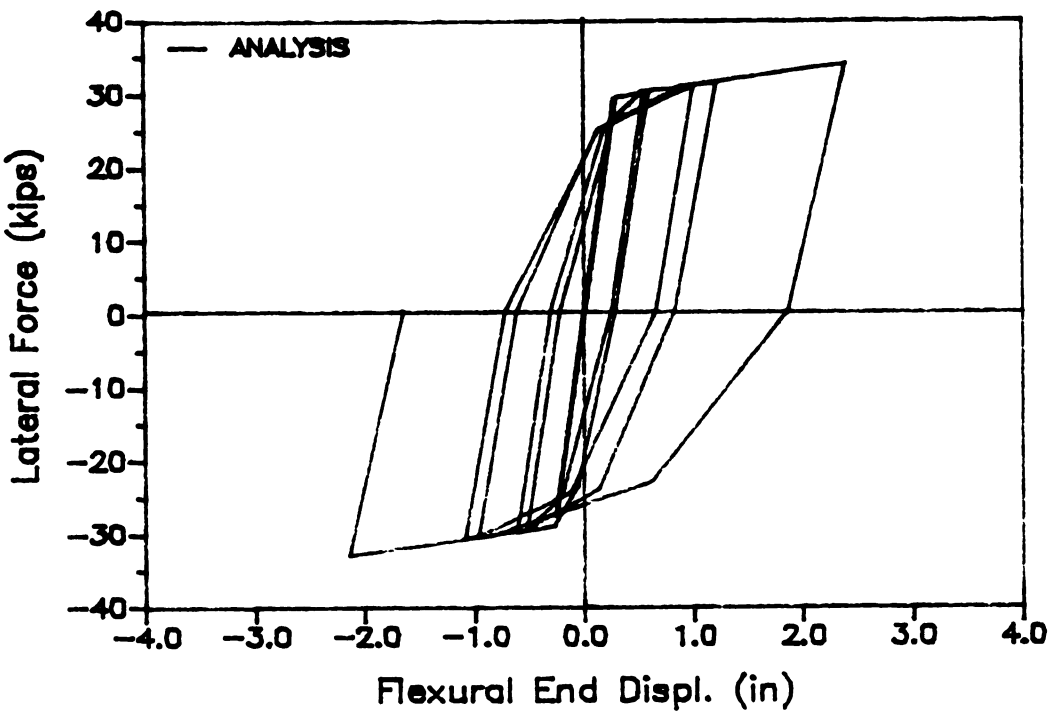

(d) Flexural Deformation (Theory)

Figure 6.24 Experimental and Theoretical Cyclic Load-Deformation Relationships of Beam No. 3(cont'd)

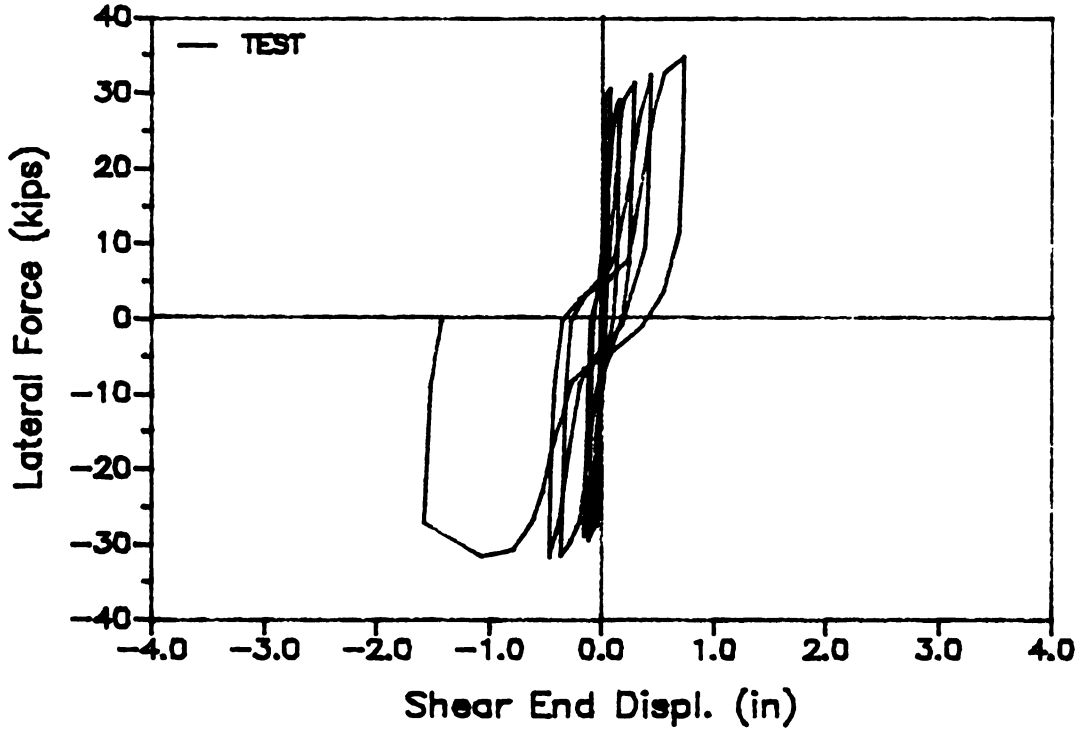

(e) Shear Deformation (Experiment)

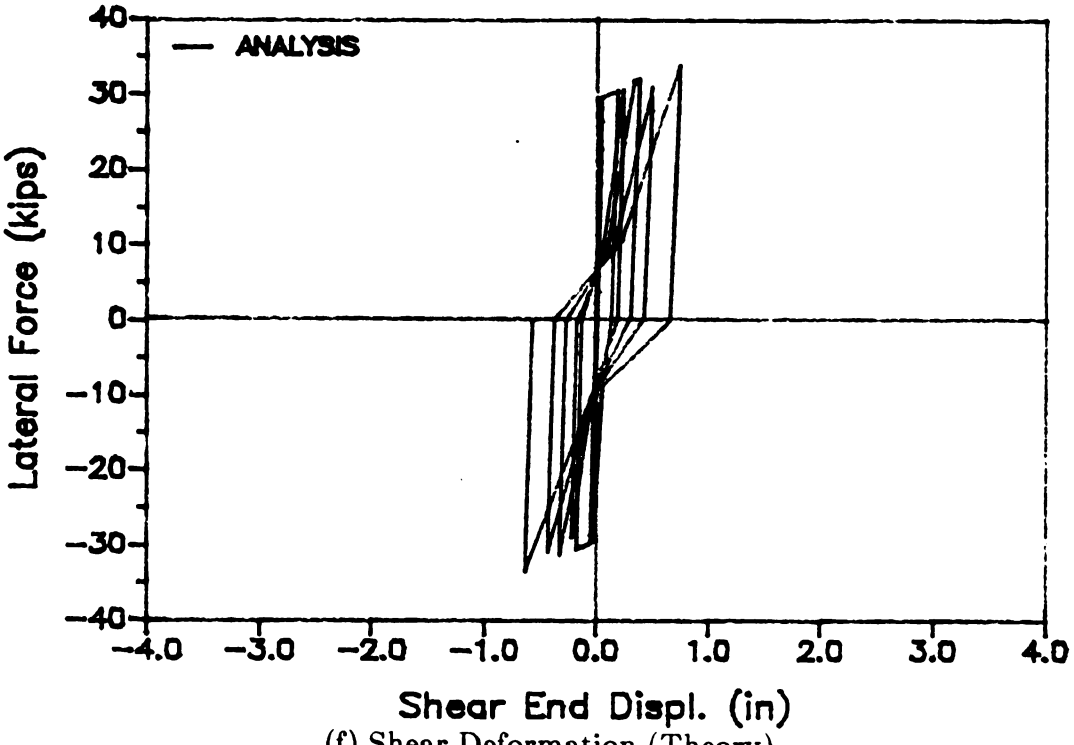

(f) Shear Deformation (Theory)

Figure 6.24 Experimental and Theoretical Cyclic Load-Deformation Relationships of Beam No. 3(cont'd)

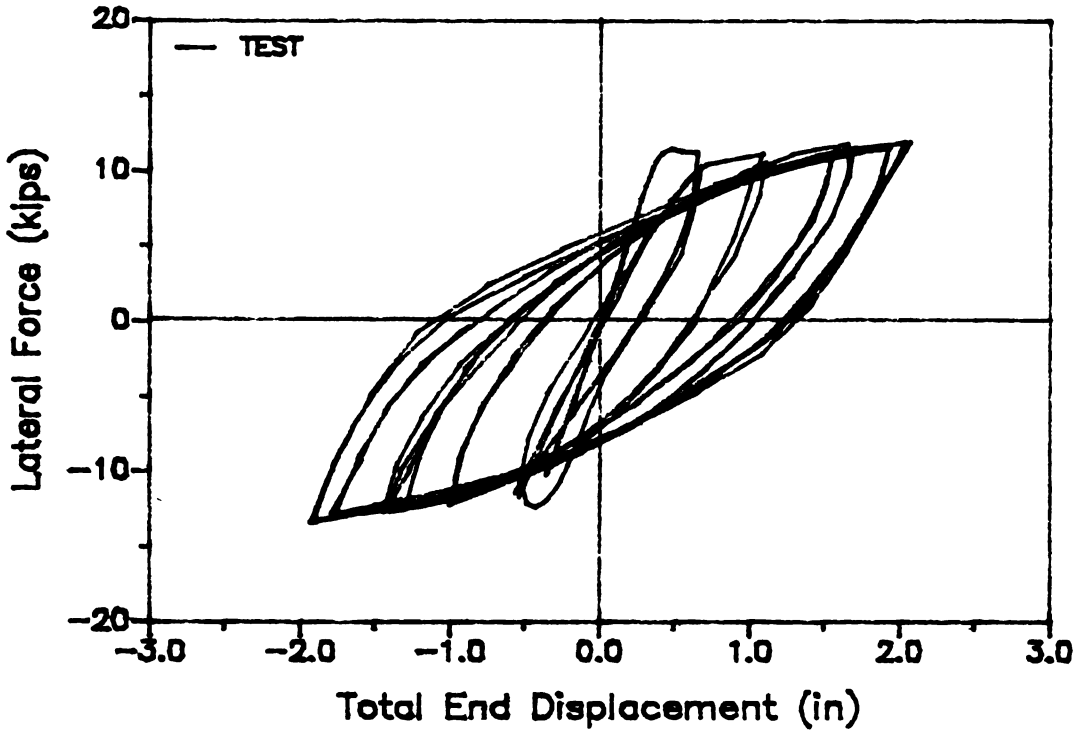

(a) Total Deformation (Experiment)

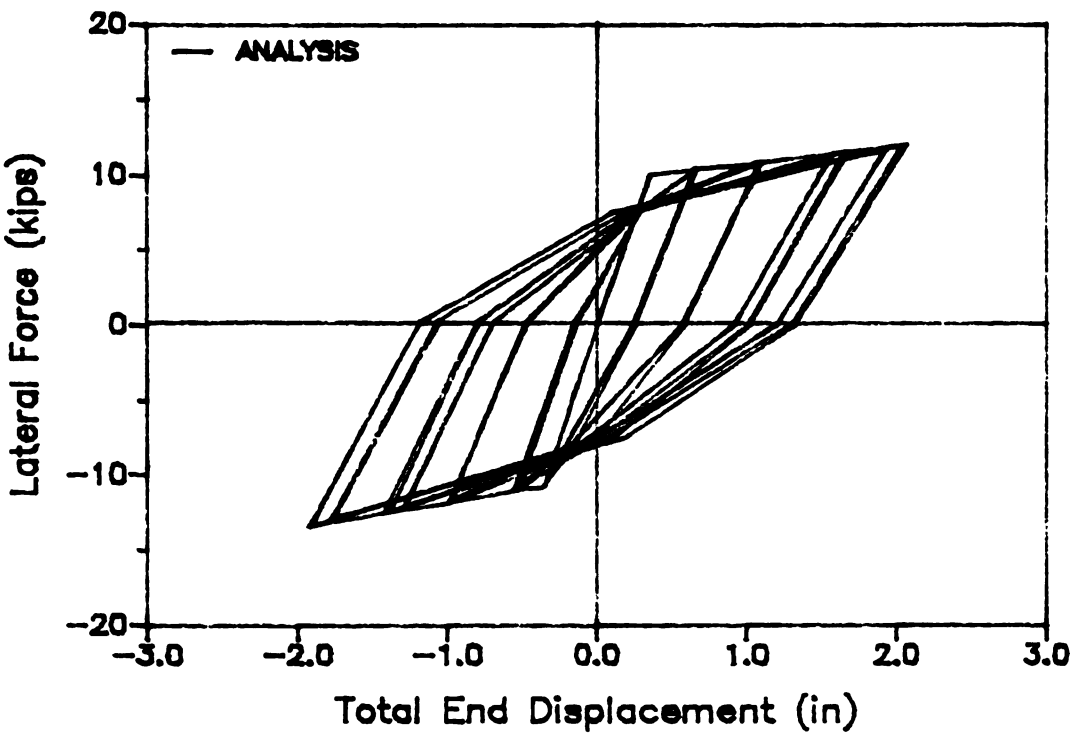

(b) Total Deformation (Theory)

Figure 6.25 Experimantal and Theoretical Total Cyclic Load-Displacement Relationships of Beam No. 4

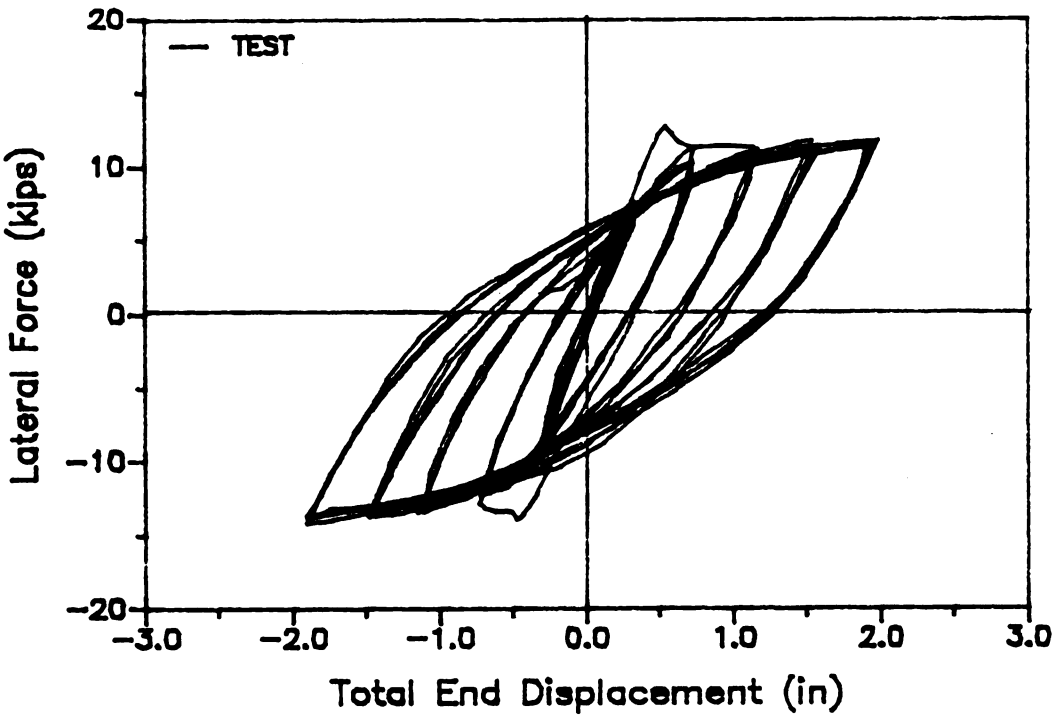

(a) Total Deformation (Experiment)

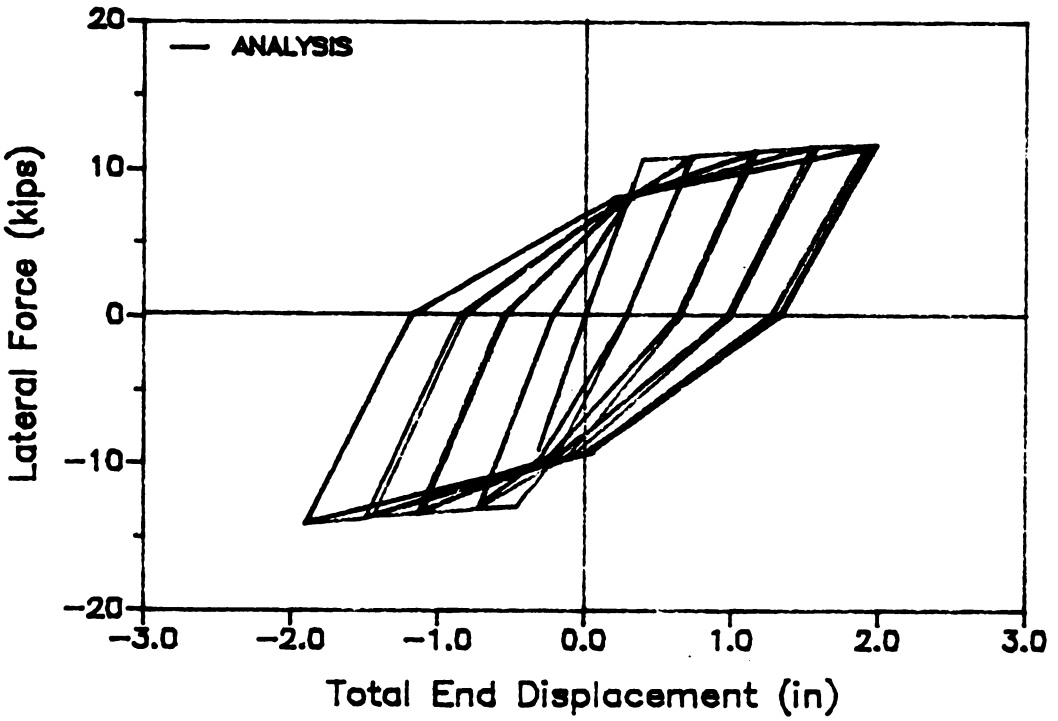

(b) Total Deformation (Theory)

Figure 6.26 Experimantal and Theoretical Total Cyclic Load-Displacement Relationships of Beam No. 5

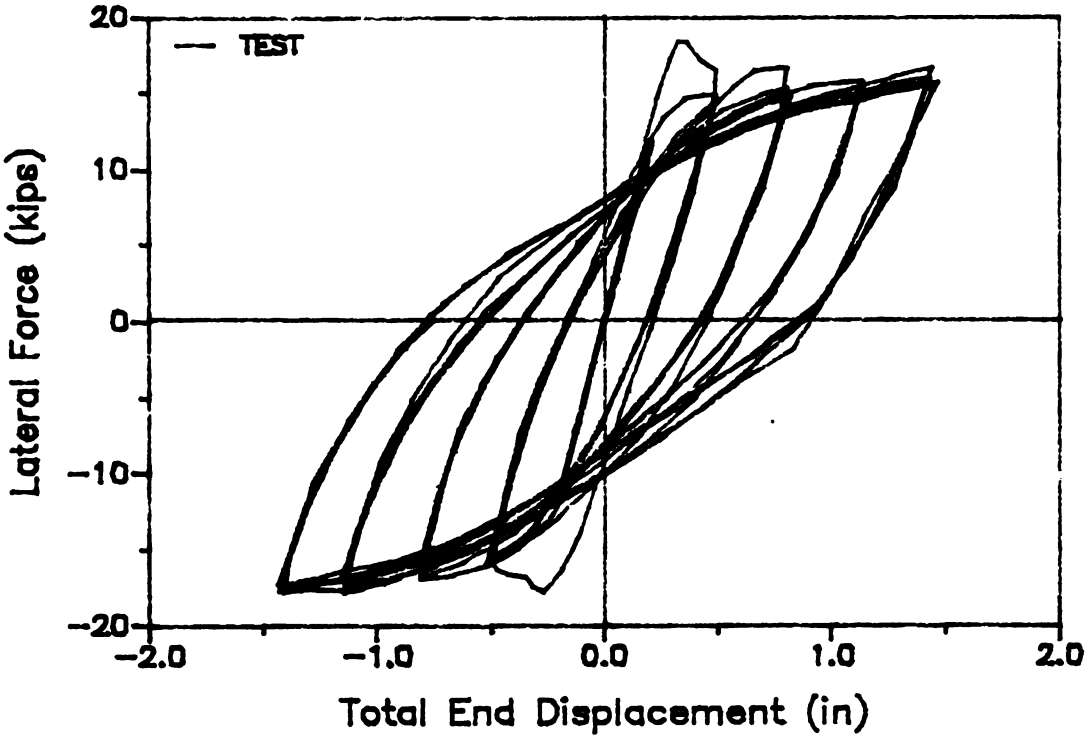

(a) Total Deformation (Experiment)

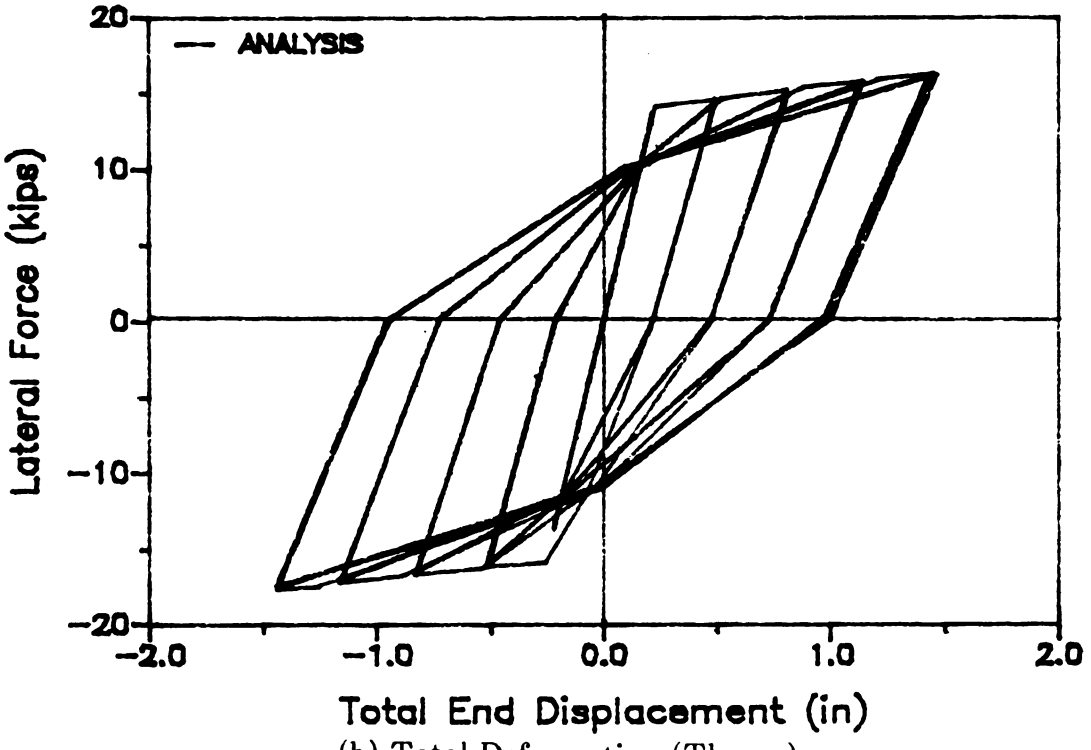

(b) Total Deformation (Theory)

Figure 6.27 Experimantal and Theoretical Total Cyclic Load-Displacement Relationships of Beam No. 6

6.6 SUMMARY AND CONCLUSIONS

Under monotonic loads, shear deformations generally constitute only a minor fraction of the overall displacements of the R/C beam elements. Consequently, the shear deformations have traditionally been neglected in analytical modeling of the R/C elements. Repeated inelastic load reversals, however, tend to deteriorate the shear resisting mechanisms in a faster pace than the flexural ones. Hence, shear deformations play an increasingly important role in determining the element behavior under inelastic load cycles, and the disregard for shear deformations in analytical modeling can lead to major discrepancies between cyclic test results and theoretical predictions.

A practical element model was developed in this study to predict the hysteretic behavior of R/C beams, accounting for the distinct hysteretic characteristics of shear and flexural deformations. All the elasto-plastic deformations were assumed to be concentrated in dimensionless serial shear and flexural springs at the element ends. The behavior of each spring was defined by a semi-empirical skeleton force-deformation curve and a set of empirical hysteretic rules which were derived from the available cyclic test results on R/C beam (in which the shear and flexural deformations were measured separately).

Based on the developed physical model (with concentrated shear and flexural springs), tangent stiffness matrices were constructed for cantilever beams and general beam elements.

The element model was checked against the results of a number of cyclic tests performed on R/C cantilever beams with wide ranges of geometric and material properties. The comparison between test and theory was satisfactory, and both the experimental and theoretical cyclic load-deformation relationships indicated that the repetition of inelastic load cycles leads to a growing dominance of shear deformations in the cyclic behavior of R/C beams.

CHAPTER 7

SUMMARY AND CONCLUSIONS

This investigation dealt with two critical aspects of the dynamic response characteristics of R/C structures which are generally neglected in developing dynamic analysis and design procedures. These two aspects are the effects of the relatively high strain rates induced by the dynamic (e.g., seismic and impulsive) loads in structures, and the role of shear deformations in the cyclic load-deformation behavior of R/C elements and structures.

In the first phase of this investigation, summarized in chapters 2 to 5, refined strain rate-sensitive models were developed for nonlinear axial-flexural inelastic analysis of R/C elements under monotonic dynamic loads. These models were used to assess the strain rate-sensitivity of the axial behavior of R/C columns and the flexural behavior of R/C beams. The steps involved in this phase of the research, and conclusions at each step are presented below.

Constitutive Modeling of Concrete

On the basis of many test results reported by different investigators, empirical models were developed for the strain rate effects on the concrete compressive strength, strain at maximum stress, and modulus of elasiticity. It was found that

(1) the concrete compressive strength increases at higher strain rates, and this increase is more significant for saturated concrete,

(2) the strain at maximum stress first decreases and then increases as the strain rate increases over the static values, and

(3) at higher strain rates, the secant modulus of elasticity of concrete increases. The initial tangent modulus also increases at higher strain rates but at a much slower rate when compared with the secant modulus.

The preceding idealizations of the strain rate effects were used to develop a practical constitutive model for confined and unconfined concrete subjected to different compressive strain rates. This model compared well with test results.

Constitutive Modeling of Steel

Dynamic test results reported by different investigators on structural steel, deformed bars, and deformed wires subjected to monotonic tension were used for deriving empirical expressions for the ratios of static to dynamic values of the yield and ultimate strengths, yield and ultimate strains, and the strain at the end of the yield plateau. The principal variables in the expressions are the rate of straining and the steel static yield strength. The following conclusions was derived:

(1) All the characteristic stress and strain values on the steel monotonic constitutive diagram increase with increasing strain rate. The yield strength is more strain rate-sensitive than the ultimate strength. The steel modulus of elasticity is independent of the rate of straining.

(2) The main factor influencing the strain rate effects is the static yield strength of steel. The mechanical properties of steel with lower yield strength are more strain rate-sensitive.

(3) No considerable difference was observed between the strain rate effects on structural steel, deformed bars, and deformed wires.

(4) The empirical strain rate-dependent constitutive models proposed in this chapter for steel subjected to monotonic loading compare well with test results.

Element Modeling and Numerical Studies

Empirical strain rate-sensitive constitutive models of steel and concrete were incorporated into an analytical procedure for axial/flexural analysis of R/C beam-columns at different loading rates. The analytical predictions compared well with quasi-static and dynamic test results. Simple practical analysis procedures were also developed for calculating the axial and flexural strengths of R/C columns and beams as functions of the applied loading rates.

The refined (layer) analytical method was used to perform a numerical study on the sensitivity of the axial and flexural performances of R/C sections and elements to the changes in steel and concrete strengths, concrete confinement and the rate of load application. The results of this numerical study indicated that:

(1) Variations in longitudinal steel yield strength have major effects on the flexural strength, and some important effects on the axial strength of the typical beam and column cross sections considered in this study ($\pm$ 30% variations in the longitudinal steel yield strength causes changes of the order of $\pm$ 30% in flexural strength and $\pm$ 10% in axial compressive strength). The axial and flexural stiffnesses, however, are not much influenced by the variations in yield strength.

(2) Variations in the concrete compressive strength have relatively small effects on the beam flexural behavior, but major effects on the column compressive stiffness and strength. For the typical beam and column cross sections studied here, $\pm$ 30% changes in concrete compressive strength resulted in variations of about $\pm$ 3% and $\pm$ 25%, respectively, in the flexural and compressive

strengths (and stiffnesses).

(3) The flexural behavior of reinforced concrete beam sections is strongly influenced by the variations in the tension steel ratio, but not much by the changes in compression steel ratio. A ± 30% change in tension steel ratio results in about ± 30% change of a typical beam flexural stiffness and strength. The axial strength and stiffness of R/C column cross sections are also found to be sensitive to the variations in their total steel area. Changes of the order of ± 15% were observed in strength of a typicaal column as a result of ± 30% changes in the total steel area.

(4) Increased confinement does not have major effects on the beam flexural behavior (neglecting the possibility of compression steel buckling). It, however, slightly increases the compression strength and ductility of the column.

(5) Under typical impulsive loading rates, the axial strength and stiffness of typical R/C columns increase by about 30% over the corresponding quasi-static values.

(6) The flexural strengths of typical R/C beams increase by about 15% at typical impulsive loading rates over the quasi-static values. The flexural stiffnesses of R/C beams is not much influenced by the loading rate variations.

(7) The loading rate-sensitivity of R/C column axial behavior increases with decreasing yielding strength and increasing degree of saturation of concrete. The variations in steel ratio, concrete compressive strength, confinement and cross sectional shape of columns do not significantly influence the column loading rate-sensitivity.

(8) The loading rate-sensitivity of R/C beam flexural behavior increases with decreasing steel yield strength and increasing steel ratio and concrete degree of saturation. The variations in concrete compressive strength, confinement,

and element length and cross sectional shape do not significantly influence the loading rate-sensitivity of R/C beams in flexure.

In the second phase of research, summarized in chapter 6, an element model capable of distinguishing between the shear and flexural hysteretic characteristics for R/C elements was developed and verified against test results. The findings of this phase are summarized below.

Under monotonic loads, shear deformations generally constitute only a minor fraction of the overall displacements of the R/C beam elements. Consequently, the shear deformations have traditionally been neglected in analytical modeling of the R/C elements. Repeated inelastic load reversals, however, tend to deteriorate the shear resisting mechanisms in a faster pace than the flexural ones. Hence, shear deformations play an increasingly important role in determining the element behavior under inelastic load cycles, and the disregard for shear deformations in analytical modeling can lead to major discrepancies between cyclic test results and theoretical predictions.

A practical element model was developed in this study to predict the hysteretic behavior of R/C beams, accounting for the distinct hysteretic characteristics of shear and flexural deformations. All the elasto-plastic deformations were assumed to be concentrated in dimensionless serial shear and flexural springs at the element ends. The behavior of each spring was defined by a semi-empirical skeleton force-deformation curve and a set of empirical hysteretic rules which were derived from the available cyclic test results on R/C beam (in which the shear and flexural deformations were measured seperately).

Based on the developed physical model (with concentrated shear and flexural springs), tangent stiffness matrices were constructed for cantilever beams and general beam elements.

The element model was checked against the results of a number of cyclic tests performed on R/C cantilever beams with wide ranges of geometric and material properties. The comparison between test and theory was satisfactory, and both the experimental and theoretical cyclic load-deformation relationships indicated that the repetition of inelastic load cycles leads to a growing dominance of shear deformations in the cyclic behavior of R/C beams.

LIST OF REFERENCES

1. American Society for Testing and Materials, "Standard Test Method for Compressive Strength of Cylindrical Concrete Specimens," Designation: c39-81, *1982 Annual Book of ASTM Standards*, Part 14: Concrete and Mineral Aggregates, pp. 26-29.
2. Amreican Society for Testing and Materials, "Standard Test Method for Flexural Strength of Concrete Using Simple Beam with Third-Point Loading," Designation: C78-75, *1982 Annual Book of ASTM Standards*, Part 14: Concrete and Mineral Aggregates, pp. 40-42.
3. American Society for Testing and Materials, "Standard Methods and Definitions for Mechanical Testing of Steel Productes," Designation: A 370-77, *1984 Annual Book of ASTM Standards*, Section 1, Iron and Steel Productes, pp. 261-316.
4. Scott, B. D., Park, R. and Priestley, M. J. N., "Stress-Strain Behavior of Concrete Confined by Overlaapping Hoops at Low and High Strain Rates," *Journal of the American Concrete Institute* , Jan.-Feb. 1982, pp. 13-27.
5. Mahin, S. A. and Bertero, V. V., "Rate of Loading Effects on Uncracked and Repaired Reinforced Concrete Members," *Report No. UCB/EERC-72/09*, Earthquake Engineering Research Center, University of California, Berkely, CA, Dec. 1972.
6. Fenwick, R. C., Tankut, A.T., and Thom, C. W., "The Deformation of Reinforced Concrete Beams Subjected to Inelastic Cyclic Loading - Experiment Results," *Report No. 268*, Dept. of Civil Engineering, Univ. of Auckland, Private Bag, Auckland, New Zealand, Oct. 1981.
7. Fenwick, R. C., "Shear Deformations in Seismic Response of Frame Structures," *Journal of Structural Division*, ASCE, Vol. 109, No. ST 4, April, 1983.
8. Thom, C. M., "The Effects of Inelastic Shear on The Seismic Response of Structures," A Thesis Submitted in Partial Fulfilment of the Requirements for the Degree of Philosophy, Department of Civil Engineering, University of Auckland, Private Bag, Auckland, New Zealand, March 1983.
9. American Concrete Institute, "Building Code Requirements for Reinforced Concrete," ACI 318-83, Nov. 1983.
10. Dilger, W. H., Koch, R., and Kowalczyk, R., "Ductility of Plain and Confined Concrete Under Different Strain Rates," *Journal of the American Concrete Institution*, Vol. 81, No. 1, Jan-Feb. 1984, pp. 75-82.
11. Kaplan, S. A., "Factors Affecting the Relationship Between Rate of Loading and Measured Compressive Strength of Concrete," *Magazine of Concrete Research*, Vol. 32, No. 111, June 1980, pp. 79-88.
12. Seabold, R. H., "Dynamic Shear Strength of Reinforced Concrete Beams - Part III," *Technical Report No. R-695*, U.S. Naval Civil Engineering Laboratory, Port Hueneme, California, Sept. 1970.
13. Watstein, D., "Effect of Straining Rate on the Compressive Strength and Elastic Properties of Concrete," *Journal of the American Concrete Institute*, Vol. 49, No. 8, April 1953, pp. 729-744.

14. Cowell, W. L., "Dynamic Properties of Plain Portland Cement Concrete," *Technical Report No. R447*, U.S. Naval Civil Engineering Laboratory, Port Hueneme, California, June 1966.

15. Shah, S. P., Fafitis, A., and Arnold, R., "Cyclic Loading of Spirally Reinforced Concrete," *Journal of the Structural Division*, American Society of Civil Engineers, Vol. 109, No. 7, July 1983, pp. 1695-1710.

16. Kaba, S. A., and Mahin, S. A., "Interactive Computer Analysis for Predicting the Inelastic Cyclic Behavior of Structural Sections," *Report No. UCB/EERC-83/18*, Earthquake Engineering Research Center, University of California, Berkeley, July 1983.

17. Raphael, J. M., "Tensile Strength of Concrete," *Journal of The American Concrete Institute*, Vol. 81, No. 2, March-April 1984, pp. 158-165.

18. Komlos, K., "Factors Affecting Stress-Strain Relation of Concrete in Uniaxial Tension," *Journal of the American Concrete Institute*, Vol. 66, No. 2, Feb. 1969, pp. 111-114.

19. Birkimer, D., and Lindemann, R., " Dynamic Tensile Strength of Concrete Materials," *Journal of the American Concrete Institute*, Vol. 79, No. 1, January 1971, pp. 42-49.

20. Wright, P. J. F., "The Effect of the Method of Test on the Flexural Strength of Concrete," *Magazine of Concrete Research*, No. 10, July 1953, pp. 67-76.

21. Norris, C. H., Hansen, R. J., Hokey, Jr., M. J., Diggs, J. M., Namyet, S., and Minami, J. K., *Structural Design for Dynamic Loads* , McGraw Hill Book Company, Inc., 1959.

22. Winlock, J., "The Influence of the Rate of Deformation on the Tensile Properties of Some Plain Carbon Sheet Steel," *Journal of Metals* , ASME, Vol. 197, June 1955, pp. 797-803.

23. Fuss, R. J., "Dynamic Compression Tests on Thin-Section Reinforced Concrete," *Technical Report R406*, U.S. Naval Civil Engineering Laboratory, Port Hueneme, California, Dec. 1985.

24. Seabold, R. H., "Dynamic Shear Strength of Reinforced Concrete Beams - Part II," *Technical Report R-502* , U.S. Naval Civil Engineering Laboratory, Port Hueneme, California, January 1967.

25. Cowell, W. C., "Dynamic Test of Concrete Reinforcing Steel," *Technical Report R394* , U.S. Naval Civil Engineering Laboratory, Port Hueneme, California, Sept. 1965.

26. Staffier, S. R, and Sozen, M. A., "Effect of Strain Rate on Yield Stress of Model Reinforcement," *Structural Research Series No. 415, Civil Engineering Studies*, University of Illinois, Urbana, Illinois, Feb. 1975.

27. Filippou, F. C., Popov, E. P, and Bertero, V. V., "Effects of Bond Relation on Hysteretic Behavior of R/C Joints," *Report No. UCB/EERC-83/19*, Earthquake Engineering Research Center, University of California, Berkeley, CA, Aug. 1983.

28. Celebi, M., and Penzien, J., "Experimental Investigation Into The Seismic Behavior of Critical Regions of Reinforced Concrete Components as Influenced by Moment and Shear," *Report No. UCB/EERC-73/04*, Earthquake Engineering Research Center, University of California, Berkeley, CA, Jan. 1973.

29. Bertero, V. V., Aktan, A. E., Charney, F. A., and Sause, R., "U.S.-Japan Cooperative Earthquake Research Program: Earthquake Simulation Tests and Associated Studies of a 1/5th - Scale Model of a 7-Story Reinforced Concrete Test Structure," *Report No. UCB/EERC-84/05*, Earthquake Engineering Research Center, University of California, Berkeley, CA, June 1984.

30. Aktan, A. E., Bertero, V. V., and Piazza, M., "Predicting of the Seismic Response of R/C Frame Coupled Wall Structures," *Report No. UCB/EERC-82/12* , Earthquake Engineering Research Center, University of California, Berkeley, CA, Aug. 1982.

31. Takayanagi, T., and Schnobrich, W. C., "Computed Behavior of Reinforced Concrete Coupled Shear Walls," *Civil Engineering Studies, Structural Research Series No. 434* , University of Illinois, Urbana-Champaign, Dec. 1976.

32. Keshavarzian, M., and Schrobrich, W., "Computed Nonlinear Seismic Response of R/C Wall-Frame Structures" *Civil Engineering Studies, Structural Research Serirs No. 515*, University of Illinois, Urbana-Champaign, May 1984.

33. Suariz, W., and Shah, S. P., "Properties of Concrete Subjected to Impulse," *Journal of the Structural Division*, American Society of Civil Engineers, Vol. 109, No. 7, July 1983, pp. 1727-1741.

34. Eligehausen, R., Popov, E. P., and Bertero, V. V., "Local Bond Stress-Slip Relationship of Deformed Bars Under Generalized Excitation," *Report No. UCB/EERC-83/23*, Earthquake Engineering Research Center, University of California, Berkeley, CA. Oct. 1983.

35. Tassios, T. P., "Properties of Bond Between Concrete and Steel Under Load Cycles Idealizing Seismic Action," Comite' Euro-International Du Be'ton, Bulletin, No. 131, Paris, April 1979.

36. Perry, E. S., and Jundi, N., "Pull-Out Bond Stress Distribution Under Static and Dynamic Repeated Loading," *Journal of the American Concrete Institute*, Vol. 66, No. 5, May 1969, pp. 377-380.

37. Ataly, M. B., and Penzien, J., "The Seismic Behavior of Critical Regions of Reinforced Concrete Components As Influenced by Moment, Shear and Axial Force," *Report No. UCB/EERC-75/19*, Earthquake Engineering Research Center, University of California, Berkeley, Dec. 1975.

38. Soroushian, P., and Obaseki, K., "Strain Rate-Dependent Interaction Diagrams for Reinforced Concrete Sections," *Journal of the American Concrete Institute* , Vol. 83, No. 1, Jan-Feb. 1986, pp. 108-116.

39. Bazant, P. Z., and Bhat, P. P., "Prediction of Hysteresis of R/C Members," *Journal of the Structural Division*, American Society of Civil Engineers, Vol. 103, No. ST 1, Jan. 1977, pp. 153-167.

40. Meregotto, M., and Pinto, P., "Method of Analysis for Cyclically Looded Reinforced Concrete Plane Frames Influencing Changes in Geometry and Nonlinean Behavior of Elements under Combined Normal Force and Bending," *Proceedings,* Symposium on Resistance and Ultimate Deformability of Structures Acted by Well-Defined Repeated Loads, IABSE, Lisbon, 1973.

41. Wood, D. S., "Rapid Loading Tests on Three Grades of Reinforcing Steel," *Report under Contract NOY-90922 with NCEL*, May 1956.

42. Kaba, S. A., and Mahin, S. A., "Refined Modeling of Reinforced Concrete Columns for Seismic Analysis," *Report No. UBC/EERC-84/03*, Earthquake Engineering Research center, University of California, Berkely, CA, April 1984.

43. Soroushian, P. and Sim, J., "Axial Behavior of R/C element under Dynamic Loads," *Journal of the American Concrete Institute,* Vol. 83, No. 6, Nov.-Dec. 1986, pp. 1018-1025.

44. Moehle, J. P., and Cavanagh, T., "Confinement Effectiveness of Crossties in RC," *Journal of the Structural Division*, American Society of Civil Engineers, Vol. 111, No. 10, Oct. 1985, pp. 2105-2120.

45. Scribner, C. F., and Wight, J. K., " Delaying Shear Strength Decay in R/C Flexural Members Under Large Load Reversals," *Report UMEC 78-R2*, Civil Engineering Department, Univ. of Michigan, Ann Arbor, MI, 1978.

46. Ma, S. M., Bertero, V. V., and Popov, E. P., "Experimental and Analytical Studies on The Hysteretic Behavior of R/C Rectangular and T-Beams," *Report No. UBC/EERC-76/02*, Univ. of California, Berkely, CA, May, 1976.

47. Aoyama, H., "Simple Nonlinear Model for The Seismic Response of Reinforced Concrete Buildings," *Proceedings*, US - Japan Cooperative Earthquake Research Program, Aug. 1975.

48. Küstü, O., and Bouwkamp, J. G., "Behavior of Reinforced Concrete Deep Beam - Column Subassemblages Under Cyclic Loads," *Report No. UBC/EERC-75/08*, Univ. of California, Berkely, CA, May, 1975.

49. Clough, R. H., "Effect of Stiffness Degradation on Earthquake Ductility Requirements," *Report No. 66-16*, Dept. of Civil Engineering, Univ. of California, Berkely, 1966.

50. Takeda, T., Sozen, M. A., and Nielson, N. N., "Reinforced Concrte Response to Simulated Earthquakes," *Journal of Structural Division*, ASCE, Vol. 96, No. ST 12, Dec. 1970, pp. 2557-2573.

51. Jennings, P. C., "Response of Yielding Structures to Statistically Generated Ground Motions," *Proceedings of The 3rd World Conference on Earthquake Engineering*, New Zealand, 1963, Vol. II, pp. 237-259.

52. Celebi, M., "Hysteretic Behavior of Reinforced Concrete Beams Under The Influence of Shear and Bending," *Proceedings of The Symposium on Earthquake Engineering*, Univ. of Rourkei, India, 1974, Vol. 5, pp. 375-380.

53. Shiha, B. P., Gerstle, K. H., and Tulin, L. G., "Stress-Strain Relationships for Concrete Under Cyclic Loading," *Journal of the American Concrete Institute,* Vol. 61, No. 2, Feb 1964, pp. 195-211.

54. Singa, T., Ogana, J., Shibata, A., and Shibuyu, J. J., "The Dynamic Properties of Reinforced Concrete Frames," *Proceedings of The US - Japan Seminar on Earthquake Engineering with Emphasis on Safty of School Buildings*, Sendai, Japan, 1970.